Università degli Studi di Catania

Dottorato di Ricerca in Scienza e Tecnologia dei Materiali

XXVI - Ciclo

Preparation and Characterization of Single Walled Carbon Nanotubes – Poly(3-hexylthiophene) Nanohybrids

Gianfranco Sfuncia

Tutor: Chiar.mo Prof. G. Marletta

Coordinatore: Chiar.ma Prof.ssa M. G. Grimaldi

Table of Contents

1. Scope of the thesis

Since their discovery in 1990's carbon nanotubes have attracted the interest of a wide scientific community, both for fundamental and applied research. The reasons of this lie in the outstanding properties nanotubes possess: mechanical, electrical, thermal and optical properties unknown to every other material. This led scientists and engineers around the world to explore a wide range of technological applications that make use of these properties. The extraordinary mechanical properties of nanotubes are used in the fabrication of new, strong composites; their field-emission properties are employed to fabricate flat panel displays; the ballistic character of electronic transport in SWNT has been utilized to demonstrate SWNT transistors that outperform corresponding state-of-the-art silicon devices; while the sensitivity of their electrical characteristics on interactions with their environment is being used to produce chemical and biological sensors. Some of these technologies already have matured enough to enter the market place; others will require much more time. New uses of carbon nanotubes are continually being proposed, and it would not be an exaggeration to say that NTs are destined to become the key material of the 21st century.

Semiconducting conjugated polymers represent another class of materials with interesting properties which can be used as the active layer in LEDs, field effect transistors, solar cells, photodiodes, electrochemical cells and memory devices. They have proved to be of great importance as an active medium in lasers. These devices are being pushed toward commercialization because they can be fabricated by inexpensive techniques, such as spin coating, ink-jet printing, low temperature fiber drawing and screen-printing on the flexible substrates. This leads to a real advantage over the expensive and sophisticated technology used with inorganic materials in the semiconductor industry. The glass and flexible plastic foil make these devices particularly interesting because of the advantages they offer in terms of flexibility, low power, low weight, and low cost. In view of the above advantages, conducting plastics have emerged as a new class of electronic materials.

With these premises, a composite material obtained from carbon nanotubes and semiconducting polymers can only be of great interest. In fact, the interaction between two components confers new, unique properties to the composite materials, in a synergistic way, so that finale product properties are more than the simple addition of starting materials properties. These hybrid nanotubes/semiconducting polymer systems represent therefore very promising functional materials regarding a wide list of applications like hybrid organic field-effect transistor (OFET), organic light-emitting diode (OLED) and organic/polymeric solar cells (OSC/PSC).

These three main topics mentioned above are briefly discussed in three chapters composing the scientific background of this thesis.

The experimental part is divided into two parts: the first concerns the develop of a method for the purification of raw single walled nanotubes; the second part is focused on the preparation of a composite material based on the purified carbon nanotubes with a semiconducting polymer and on the characterization of the electrical and optical properties of such composite material. Finally, a nanostructuring technique that has allowed to obtain composite thin films with nanoscale phase separation has also been developed.

Purification of carbon nanotubes represents an hard task because of samples impurities heterogeneity, due to different synthesis technique, catalysts and reactants, that has prevented the develop of a universally valid protocol for nanotubes purification. Nowadays no synthesis technique is able to produce nanotubes without by-product like amorphous carbon, fullerenes and graphitic particles. In addition, single walled carbon nanotubes can only be synthesized using metallic catalyst that inevitably remains in the final product. For all these reason, purification of nanotubes is a preliminary, necessary step for further applications.

In this work, nanotubes were purified by means of a liquid phase oxidation, using a mixture of concentrated sulfuric and nitric acids. Different reaction conditions were investigated to find out the best conditions possible for purification, in terms both of final quality and final yield of the purified product. It was seen that reaction temperature has a deep effect on purification's results even for short reaction time. A second chemical step, namely a reflux in strong alkaline condition and high temperature, was necessary to further improve the quality of the purified nanotubes. This purification protocol based on two different steps was proved to be effective, allowing to obtain high quality purified nanotubes.

Purified nanotubes were characterized through atomic force microscopy (AFM), thermogravimetric analysis (TGA), Raman spectroscopy and near infrared photoluminescence spectroscopy (NIR-PL). AFM was used to obtain a direct visualization of samples purity after their deposition on substrates, allowing to evaluate the presence of amorphous carbon and the aggregation of the tubes in bundles. TGA was used to demonstrate the reduction of the residual metal content in the purified product, evidencing also that the oxidation-based purification is able to not lead substantial damage to the tubes, as evidenced by the high oxidation temperatures reported. Raman spectroscopy has allowed to analyze the effect of oxidation and base-wash steps onto the nanotubes through the analysis of the modification of their characteristic bands. In particular, the ratio between the intensity of the D band (due to defects) and the G band (correlated to the integrity of the structure) was used as qualitative index of the purity and the integrity of the samples. Variation of the characteristic band profile, linewidths and peak shifts gave important information that allowed to evidence the improved quality of the final product. Finally, NIR-PL proved that, after the oxidation-based purification, nanotubes emission properties are maintained, giving a direct proof of the integrity of the electronic structure which is therefore preserved undamaged so that it is possible for this purified nanotubes to realize their full potential by being integrated in electronic devices.

The second part of the thesis was focused on nanotubes/semiconducting polymer composites. Poly(3-hexylthiophene), (P3HT), was chosen as the semiconducting polymer for the composite fabrication because of its high conductivity that make it one of the most used material in organic electronics, suitable for fabrication of devices such as organic transistor or solar cells.

Composite dispersions were first prepared in liquid phase, using a noncovalent approach where nanotubes are stabilized in solution by the interaction with the conjugated polymer. These composite dispersions were prepared in different polymer/nanotube ratios and were used to deposit composite SWNTs/P3HT thin films. The electrical properties of these composite thin films were investigated through current-voltage measures using a Schottky diode configuration, with composite thin films deposited between the electrodes. Electrical measures highlighted the effect of the nanotubes on the transport behavior of the semiconducting polymer, revealing that nanotubes enhance the conductivity of the devices up to two orders of magnitude. In addition, the characteristic current profile of the diode is modified as function of the nanotubes ratio so that the system is no more rectifying but shows comparable conductivities for opposite applied voltages, evidencing therefore the capability to transport with comparable efficiency charge carriers with opposite sign, i.e. holes and electrons.

Optical properties of composite dispersion were investigated, in UV-Vis absorption and emission. Absorption spectroscopy revealed that P3HT and SWNTs interact so strongly to modify the absorbance spectrum of the polymer. A new signal, relative to those polymer chains adsorbed onto nanotubes, arises because physisorbed chains experiment both higher conjugation length and crystalline order induced by the strong π–π interactions with the underlying nanotube that modify the energy level of the polymer. This was further proved showing that the absorption spectrum of the composite dispersion matches fairly well with one obtained from a pure P3HT thin film. Finally, emission spectra evidenced quenching of the polymer fluorescence upon addition of nanotubes, due to charge transfer from the excited P3HT to the SWNTs further proving the interaction at molecular level between P3HT and SWNTs. This led to consider that the electronic interactions between P3HT and SWNTs are so strong to be responsible of the formation of stables supramolecular multifunctional composite complexes, hybrid systems characterized by a phase separation at nanoscale level, i.e. nanohybrids.

Finally, a method for the nanostructuring of SWNTs/P3HT composite thin films was developed. This method relies on the strong interaction between nanotubes and conjugated polymer to isolate nanohybrids after their formation in solution, obtaining a nanohybrid-enriched dispersion. The deposition of this dispersion allowed to create thin nanohybrids films which showed a singular morphology.

2. Carbon Nanotubes

2.1 Introduction

Carbon nanotubes have attracted tremendous interest from the scientific community over the last few years since their discovery by Iijima in 1991 [1] and in 1993 in their single-walled form [2]. The last few years witnessed a dramatic increase in nanomaterial and nanotechnology research. Among others, one of the most exciting fields to emerge is nanoelectronics [3–5], where a myriad of possibilities are appearing in the form of sensors [6], actuators [7], and transistors [8–10], each characterized by feature sizes of the order of a few nanometers. All this innovation has been fueled by the discovery of new materials and the invention of manufacturing methods that allow design and development at such a minute scale. Carbon nanotubes (CNTs) are at the forefront of these new materials, due to the unique mechanical and electrical properties that give them, e.g., exceptional strength [11] and conductivity [12]. Moreover, these nanotubes exhibit a tremendous current-carrying ability [13], potentially allowing for increased miniaturization of high-speed and high-power circuits. CNT molecules have a cylindrical structure and are formed by one or more concentric, crystalline layers of carbon atoms. These atoms are assembled in hexagonal-lattice graphene sheets, which are rolled up into seamless tubes and named according to the number of concentric sheets as being either multi or single-walled nanotubes. CNTs exhibit excellent physical, mechanical, and chemical properties so to be studied in a variety of fields to make use of their properties. Nanotubes appear to be paving the way for myriad possibilities in the growing nanotechnology and emerging biotechnology industries, particularly in nanoelectronics in the form of sensors, transistors, and interconnections. The potential application for CNTs in nano-optoelectronics also gives high expectation.

2.2 Structure of Single Walled Carbon Nanotubes

Carbon nanotubes are hollow graphite-based cylinders [14–17]. Depending on the number of graphite layers of the wall they are called single-walled (one graphite layer) (SWNTs), double-walled (two layers) (DWNTs), and so forth. Tubes with a large number of concentric cylinders – ten or more – are known as multiwall nanotubes (MWNTs). Graphene, a single sheet of graphite, is thus the basic building block of carbon nanotubes. Formally, a carbon nanotube is obtained by cutting a tiny strip out of a graphene sheet and rolling it up into a cylinder. The cutting of graphene fixes the so-called chiral or roll-up vector c. This vector goes around the circumference of the final tube (figure 2.1).

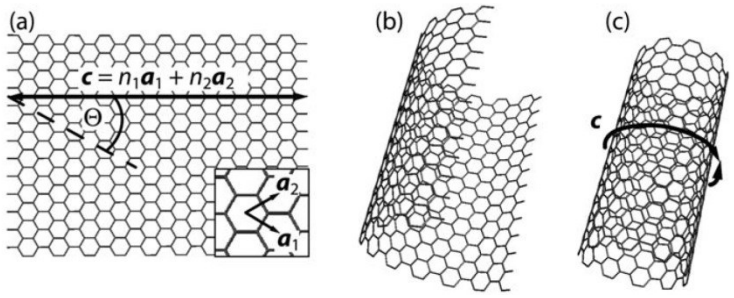

Figure 2.1 – A strip is cut out of graphene (a) and then rolled up (b) to form a seamless cylinder (c). The chiral vector *c* = 10(*a*1 + *a*2) in (a) forms the circumference of the (10,10) nanotube in (c). The *inset* in (a) shows the graphene lattice and the graphene unit cell vectors *a*1 and *a*2 on an enlarged scale

There are two parameters that control the microscopic structure of a nanotube, its diameter and its chiral angle or twist along the axis. Both are specified completely by $\boldsymbol{c}$, which is normally given in terms of the graphene lattice vectors $\boldsymbol{a_1}$ and $\boldsymbol{a_2}$ (inset of fig.1a)

$$\boldsymbol{c} = n_1\boldsymbol{a}_1 + n_2\boldsymbol{a}_2$$

(n_1, n_2) are called the chiral index of a tube and they fully characterize a tube ($n_1 > n_2 > 0$).

The diameter of a tube is related to the chiral vector by

$$d = \frac{|\boldsymbol{c}|}{\pi} = \frac{a_0}{\pi}\sqrt{n_1^2 + n_1n_2 + n_2^2}$$

where a_0 = 2.460˚A is the graphene lattice constant. For small tubes (d < 0.8 nm) the diameter is predicted to deviate from the geometrical diameter of a graphene cylinder. Ab-initio calculations show

that d becomes a function of the chiral angle below 0.8 nm [18]. Deviations from are below 2% for tube diameters $d \geq 5$˚A [18].

The second important parameter for carbon nanotubes is the chiral angle Θ, which is the angle between $\boldsymbol{a_1}$ and the chiral vector $\boldsymbol{c}$. The chiral angle specifies the arrangement of the graphene hexagons on the wall of the tube. Single-walled nanotubes having similar diameters show very different microscopic structure due to different chiral angles (figure 2.2).

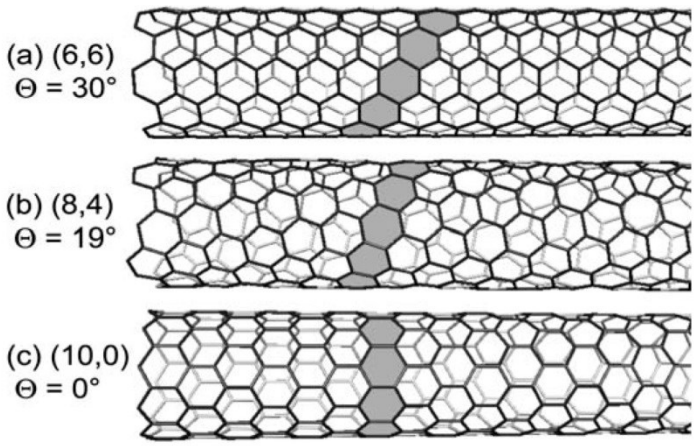

Figure 2.2 – Three carbon nanotubes with diameters around 0.8 nm: (a) (6,6) armchair, (b) (8,4) chiral tube and (c) (10,0) zigzag nanotube.

Θ is related to the chiral index by

$$\Theta = \arccos\left[\frac{n_1 + n_2/2}{\sqrt{n_1^2 + n_1 n_2 + n_2^2}}\right] = 30° - \arctan\left[\frac{1}{\sqrt{3}}\frac{n_1 - n_2}{n_1 + n_2}\right]$$

The chiral angle is allowed to vary between $0° \leq \Theta \leq 30°$; all other ranges of Θ are equivalent to this interval because of the hexagonal symmetry of graphene. A chiral angle of 0° and 30° corresponds to tubes with a particular high symmetry. They are called zigzag (Θ = 0°) and armchair tubes (Θ = 30°). The chiral vector not only determines the tube diameter and chiral angle, but all other structural parameters including the length of the unit cell and the number of carbon atoms in the unit cell.

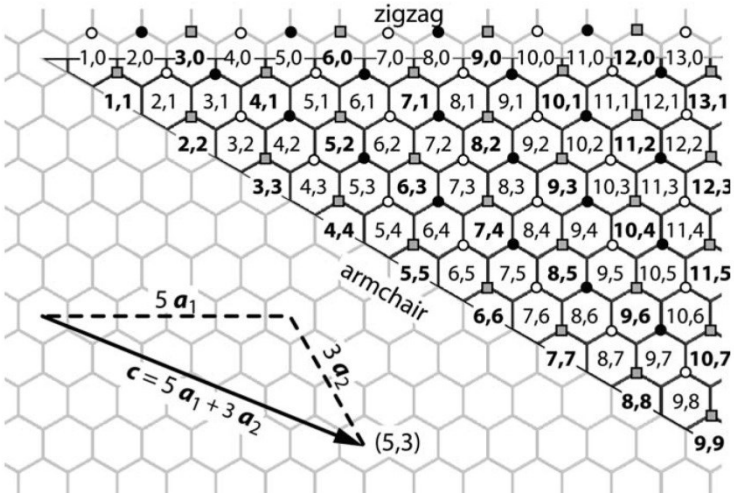

Figure 2.3 – Chiral indices of single-walled carbon nanotubes mapped onto a graphene sheet. The small symbols at the upper corner of a hexagon indicate the family of a nanotube. Closed circles are semiconducting tubes belonging to the ν = (n1 − n2) mod 3 = −1 (closed circles) or to the ν = (n1 − n2) mod 3 = +1 (open circles). Squares are tubes from the ν = 0 family. These tubes are metallic or quasimetallic, the latter having a small electronic bandgap induced by the curvature of the nanotube wall, ranging from 10meV to 100meV.

The series of (n, 0) zigzag nanotubes (that run horizontally in figure 2.3) have Θ = 0°. The name derives from the zigzag chain that forms the edge of this high-symmetry type of tubes (see figure 2.2c). The other high-symmetry nanotube structures are the (n, n) armchair tubes with Θ = 30°. The edge of their unit cell resembles a row of armchairs when viewed from above (figure 2.2a), hence the name.

Zigzag and armchair tubes are both called achiral tubes. A general nanotube with lower symmetry, like the (8,4) tube in figure 2.2b, is referred to as chiral.

2.3 Electronic Band Structure of Single Walled Carbon Nanotubes

The electronic band structures of single-walled carbon nanotubes (SWNTs) along with their small size and low dimension are responsible for their unique electrical transport properties. Since a SWNT can be considered as a graphene sheet, rolled up to form a hollow cylinder, the band structures of SWNTs can be obtained from that of graphene, a two-dimensional (2D) layer of graphite.

2.3.1 Electronic band structure of graphene

The lattice structure of graphene in real space consists of hexagonal arrangement of carbon atoms. (figure 2.4). An isolated carbon has four valence electrons in 2s, $2p_x$, $2p_y$, and $2p_z$ atomic orbitals. In graphene, three atomic orbitals 2s, $2p_x$, $2p_y$, are hybridized into three sp^2 orbitals lying in the same plane while the $2p_z$ orbital remains perpendicular to this plane. The hybridized orbitals are responsible for the σ bonds between the adjacent carbon atoms and the $2p_z$ orbitals result in π bonds out of the plane of graphene. These π orbitals lie near the Fermi level and are therefore responsible for the electrical transport properties of graphene.

Figure 2.4 – A graphene sheet, where the carbon atoms are arranged in a honeycomb lattice.

The band structure of graphene derived by π orbitals can be calculated by the tight-binding approximation [19]. Graphene unit cell has two nonequivalent carbon atoms, A and B; all other atoms in the lattice can be obtained by translation of A or B using a linear combination of two unit vectors $\mathbf{a_1}$ and $\mathbf{a_2}$ (figure 2.5a). From the real space lattice is possible to obtain the reciprocal space lattice, characterized by two unit vectors $\mathbf{b_1}$ and $\mathbf{b_2}$ and by high-symmetry points, Γ, K, M in a Brillouin zone (figure 2.5b).

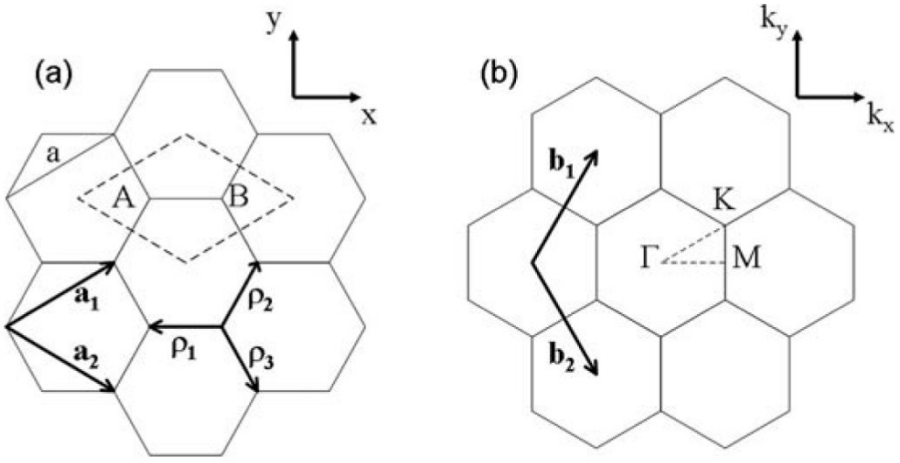

Figure 2.5 – Real space representation of a graphene lattice with unit vectors a1 and a2. A unit cell is shown as a dashed rhombus with two carbon atoms (A and B) (a). Reciprocal space representation of a graphene lattice with two unit vectors b1 and b2. High-symmetry points (Γ, K, M) in a Brillouin zone are also shown (b).

The band structure of graphene π orbitals can be obtained resolving Schrödinger equation.

$$H\psi = E\psi$$

Where H is the Hamiltonian, ψ is the total wave function, and E is the energy of electrons in orbitals of graphene. In a periodic system as in graphene, the total wave function can be constructed from a linear combination of Bloch functions, u_i, which has a periodicity of the lattice. In the tight-binding approximation, u_i is represented by a linear combination of atomic wave functions. Since only the π orbitals from the 2pz orbital of each atom are considered, Bloch function u_i, for each atom can be constructed from 2pz orbitals of atoms A and B as

$$u_{A(B)} = \frac{1}{\sqrt{N}} \sum_{A(B)} e^{i\boldsymbol{k}\cdot\boldsymbol{r}_{A(B)}} X(\boldsymbol{r} - \boldsymbol{r}_{\boldsymbol{A(B)}})$$

Where X(**r**) is the orbital 2pz wave function for an isolated carbon atom. Then ψ can be written as:

$$\psi = C_A u_A + C_B u_B$$

Leading to:

$$\begin{pmatrix} H_{AA} & H_{AB} \\ H_{BA} & H_{BB} \end{pmatrix} \begin{pmatrix} C_A \\ C_B \end{pmatrix} = \begin{pmatrix} S_{AA} & S_{BB} \\ S_{BA} & S_{BB} \end{pmatrix} \begin{pmatrix} C_A \\ C_B \end{pmatrix}$$

In which,

$$H_{ij} = \langle u_i \,|H|\, u_j \rangle, \qquad S_{ij} = \langle u_i \,|\, u_j \rangle$$

The overlap between wave functions of different atoms are neglected, i.e. $S_{AB} = S_{BA} = 0$. Imposing a normalization condition, $S_{AA} = S_{BB} = 1$, the matrix equation is simplified to:

$$\begin{pmatrix} H_{AA} - E & H_{AB} \\ H_{BA} & H_{BB} - E \end{pmatrix} \begin{pmatrix} C_A \\ C_B \end{pmatrix} = \begin{pmatrix} 0 \\ 0 \end{pmatrix}$$

Which has a nontrivial solution only when:

$$\begin{vmatrix} H_{AA} - E & H_{AB} \\ H_{BA} & H_{BB} - E \end{vmatrix} = 0$$

Since A and B atoms are not distinguishable, $H_{AA} = H_{BB}$ and $H_{AB} \neq H_{BA}$, leading to the solution:

$$E = H_{AA} \mp |H_{AB}|$$

H_{AA} and H_{AB} can be calculate using the Bloch functions to finally obtain the energy dispersion for π orbitals in graphene, using the coordinate system of the graphene in figure 2.5a:

$$E = E_0 \mp \gamma_0 \sqrt{\left(1 + 4\cos\left(\frac{\sqrt{3}\,k_x a}{2}\right) cos\left(\frac{k_y a}{2}\right) + 4\, cos^2\left(\frac{k_y a}{2}\right)\right)}$$

Where γ_0 is called as the tight-binding or transfer integral which measures the strength of exchange interaction between nearest atoms. Negative sign denote valence bands of graphene formed by bonding π orbitals, while positive sign represents conduction bands formed by antibonding π* orbitals. The dispersion relation along high-symmetry points in the reciprocal space with $E_0 = 0$ is plotted in figure 2.6.

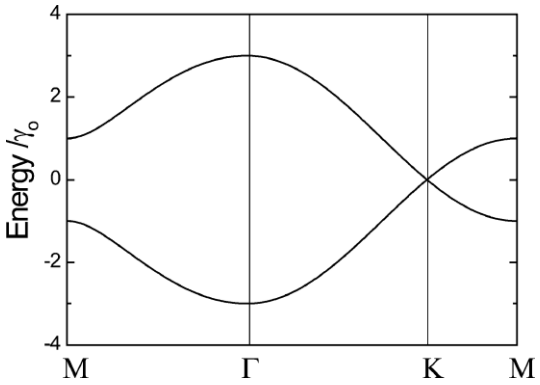

Figure 2.6 – Energy dispersion of graphene along high-symmetry points

The surface and contour plots of energy dispersion are shown in figure 2.7.

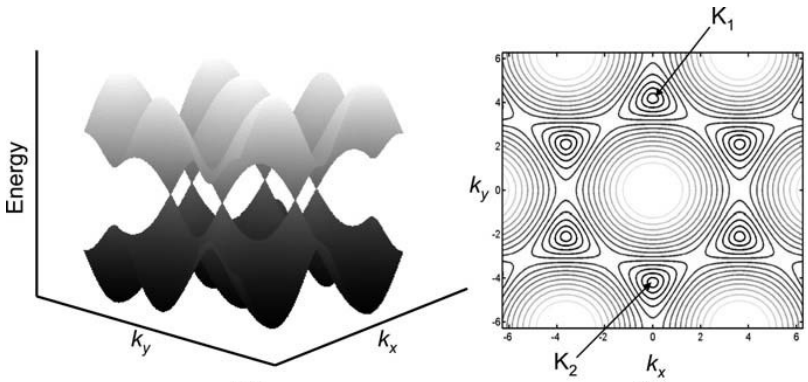

Figure 2.7 –Surface plot (a) and contour plot (b) of the energy dispersion in graphene. There are six K points where the bandgap becomes zero. Of the six K points, only two are nonequivalent, denoted by K1 and K2, originating from two nonequivalent atoms in the real space unit cell.

The main feature of the energy dispersion of graphene is the six K point at the corners of the Brillouin zone, where the conduction and valence bands meet so that the bandgap is zero only at these points.

The density of states (DOS) in graphene can be derived from the energy dispersion relation and it is found to be zero at Fermi level [20]. Along with the zero bandgap, this is why graphene is a zero bandgap semiconductor.

2.3.2 Electronic band structure of SWNTs

A SWNT can be uniquely identified by a chiral vector $\boldsymbol{C} = n_1\boldsymbol{a}_1 + n_2\boldsymbol{a}_2$, where n_1 and n_2 are integers and $\boldsymbol{a}_1$ and $\boldsymbol{a}_2$ are the unit vectors of the graphene lattice (figure 2.6).

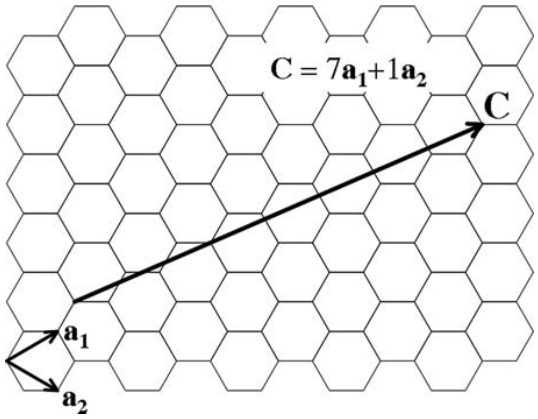

Figure 2.6 – Representation of the chiral vector identifying a (7,1) SWNT.

A SWNT is formed by rolling a graphene sheet so that two carbon atoms pointed by C coincide. The integers n_1 and n_2, which are also called wrapping indices, uniquely define and describe a SWNT. SWNTs described by wrapping indices (n, n) and $(n, 0)$ are called armchair and zigzag SWNTs, respectively.

The band structure of a SWNT can be derived from that of graphene by imposing an appropriate boundary condition around the SWNT. Considering a SWNT as an infinitely long cylinder, there exist two wave vectors associated with it. The wave vector $k_{\parallel}$, which is parallel to the SWNT axis, is continuous since the SWNT is assumed to be infinitely long, while the wave vector $k_{\perp}$, which is along the circumference of the SWNT, must satisfy a periodic boundary condition, since the wave function repeat itself as it rotates 2π around the SWNT.

This boundary condition can be expressed as:

$$\mathbf{k}_{\perp} \cdot \mathbf{C} = \pi d k_{\perp} = 2\pi m$$

where d is the diameter of a SWNT and m is an integer. This boundary condition leads to quantized values of allowed $k_{\perp}$ for SWNTs. The 1D band structure of SWNTs can be obtained from cross-sectional cutting of the energy dispersion of 2D graphene with these allowed $k_{\perp}$ states. This approach is called zone folding scheme and it allows to obtain the band structure of SWNT. Each cross-sectional cutting gives rise to a 1D subband. Therefore, the 1D band structures of SWNTs are determined by the spacing between allowed $k_{\perp}$states and their angles with respect to the surface Brillouin zone of graphene, which is set by the diameter and chirality of SWNTs, i.e. the wrapping indices.

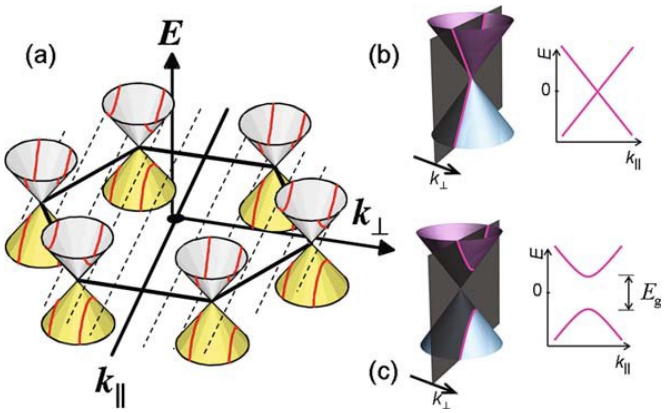

Figure 2. 7 – (a) A first Brillouin zone of graphene with conic energy dispersions at six K points. The allowed $k\perp$ states in a SWNT are indicated by dashed lines. The band structure of a SWNT is obtained by cross-sections as indicated. Zoom-ups of the energy dispersion near one of the K points are schematically shown along with the cross-sections by allowed $k\perp$ states and resulting 1D energy dispersions for (b) a metallic SWNT and (c) a semiconducting SWNT.

The band structure near the Fermi level, which determines the transport properties, is given by allowed $k_\perp$ states that are closest to the K points. When the allowed $k_\perp$ pass directly through the K points (figure 2.7b), the energy dispersion shows two linear bands crossing at the Fermi level without a bandgap. Otherwise, if the allowed $k_\perp$states fall far from the K points (figure 2.7c), there are two parabolic 1D bands with an energy bandgap. Therefore, depending on the wrapping indices, SWNTs can have a band structure with or without a bandgap, therefore they can be semiconducting or metallic, respectively.

Considering, as example, the 1D subbands of a zigzag SWNT, described by wrapping indices $(n, 0)$ which can be either metallic or semiconducting; the chiral vector $\mathbf{C}$ for a zigzag nanotube is $\boldsymbol{C = n a_1}$ and the boundary condition becomes:

$$k_x na = 2\pi m$$

When n is a multiple of 3 ($n = 3q$, where q is an integer), there is an allowed k_x that coincides with a K point, which is at $(0, 4\pi/3a)$. By substitution,

$$k_x = \frac{2\pi m}{na} = \frac{3Km}{2n} = \frac{Km}{2q}$$

Then, there is always an integer m $(= 2q)$ that makes k_x pass through K points so that these zigzag SWNTs (with $n = 3q$) are always metallic without a bandgap.

There are two cases when n is not a multiple of 3. If $n = 3q + 1$, the k_x closest to K point is at $m = 2q + 1$:

$$k_x = \frac{2\pi m}{na} = \frac{3Km}{2n} = \frac{3K\,(2q+1)}{2\,(3q+1)} = K + \frac{K}{2}\,\frac{1}{3q+1}$$

Similarly, for $n = 3 - 1$, the allowed k_x closest to K is when $m = 2q - 1$:

$$k_x = \frac{2\pi m}{na} = \frac{3Km}{2n} = \frac{3K\,(2q-1)}{2\,(3q-1)} = K - \frac{K}{2}\,\frac{1}{3q-1}$$

In these two cases, allowed k_x misses K points by:

$$\Delta k_x = \frac{K}{2}\,\frac{1}{3q \pm 1} = \frac{2}{3}\,\frac{\pi}{na} = \frac{2}{3}\,\frac{\pi}{\pi d} = \frac{2}{3d}$$

The smallest misalignment between an allowed k_x and a K point is inversely proportional to the diameter. Then, the bandgap E_g is given by:

$$E_g = 2 \times \left(\frac{\delta E}{\delta k}\right) \times \frac{2}{3d} = 2\hbar v_F \left(\frac{2}{3d}\right) \approx 0.7\ eV/d(nm)$$

Therefore, semiconducting SWNTs (d = 0.8 – 3 nm) have a bandgap in the order of 0.2 – 0.9 eV, inversely proportional to the diameter. Similar treatment for armchair SWNTs (n, n) leads to the conclusion that they are always metallic.

Using wrapping indices (n_1, n_2), SWNTs can be classified into three different categories depending on the value of p, which is the remainder when the difference between wrapping indices is divided by 3 (i.e. $n_1 + n_2 = 3q + p$):

(i) p = 0; metallic with linear subbands crossing at the K points
(ii) p = 1, 2; semiconducting with bandgap, Eg ~ 0.7 eV/d (nm)

2.3.3 Deviation from simple tight-binding zone folding scheme

In the zone-folding derivation of the electronic band structure of SWNTs, nanotubes are treated as graphene sheet with a periodic boundary condition with the assumption that π orbitals are still orthogonal to σ orbitals in the graphene plane so that π orbitals can be treated independently as in the graphene case. This assumption is not valid for SWNTs because their curvature mixes π and σ orbitals, leading to the hybridization between these orbitals, with the degree of hybridization becoming larger as

the diameter of SWNT gets smaller. The main result of this π-σ hybridization is to open a small bandgap in metallic SWNTs, with the exception of the armchair nanotubes due to symmetry (figure 2.8). This is a secondary effect as the bandgap goes as $1/d^2$, ranging from a few meV to tens of meV for a diameter of ~3 nm or smaller.

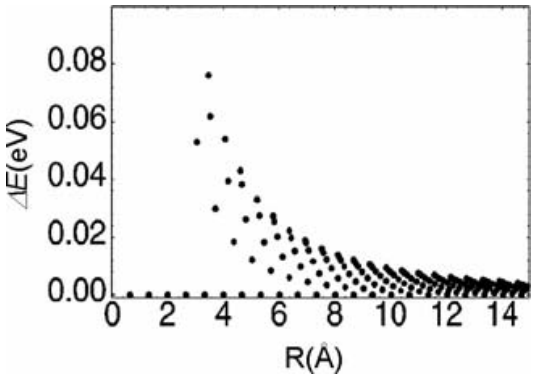

Figure 2.8– The calculated curvature-induced bandgaps for metallic SWNTs. The bandgap is still zero for armchair SWNTs.

2.3.4 Density of States in SWNTs

The DOS is an actual physical quantity that can be measured with different techniques as scanning tunneling microscopy, electrical transport measurements, and optical measurements (photoluminescence). The DOS, *n(E)*, with 1D subbands *ε(k)* can be calculate as:

$$n(E) = \frac{\delta N(E)}{\delta E} = \frac{2}{l}\sum_i \int dk\delta\,(k - k_i)\left|\frac{\delta\varepsilon}{\delta k}\right|^{-1}$$

Where k_i are the roots of the equation $E - \varepsilon(ki) = 0$, l is the length of the 1D Brillouin zone, and *N(E)* is the total number of electron states per unit cell below a given energy *E*. For parabolic 1D subbands such as those of semiconducting SWNTs (figure 2.7c), the resulting DOS is proportional to $1/E^{1/2}$ for each subband and diverges for each onset of a subband, giving rise to the so-called van Hove singularity in 1D systems. In higher dimensionality system DOS goes to zero with $E^{1/2}$ in 3D and over series of step at each inset of a subband in 2D systems (figure 2.9).

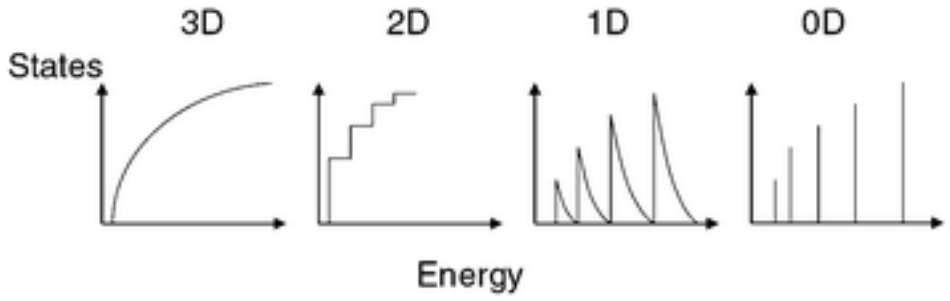

Figure 2.9 – Density of states in systems with different dimensions.

The metallic bands at K points can be approximated by a linear dispersion (figure 2.7b), so they lead to finite, constant DOS.

For SWNTs the equation can be solved as

$$n(E) = \frac{2\sqrt{3}}{\pi^2}\frac{d}{\gamma_0 D}\sum_{m=-\infty}^{\infty} g(E, \varepsilon_m)$$

Where

$$g(E, \varepsilon_m) = \begin{cases} \dfrac{|E|}{\sqrt{E^2 - \varepsilon_m^2}}, & |E| > |\varepsilon_m| \\ 0, & |E| < |\varepsilon_m| \end{cases}$$

$g(E, \varepsilon_m)$ becomes divergent whenever $E = \varepsilon_m$, corresponding to van Hove singularity and $g(E, 0) = 1$. These leads to different 1D density of states for semiconducting and metallic SWNTs (figure 2.10).

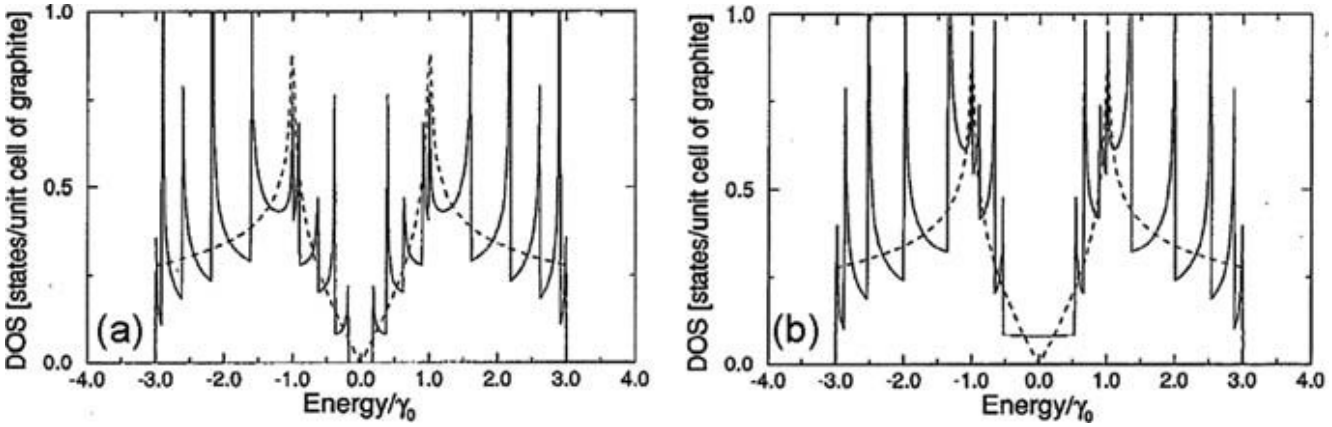

Figure 2.10 – The electronic density of states for a (a) (10, 0) semiconducting and (b) (9, 0) metallic SWNT. Dotted lines are for the density of states of graphene (which is zero at the Fermi level).

While DOS is zero at K points in graphene, it is finite for metallic SWNTs, due to the 1D characteristics of SWNTs. Zero bandgap and finite DOS at the Fermi level entitles metallic SWNTs as truly metallic, unlike graphene.

2.4 Electron Transport in Single Walled Carbon Nanotubes

Resistance in solid system is due to the scattering of charge carriers as they travel through the system. In solid state system, main sources of scattering are static defects (imperfection, impurities…) and phonons (lattice vibrations). Usually, scattering of phonons is dominant at high temperature while impurity scattering prevails at low temperatures. In SWNTs there are various sources of carrier scattering affecting transport characteristics.

2.4.1 Scattering in SWNTs

Charge carrier scattering in 1D system is quite different from the one in higher dimensions because carriers can only forward or backward scatter while in higher dimension they can be scattered into many different directions.

In general there are two types of scattering processes in solid systems: one is the scattering by static potentials such as impurities which does not change the energy of the particles being scattered; the other is the scattering by time-varying potential such as phonons which results in inelastic scattering with energy as well as momentum changes.

Scattering by defects or impurities is due to scattering potentials which are generally static in time. The scattering potential can be a screened or unscreened Coulomb neutral defect. Although SWNTs retain high crystallinity, they inevitably have different kinds of structural defects such as vacancies or pentagon-heptagon pairs and impurities such as foreign atoms or chemicals deposited in the surface. Despite these imperfections, metallic SWNTs are expected to have a long mean free path, even at room temperature, and this is attributed to the suppressed back scattering due to high symmetry of SWNTs, especially armchair SWNTs. Metallic SWNTs have two degenerate 1D subbands crossing at the Fermi level. Each subband corresponds to a different moving direction for electrons and backscattering requires electrons move from one subband to the other. Due to symmetry, these two crossing 1D subbands are orthogonal to each other and do not mix resulting in a significant suppression of backscattering in metallic SWNTs. As long as the defects do not significantly perturb the band symmetry of SWNTs, metallic SWNTs have a large mean free path. Defects such boron and nitrogen impurities and pentagon-heptagon pairs are expected to affect the electrical transport properties of metallic SWNTs, but only far away from the Fermi level, while vacancies which have a short range potential seem to affect the transport near the Fermi level.

As scattering due to defects are suppressed in SWNTs, the main source of scattering is believed to be phonons, especially at high temperatures. Various phonon modes exist in SWNTs (figure 2.11).

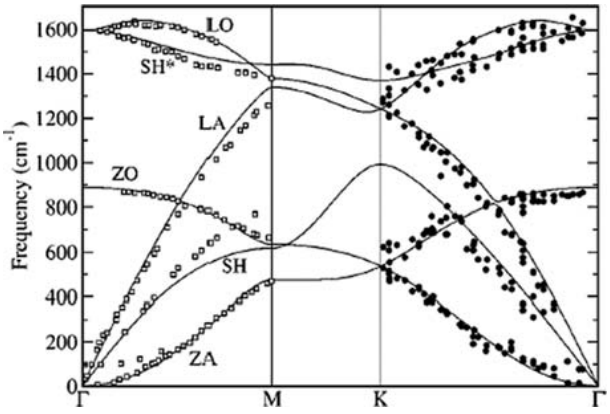

Figure 2.4 – Phonon dispersion relation of graphene

Phonon scattering is an inelastic scattering process which requires the momentum and energy conservations by electrons and phonons combined. Limited momentum space of SWNTs along with the symmetry requirements leave only three possible electron-phonon processes satisfying the momentum and energy conservations (figure 2.12).

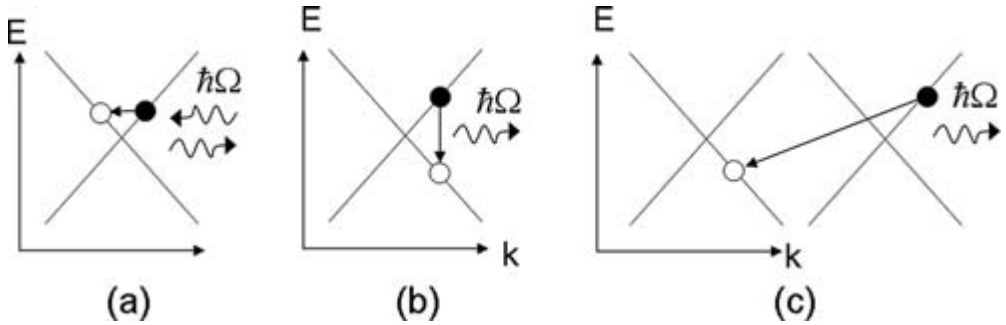

Figure 2.5 – Allowed electron backscattering process in a metallic SWNT by (a) acoustic phonons, (b) optical phonons, and (c) zone boundary phonons with energy $\hbar\Omega$

The first one is scattering by low energy acoustic phonons which involves a small momentum and energy changes. The other two scattering process are due to the high energy optical and zone boundary phonons which require large energy changes (150-180 meV) with small and large momentum, respectively. Phonon scattering involves either emission or absorption of the phonons by traveling charge carriers.

At low electric field acoustic phonon scattering (a) is the only available scattering process since electrons do not have enough energy to interact with the high-energy phonons. In this regime, resistance is inversely proportional to the temperature since the scattering rate is determined by number of phonons available and the occupation of acoustic phonons is proportional to the temperature. Due to their high energy, compare to the room temperature, $k_BT \sim 25$ meV, the optical and zone boundary phonons are not expected to be present at room temperature so that the scattering in this case corresponds to only the emission of phonons by electrons.

At high electric fields, electrons can acquire enough energy to emit optical and zone boundary phonons, which results in the backscattering of electrons. As long as the mean free path for high energy phonon scattering is much smaller than the SWNT length, it can be assumed that electrons backscatter instantly when they acquire enough energy to emit high-energy phonons.

2.5 Optical Properties of Single Walled Carbon Nanotubes

Optical properties of single-walled nanotubes are governed by the extended π-electron system. The available electronic states in such π-system reflect the unusual band structure of nanotubes which varies with the (n,m) values describing each nanotube's structure, meaning that each physical SWNT structure has its own characteristic electronic structure. The diversity of electronic properties and their strong dependence on nanotube structure constitute one of the most remarkable and potentially useful features of SWNTs, which must be viewed as a family of related materials rather than a single substance such as C_{60}.

SWNTs for which n = m have a finite density of states at the Fermi energy and display metallic electronic behavior. Other structures for which the quantity (n–m) is evenly divisible by 3 are semimetallic, with band gaps smaller than k_BT at room temperature, whereas SWNT in which (n–m) does not divide evenly by 3, are semiconductors with their bandgap varying approximately inversely with nanotube diameter. Nanotubes with the same (n,m) identity but different lengths have matching optical and electronic properties because SWNT electronic structure is governed by transverse structure. The quasi-one-dimensionality of nanotubes has an important electronic consequence for all (n,m) species: it introduces sharp spikes, called van Hove singularities, into the densities of states (figure 2.13).

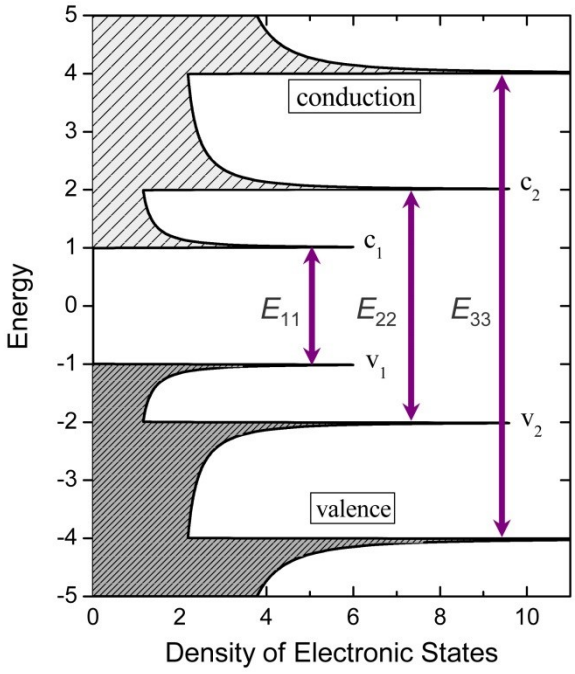

Figure 2.63 –Schematic density of states diagram for a semiconducting single-walled carbon nanotube, in a simple band theory model. Allowed optical transitions are illustrated as vertical arrows.

Figure 2.13 shows a band theory model density of states function for a semiconducting SWNT [21]. Each van Hove singularity belongs to a different sub-band. Optical absorption and emission are dominated by dipole-allowed transitions in which light polarized with its electric vector parallel to the tube axis promotes an electron from a valence subband to the corresponding conduction sub-band, conserving the angular momentum projection. In a one-electron model, these transitions are predicted to be most intense when the photon energy matches the energy difference between corresponding van Hove singularities. The absorption and emission spectra of a single (n,m) species of SWNT are therefore expected to consist mainly of a series of sharp features at energies E_{ii}, where i takes the values 1, 2, 3, according to subband.

2.5.1 Absorption of SWNTs

For semiconducting SWNTs with diameters near 1 nm, the first three of these transitions will appear in the near-infrared, visible, and near-ultraviolet regions. Metallic or semimetallic SWNTs of similar diameter have their lowest energy optical transitions at visible wavelengths falling between the semiconducting nanotubes' E_{22} and E_{33} features. In addition, semimetallic nanotubes also have much lower energy absorptions in the far-infrared at wavelengths near 100 mm [22,23]. These correspond to transitions across the small, diameter-dependent band gaps (in the range of 10 meV) that are induced by s–p hybridization associated with the nanotubes' cylindrical curvature [24]. Apart from the nondispersive interband optical transitions in the infrared and visible that are characteristic of nanotube diameter and chiral angle, SWNT samples also display dispersive, intense near-ultraviolet absorptions at 4.5 and 5.2 eV that have been assigned to collective plasmon excitations of their p-electrons [25,26].

The near-infrared and visible transitions of SWNTs would be expected to be quite useful in distinguishing different structural species from one another. However, it was found that spectra of samples containing many species typically showed broad, undifferentiated optical absorption features arising from strongly overlapped transitions of those species, rather than sharp, resolved absorptions. In addition, no emission was observed that could be assigned to van Hove interband transitions.

A breakthrough in nanotube spectroscopy occurred with the 2002 report of structured absorption from samples of SWNTs that had been prepared with special processing to counteract their strong tendency to form bundles of parallel nanotubes held together by van der Waals forces [27]. To obtain these disaggregated samples, raw and unpurified product from the HiPco process was first mechanically dispersed into an aqueous solution of a surfactant such as SDS (sodium dodecylsulfate). Then intense ultrasonic agitation was applied to free many individual nanotubes from bundles. Once freed, the nanotubes became surrounded by a micelle-like layer of surfactant molecules that prevented their reaggregation into bundles. Finally, the sample was subjected to ultracentrifugation, which allowed significant physical separation of suspended individual nanotubes from the slightly denser suspended bundles. Decanted portions of such processed samples showed notably complex and sharpened near-infrared absorption spectra with structure extending from approximately 900 to 1600 nm (figure 2.14). D2O was used in preference to H2O as the solvent for spectroscopic studies because of its superior

near-infrared transparency. The isotopic frequency shift of the O–H stretching overtone increases the long wavelength cut-off of D2O to ca. 1900 nm from 1350 nm in H2O.

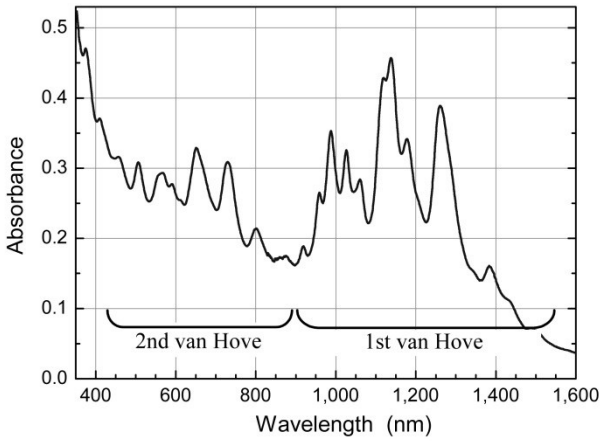

Figure 7.14 – Optical absorption spectrum of a sample of HiPco single-walled carbon nanotubes suspended in D2O by SDS surfactant at 276 K.

2.5.2 Emission of SWNTs

These aqueous samples enriched in individual surfactant-suspended SWNTs also displayed near-infrared photoluminescence with highly structured emission spectra showing a series of peaks nearly coincident with those in the absorption spectrum (figure 2.15). The emission red-shifts are only approximately 4 meV (30 cm_1).

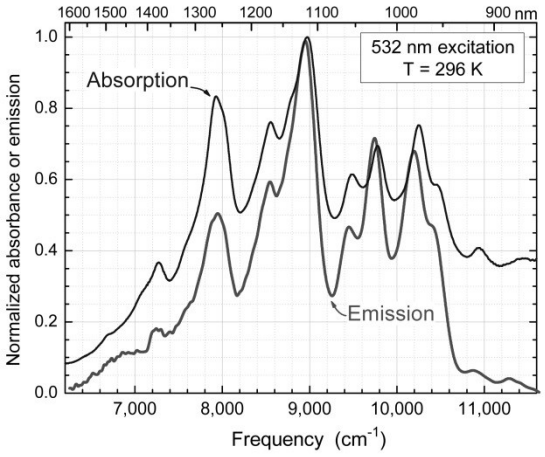

Figure 2.15 – Absorption and emission spectra of a sample of HiPco nanotubes in SDS/D2O suspension. The emission was excited by a pulsed laser at 532 nm.

This similarity of absorption and emission spectra differs strikingly from the ‘‘mirror-image’’ relation that is common in molecular photophysics. The data show that the sample contains many emitting species, with each displaying one dominant transition in this spectral range and a very small Stokes shift between its absorption and emission peaks. In accord with the predictions of Kasha's Rule that molecular electronic luminescence originates entirely from the lowest-lying electronic state within a spin multiplicity manifold [28], SWNT emission is observed exclusively for E_{11} transitions and not for E_{22} or higher transitions. Clearly, the many distinct spectral features in the E_{11} region correspond to different (n,m) species of semiconducting single-walled nanotubes in the structurally heterogeneous sample. Precise values of photoluminescence quantum yields are difficult to measure, in part because of overlapping transitions in mixed samples. However, initial estimates suggest quantum yields that are near 10^{-3} and vary somewhat as the nanotube's environment is altered by the presence of different surfactants. Lifetime studies on SWNT optically excited states have been reported by several laboratories [29–31]. The excited state lifetime of ca. 10^{-10} s can be combined with the emissive quantum yield near 10^{-3} to deduce that the emitting state has a radiative rate constant consistent with a spin-conserving optical transition. Using the terminology of molecular photophysics, nanotube photoluminescence is therefore classified as fluorescence rather than phosphorescence.

Only semiconducting SWNTs emit fluorescence, because the nonzero density of states in metallic species causes non radiative recombination of the photoinduced excitons (figure 2.16).

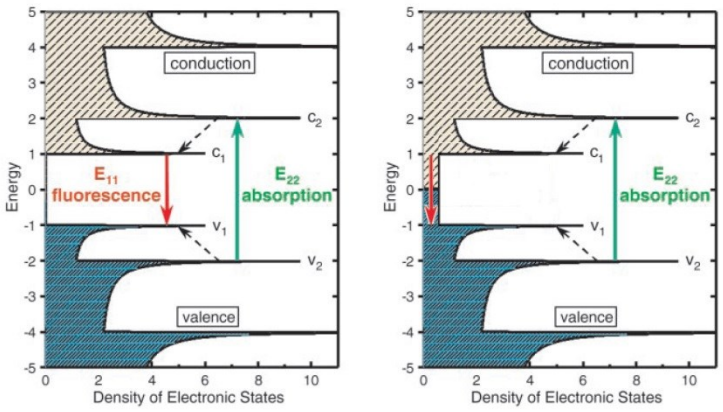

Figure 2.16 – Schematic density of electronic states for a single nanotube structure. For semiconducting species (left), excitation is followed by fluorescence upon phonon relaxation (dashed arrows). For metallic species (right), excitation is followed by non radiative decay because of the non-zero density of states at the Fermi level.

The near infrared emission due to a fluorescent bandgap transition can therefore be used for the identification of the specific nanotubes structure responsible for each peak. This was obtained using spectrofluorimetry, reporting the measured emission intensity as a function of two variables: excitation and emission wavelength. The excitation source's wavelength was scanned over the range of E_{22} transitions, and when the photon energy matched the second van Hove transition energy of one of the

SWNT species in the sample, the resulting optical absorption generated a hole in its second valence sub-band and an electron in its second conduction sub-band. The electrons and holes relaxed through phonon emission to the first sub-bands. Then a small fraction of the excited nanotubes emitted E_{11} near-infrared fluorescence through radiative electron–hole recombination across the semiconducting band gap. The wavelength of this emission was characteristic of the nanotube species that had undergone resonant E_{22} excitation.

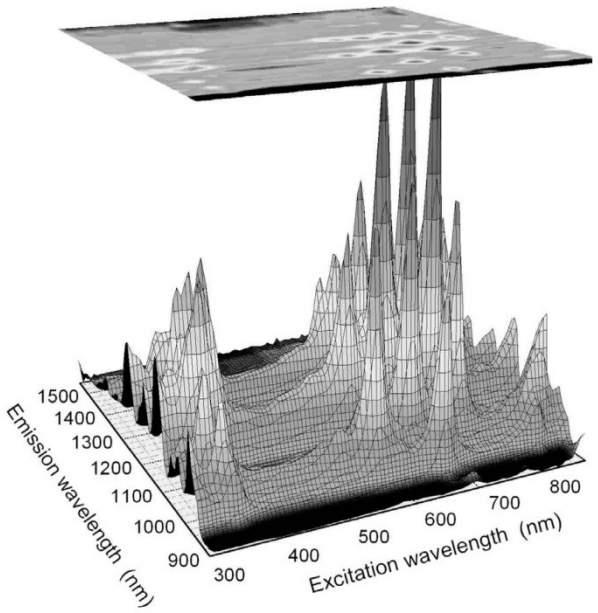

Figure 2.17 – Surface plot showing emission intensity from a sample of HiPco SWNT in SDS/D2O suspension as a function of excitation and emission wavelengths. Each distinct peak arises from a specific (n,m) species of semiconducting nanotube.

The results from this experiment can be summarized in the form of a surface plot, where height corresponds to emission intensity and the two other axes represent excitation and emission wavelengths (figure 2.17). A rich structure of ‘‘mountain peaks’’ is clearly evident for excitation in the E_{22} range between ca. 500 and 800 nm. Each of these peaks arises from a distinct (n,m) species of semiconducting nanotube. The unique E_{11} and E_{22} transition energies of each species may be simply found from the wavelength coordinates of its peak, providing a valuable correlation of E_{11} and E_{22} values for many different nanotube species.

Fluorescence is the optical property of nanotubes that is most sensitive to sample condition. The absence of near-IR emission from nanotubes that have aggregated into bundles held together by van der Waals forces seems likely to arise from efficient energy transfer within the bundle. Statistically, approximately one-third of the nanotubes in a raw sample are expected to be metallic. There is therefore a high probability that randomly formed bundles containing at least several nanotubes will include one or more metallic tubes. When a bundled semiconducting SWNT absorbs light, electronic coupling with its neighbors causes excitation transfer to species with smaller band gaps and eventually

to a metallic nanotube, in which the excitation must relax nonradiatively. This efficient fluorescence quenching process allows one to use emissive yield as a sensitive monitor of SWNT aggregation.

Fluorescence efficiency can also be sensitive to chemical environment. The addition of acid to aqueous suspensions of pristine SWNT in ionic surfactants causes fluorescence quenching that can be reversed by the addition of base to restore pH to a neutral or alkaline value [32–34]. Such quenching differs from the complete and essentially irreversible loss of near-infrared fluorescence caused by many oxidative acid treatments that are commonly applied to raw SWNT material to remove residual metallic catalysts. In addition, many chemical reactions that derivatize nanotube sidewalls inhibit fluorescence. It seems likely that the perturbation of a nanotube's π-electron system by the chemical conversion of functionalized carbon atoms from sp^2 to sp^3 hybridization produces sites for efficient nonradiative recombination of excitons. Although such chemical derivatization also leads to the characteristic D-band in Raman spectra and the loss of van Hove structure in electronic absorption spectra, fluorescence is lost significantly before the onset of these other spectroscopic symptoms. This high sensitivity of fluorescence quantum yield to sidewall defects may reflect the mobility of excitons along the tube axis. Through such motion the electronic excitation can visit relatively large segments of a nanotube during its lifetime and undergo efficient quenching by sparse defect sites.

2.6 Raman Spectroscopy of Single Walled Carbon Nanotubes

Raman spectra of SWNTs contain many features that can be identified with specific phonon modes and with specific Raman scattering processes that contribute to each feature. The Raman spectra of SWNTs can therefore provide much information about 1D properties, such as their phonon structure and their electronic structure, as well as information about sample imperfections (defects). Since mechanical properties, elastic properties and thermal properties also are strongly influenced by phonons, Raman spectra provide much general information about the structure and properties of SWNTs.

2.6.1 Phonon structure

Phonons denote the quantized normal mode vibrations that strongly affect many processes in condensed matter systems, including thermal, transport and mechanical properties.

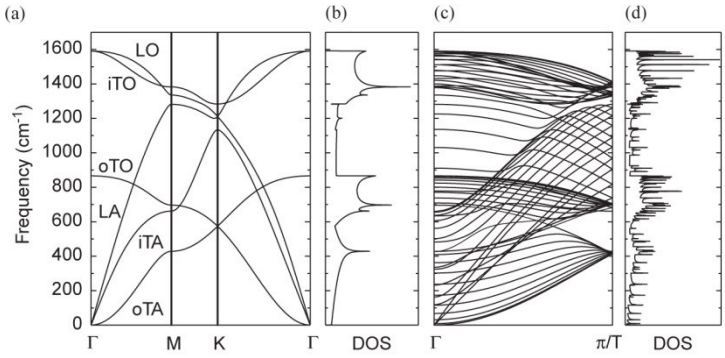

Figure 2.18 – (a) Phonon dispersion of 2D graphite [35]. (b) The phonon density of states for a 2D graphene sheet. (c) The calculated phonon dispersion relations of an armchair carbon nanotube with (n, m) = (10, 10), for which there are 120 degrees of freedom and 66 distinct phonon branches [17], calculated from (a) by using the zone folding procedure. (d) The corresponding phonon density of states for a (10,10) nanotube.

The 2D graphene sheet has 6 phonon branches, as shown in figure 2.18a. Since the SWNTs can be considered to be a 2D graphene sheet that has been rolled up seamlessly, a similar folding procedure, as was used for describing the electronic structure, is generally applied to obtain the phonon dispersion relations and phonon density of states for SWNTs from those of the 2D graphene sheet **[17]**.

The phonon dispersion for a (10,10) SWNT obtained by this folding procedure is illustrated in figure 2.18 c, and the respective phonon DOS is shown in figure 2.18d. The large amount of sharp structure in the phonon density of states in figure 2.18d for the (10,10)SWNT reflects the many phonon branches and the 1D nature of SWNTs relative to 2D graphite arising from the quantum confinement of the phonon states into van Hove singularities. The phonon density of states for 2D graphite is shown in figure 2.18b for comparison.

2.6.2 Raman Scattering Process

Raman scattering is the inelastic scattering of light. During a scattering event, (1) an electron is excited from the ground level to a virtual excited state by absorbing a photon, (2) the excited electron is scattered by emitting (or absorbing) phonons, and (3) the electron relaxes to the ground level by emitting a photon. Raman scattering can occur for phonon emission or by phonon absorption, and these two processes are called the Stokes process and anti-Stokes process, respectively. If light scattering occurs elastically, i.e. change of photon direction but no frequency shift, the process is called Rayleigh scattering (figure 2.19).

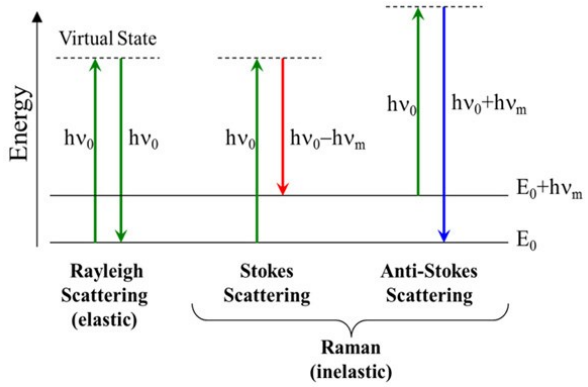

Figure 2.19 – Elastic and inelastic light scattering giving Rayleigh and Raman scattering , respectively.

Raman spectra generally report the scattered photon (light) whose energy is smaller by the phonon energy than that of the incident photon, i.e. Stokes scattering. By measuring the intensity of the scattered light as a function of frequency downshift (losing energy) of the scattered light, an accurate measure of the phonon frequencies of the material is obtained.

2.6.3 Resonance and non-resonance Raman scattering

When the energy separation between the ground and excited states is not equal to the photon energy and photon absorption process occurs through a final virtual state, the transition is called a virtual transition and the Raman process is non-resonant.

When the optical absorption (or emission) is to (or from) a real electronic state, the transition is resonant and its scattered amplitude becomes very large, giving a resonant Raman scattering.

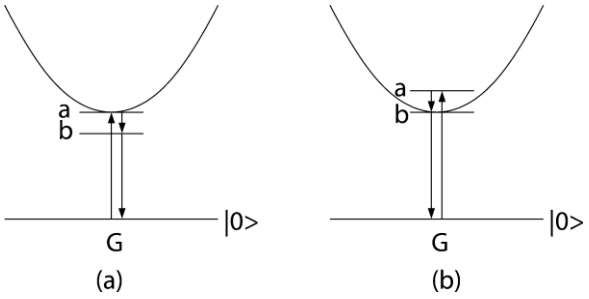

Figure 2.20 – Incident resonance (left) and scattered resonance (right) processes.

There are two resonance conditions for optical transitions: resonance with the incident laser photon (incidence resonance) and resonance with the scattered photon (scattered resonance) (figure 2.20).

When the resonance occurs with the incident photon, the incident laser light has the same energy (E_L) as the energy separation between the two electronic states in resonance (E_{ii})

$$E_L = E_{ii}$$

In this case, all Raman features are resonantly enhanced.

When the resonance occurs with the scattered photon, the incident laser light has the same energy (E_L) as the energy separation between the two electronic states in resonance (E_{ii}), with an additional energy of the phonon $\hbar\omega_i$.

$$E_L = E_{ii} + \hbar\omega_i$$

In this case the resonance condition depends on the phonon energy $\hbar\omega_i$.

Thus in the Stokes Raman process, the shift in the resonant energy for the scattered resonance state is larger than that for incident resonance state by the phonon energy.

Non-resonant Raman spectra are much weaker in intensity than resonance Raman spectra. The resonance Raman process increases the signal by a factor of approximately 10^3 in comparison to the intensity for a non-resonance Raman process. In the case of SWNTs, not only resonant enhancement but also a singularity in the DOS contributes to the Raman intensity. When the laser energy of either the incident or the scattered light has the same energy as a van Howe singularity energy in the JDOS, the Raman intensity becomes extremely strong for any SWNT that satisfies the resonance condition. This is the reason why it is possible to get a measurable signal from a single isolated SWNT in the presence of many non-resonant *(n, m)* SWNTs.

2.6.4 Classification of Raman scattering processes

The number of emitted phonons before relaxation of the lattice can be one, two, and so on, giving, respectively, one-phonon, two-phonon and multi-phonon Raman processes. The order of a scattering event is defined as its number in the sequence of the total scattering events, including elastic scattering by an imperfection (such as a defect or edge) of the crystal.

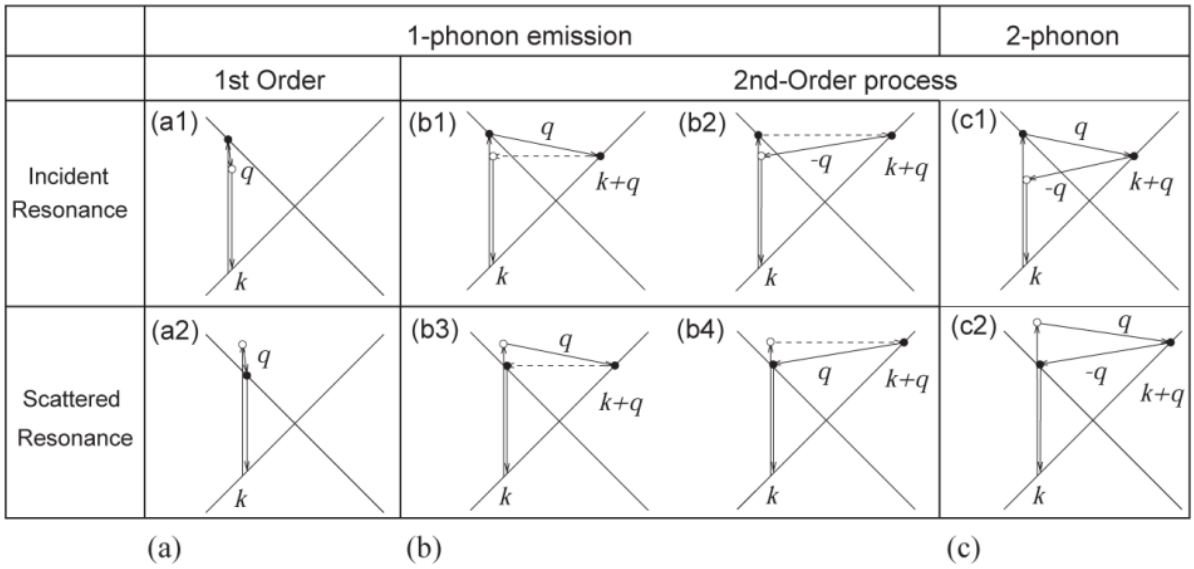

Figure 2. 21 – (a) First-order and (b) one-phonon second-order, (c) two-phonon second-order, resonance Raman spectral processes. (top) incident photon resonance and (bottom) scattered photon resonance conditions. For one-phonon, second-order transitions, one of the two scattering events is an elastic scattering event (dashed lines). Resonance points are shown as solid circles.

The lowest order process is the first-order Raman scattering process which gives Raman spectra involving one-phonon emission (figure 2.21a). In order for an electron to recombine with a hole, the scattered **k** + **q** states should not differ from **k** by more than two times the photon wave vector.

In second-order Raman scattering, **q** and −**q** scattering wave vectors are involved, so that an electron can return to its original **k** position after scattering. The electron absorbs a photon at a **k** state, scatters to **k** + **q** states, scatters back to a **k** state, and emits a photon by recombining with a hole at a **k** state. The two scattering processes consist of either elastic scattering by defects of the crystal or inelastic scattering by emitting a phonon, characterizing, respectively, one- and two-phonon double-resonance Raman process.

Second-order Raman scattering consists of one-phonon and one elastic scattering event (figure 2.21b) or two-phonon scattering events (figure 2.21c). In the case of two-phonon scattering events, it can be involved the same phonon modes (overtone mode) or different phonon modes (combination mode).

2.6.5 Raman spectra of SWNTs

Raman spectra of SWNTs are characterized by many features that can be identified with specific phonon modes and with specific Raman scattering processes (figure 2.22).

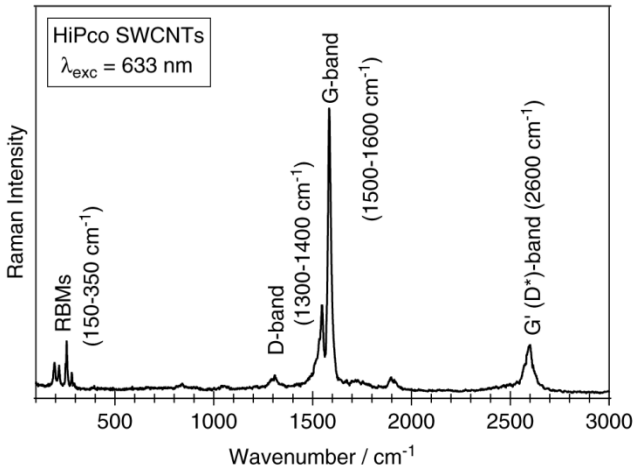

Figure 2.22 – Raman spectrum of a HiPco SWNTs

In SWNTs, the G-band spectra, which is split into many features around 1580 cm^{-1}, and the lower frequency radial breathing modes (RBMs) are usually the strongest features in SWNT Raman spectra, and are both first-order Raman modes. The D-band at 1350 cm^{-1} and the G'-band at 2700 cm^{-1} (for E_L = 2.41 eV) are, respectively, due to one- and two-phonon, second-order Raman scattering processes.

2.6.5.1 Radial Breathing Modes

The radial breathing mode (RBM) Raman features is a totally symmetric vibrational mode associated with the coherent vibration of the C atoms in the radial direction with respect to the nanotube axis (figure 2.23).

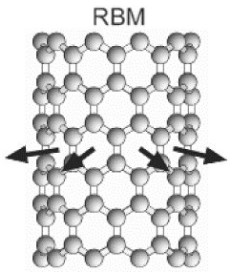

Figure 2.23 – Radial breathing mode in SWNT.

These features are unique to carbon nanotubes and occur with frequencies (ω_{RBM}) between 120 and 350 cm^{-1} for SWNTs with diameter in the range 0.7 nm < d_t < 2 nm. Theoretical and experimental results show that the ω_{RBM} is inversely proportional to the nanotube diameter d_t but does not depend on the chiral angle of the tubes. These RBM frequencies are therefore useful for verifying the presence of SWNTs through the presence of RBM modes and for characterizing the nanotube diameter distribution in the sample through the relation:

$$\omega_{RBM} = A/d_t + B$$

where A and B parameters are determined experimentally [36,37]. (B is an upshift in ω_{RBM} assigned to tube-tube interactions). For typical SWNT bundles in the diameter range $d_t = 1.5 \pm 0.2$ nm, A = 234 cm^{-1} and B = 10 cm^{-1} has been found **[**37**]**. For dispersed SWNTs in aqueous solution, A = 239, B = 0. For isolated SWNTs on an oxidized Si substrate, A = 248 cm^{-1} and B = 0 has been found [36,38]. These two set of values of A and B give similar d_t for a given ω_{RBM} only if the diameter is comprised between 1 a 2 nm. When d_t < 1 nm, the distortions of nanotube lattice lead to a chirality dependence of ω_{RBM}. For d_t > 2 nm the intensity of RBM features is weak and difficult to observe. Therefore, from the ω_{RBM} measurement of an individual isolated SWNT, it is possible to obtain a value of its diameter d_t. The RBM spectra for SWNT bundles contain an RBM contribution from different SWNTs in resonance with the excitation laser line.

Single Raman measurement gives an idea of the tubes that are in resonance with the laser line, but does not give a complete characterization of the diameter distribution of the sample. A good characterization of the diameter distribution can be obtained taking Raman spectra using many laser lines. Since semiconducting and metallic tubes of similar diameter do not occur at similar E_{ii} values, ω_{RBM} measurement using several E_L can be used to characterize the ratio of metallic to semiconducting SWNT in a given sample.

2.6.5.2 G-band

The G-band involves an optical phonon between the two dissimilar carbon atoms A and B in the unit cell and it is common to all sp^2 carbon system. In graphite G-band shows one single Lorentzian peak at 1582 cm^{-1} whereas SWNTs G-band is composed of several peaks because of the phonon wave vector confinement along the SWNT circumferential direction and due to symmetry-breaking effects associated with SWNT curvature. The G-band frequency can be used for diameter characterization, to distinguish between metallic and semiconducting SWNTs, through strong differences in their Raman lineshapes.

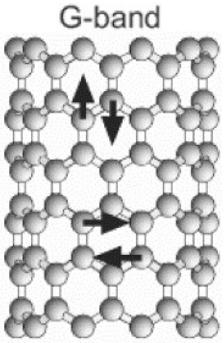

Figure 2.24 – Tangential and circumferential vibration modes responsible of G-band splitting in SWNTs.

G-band feature for SWNTs consists of two main components, one peaked at 1590 cm^{-1} (G^+) and the other peaked at about 1570 cm^{-1} (G^-). The G^+ feature is associated with carbon atom vibrations along the nanotube axis while the G^- feature, in contrast, is associated with vibrations of carbon atoms along the circumferential direction of the SWNT (figure 2.24).

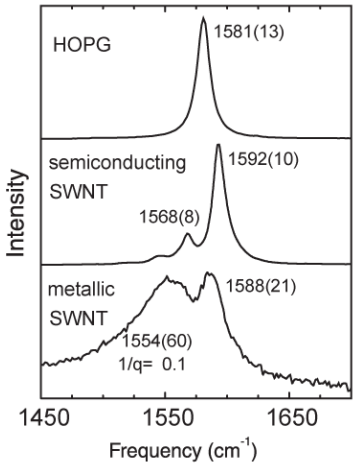

Figure 2.25 – The G-band for highly oriented pyrolytic graphite (HOPG), one semiconducting SWNT and one metallic SWNT.

For individual semiconducting SWNTs, both features exhibit a Lorentzian lineshape. The position of the higher energy component G^+ is almost independent of diameter, whereas the lower energy component G^- shows a clear diameter dependence, where the wavenumber of the mode decreases with decreasing tube radius. For metallic tubes, the G^- component is widely broadened and asymmetric. This broadening is commonly attributed to a Breit-Wigner-Fano (BWF) resonance of metallic SWNTs induced by a coupling of the phonon excitation to a continuum of plasmon states (figure 2.25).

Experimentally, it was shown that the intensity of the BWF component exhibits a diameter dependence as well [39] (figure 2.26).

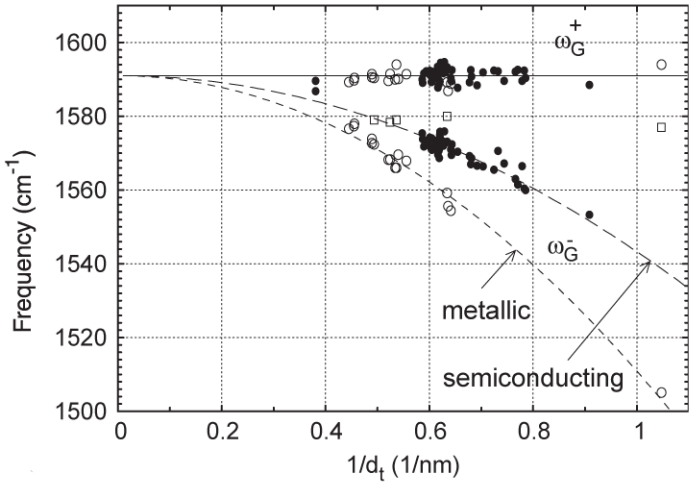

Figure 2.26 – Frequency vs. 1/dt for the two G-band features (G^+ and G^-) from isolated SWNTs

For an ensemble of metallic and semiconducting SWNTs, the resonance condition determines the lineshape of the G^- component. If, for a given diameter distribution, the excitation energy probes predominantly metallic SWNTs, an asymmetric BWF component is observed in contrast to photon energies where excitations of semiconducting SWNTs prevail.

2.6.5.3 D-Band

Disorder-induced (or defect-induced) D-band is the most common example of a second-order feature in the Raman spectra of SWNTs. This band is usually observed between 1300-1400 cm^{-1}. The D band is common to all sp^2-hybridized disordered carbon materials. In SWNTs D-band becomes active because of the presence of defects, such as impurities, missing atoms or sp3-hybridized functionalized carbon atom on SWNT sidewalls. The D-band frequency ω_D shows a strong dependence on the excitation laser energy. This dispersive behavior is explained through a double-resonance process where the electron after being promoted because of photon absorption, is scattered by a phonon and elastically scattered

back by a defect, or vice versa, then recombining with the previously created hole and finally emitting a scattered photon.

D-band is commonly used for a qualitatively defect characterization because it is known to originate from defects but until now there is no correlation between D-band and the different type of defects such as hetero-atoms, vacancies, heptagon-pentagon pairs, kinks, or other impurities [40].

Isolated SWNTs exhibit different ω_D values for a given E_L, because the double resonance condition must be satisfied for each tube. Therefore, D-band for a sample composed of an ensemble of nanotubes is the sum of different features originating from different (n, m) species of nanotubes and for resonances with different E_{ii}. A diameter dependence of ω_D is also observed, with ω_D decreasing with decreasing diameter ($1/d_t$ dependence). In isolated SWNTs, a large D peak compared to the G peak usually indicates a bad resonance condition, which is E_L is not close to E_{ii}. In SWNT bundles a large D-band indicates the presence of amorphous carbon. D features correlated to isolated nanotubes have usually small linewidths, between 40 and 7 cm^{-1}, while amorphous carbon is responsible of a broad feature.

2.6.5.4 G'-band

The G'-band is the second harmonic of the D-band, occurring at ~$2\omega_D$ (~ 2700 cm^{-1}) because the electron is backscattered by a second phonon instead than of a defect, leading to a two-phonon, second-order Raman scattering processes. So defect are no longer necessary and G'-band is present even in defect-free nanotubes for which the D band is completely absent. As for D-band, the G'-band is sensitive to the SWNTs diameter and chirality, so measurement on isolated nanotubes allow the assignment of the indices (n, m).

2.6.5.5 D/G Ratio

Changes in the D-band Raman spectra can be used for SWNTs characterization to probe and monitor structural modifications of the nanotube sidewalls like the introduction of defects. Sample purity is traditionally investigated by comparing the amplitude of the D mode to that of the G mode [41,42], which, as a first-order process, is supposed to be independent of defect density. Therefore the D/G band intensity ratio in SWNTs Raman spectra is conventionally used as an average estimation of sample's defects, including the presence of amorphous carbon and defects like vacancies or functional groups covalently attached on nanotube sidewalls.

2.7 Synthesis of Single Walled Carbon Nanotubes

The most widely used techniques for SWNTs are: arc-discharge, laser ablation and synthesis by chemical CVD. SWNTs can only be grown with a catalyst. Transition metal (Fe, Co, Ni) are the most commonly used catalyst for SWNTs growth. The detailed mechanism responsible for growth are not yet well understood but the width and peak of the diameter distribution depends on the composition of the catalyst, the growth temperature and various other conditions.

2.7.1 Arc-Discharge

The arc-discharge method creates nanotubes through arc-vaporization of two carbon-rod electrodes, separated distant 1 mm from each other, in inert atmosphere (helium or argon) at low pressure (between 50 and 700 mbar) (figure 2.27). A direct current (from 50 to 100 A at 20 V) creates a high temperature discharge between the two electrodes. The discharge vaporizes one of the carbon rods and forms a deposit on the other rod. Nanotubes self-assemble from the resulting carbon vapor. The arc-discharge method yields highly graphitized tubes with structural perfection, because of the very high process temperature around 3000°C. In order to produce SWNTs, the graphite-rod anode has to be doped with metal catalyst. The yield of the process depends strongly on the uniformity of the plasma arc and the temperature of the deposit on the carbon electrode. The arc-discharge method creates also a large amount of by-products, mainly carbonaceous materials, such as amorphous carbon, nanoparticles and fullerenes, which need to be removed in post-synthesis purification processes.

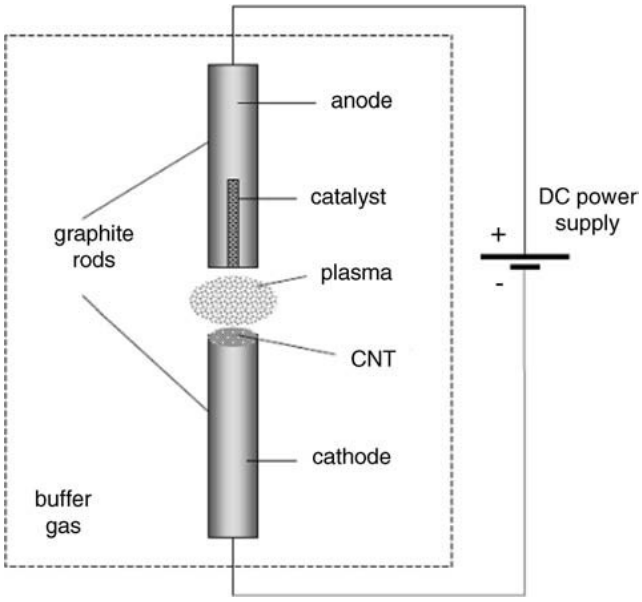

Figure 2.27 - Schematic diagram of an arc-discharge system

2.7.2 Laser-vaporization

In laser vaporization synthesis of SWNTs a pulsed or continuous laser is used to vaporize a graphite target in an oven at 1200°C (figure 2.28). The oven is filled with helium or argon gas in order to keep the pressure at 500 Torr. Upon a laser pulse, a very hot vapor plume forms, then expands and cools rapidly. As the vaporized species cool, small carbon molecules and atoms quickly condense to form larger clusters, possibly including fullerenes. Moreover, a catalyst, present as doping species in the graphite target, helps the growth of nanotubes, probably because the formation of the caps which stop the growth. About 70-90% of the carbon target can be converted to SWNTs. They are mostly produced in the form of bundles consisting of several tubes closely packed in hexagonal lattice held together by van der Waals interactions, with a typical intertube distance of 0.33 nm.

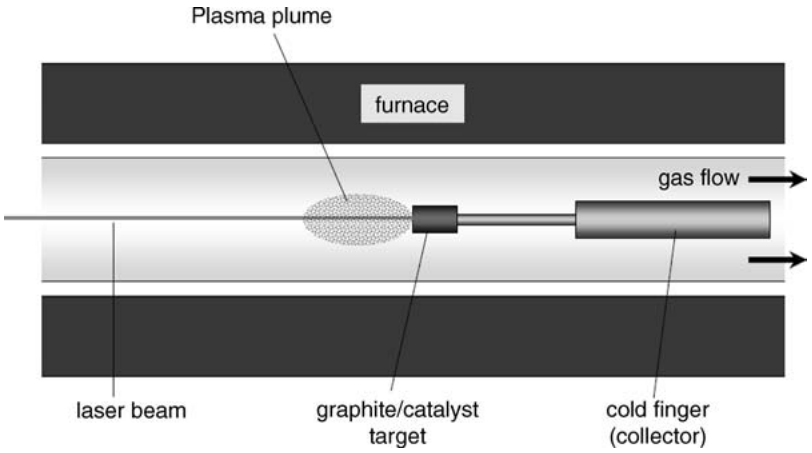

Figure 2.28 - Schematics of a laser ablation setup

2.7.3 Chemical Vapor Deposition

CVD process applies a carbon source in the gas phase through a heated tube furnace over a catalyst material (figure 2.29). Compared with arc-discharge and laser methods, CVD is a simple and economic technique for synthesizing SWNTs at relatively low temperature (600-1200°C) and ambient pressure. It is versatile and can utilize a variety of carbon source in any state (solid, liquid or gas), enables the use of various substrates, and allows SWNTs growth in a variety of forms, such as powder and films. CVD provides the possibility of growing SWNTs from controlled surface sites by catalyst patterning in a desired substrate for specific applications, which is not feasible by arc or laser methods. Therefore this technique is ideally suited for producing arrays of individual or a mat of aligned SWNTs. Commonly used gaseous carbon sources have been methane, acetylene, and carbon monoxide. Liquid carbon sources are typically alcohols, such as methanol or ethanol that are heated in a flask and purged with an inert gas to carry the vapor into the reaction furnace. The use of alcohol has allowed to produce

SWNTs at the relatively low minimum temperature of 550°C. SWNTs were produce from disproportionation of CO at 1200°C, catalyzed from Mo catalyst particles.

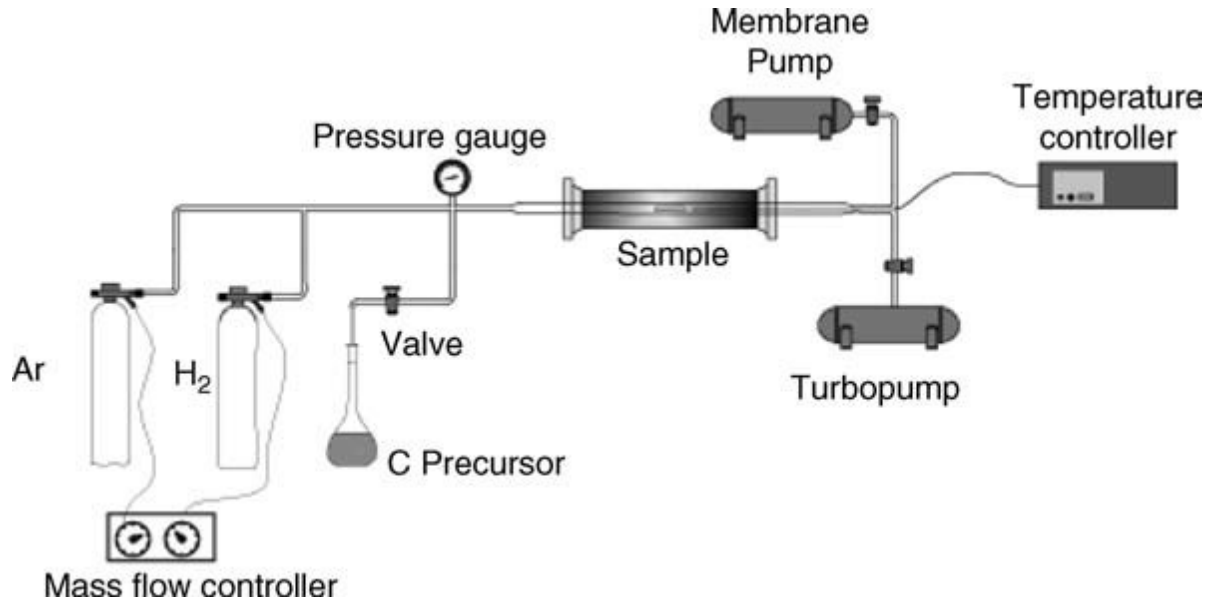

Figure 2.29 - Schematic diagram of a chemical vapor deposition system adapted to work in high vacuum conditions

High temperature (900-1200°C) are generally required for SWNTs growth, so only selected carbon sources stable at this temperature such as CO and methane can be used. The diameter of produced SWNTs is strongly governed by the size of the catalyst particles. Catalyst support material is also an important parameter in CVD nanotube synthesis because of their strong interaction with the catalyst that prevent metal species from aggregating and forming undesirable large cluster that lead to graphite particles of carbon fibers. Most used support materials are zeolites, Al_2O_3, MgO and $CaCO_3$. To improve purity and yield CVD method has been modified as plasma-enhanced CVD, which as the advantage of low temperature synthesis over thermal CVD. Highly controlled growth in terms of height, diameter, placement and alignment of SWNTs has been achieved at around 700 °C and lower. CVD is currently considered to be the most promising in terms of large-scale production because of the control over growth parameter and the ease for up-scaling the production.

2.8 Purification of Single Walled Carbon Nanotubes

As-synthesized SWNTs prepared by the above methods inevitably contain carbonaceous impurities and metal catalyst particles (figure 2.30), and the amount of the impurities commonly increases with the decrease of CNT diameter. Carbonaceous impurities typically include amorphous carbon, fullerenes, and carbon nanoparticles (CNPs). Graphitic polyhedrons with enclosed metal particles also coexist with CNTs synthesized by arc discharge and laser ablation as well as high temperature (T > 1000 °C). Fullerenes can be easily removed owing to their solubility in certain organic solvents. Amorphous carbon is also relatively easy to eliminate because of its high density of defects, which allow it to be oxidized under gentle conditions. The most knotty problem is how to remove polyhedral carbons and graphitic particles that have a similar oxidation rate to CNTs, especially SWNTs. Metal impurities are usually residues from the transition metal catalysts. These metal particles are sometimes encapsulated by carbon layers (varying from disordered carbon layers to graphitic shells) making them impervious and unable to dissolve in acids.

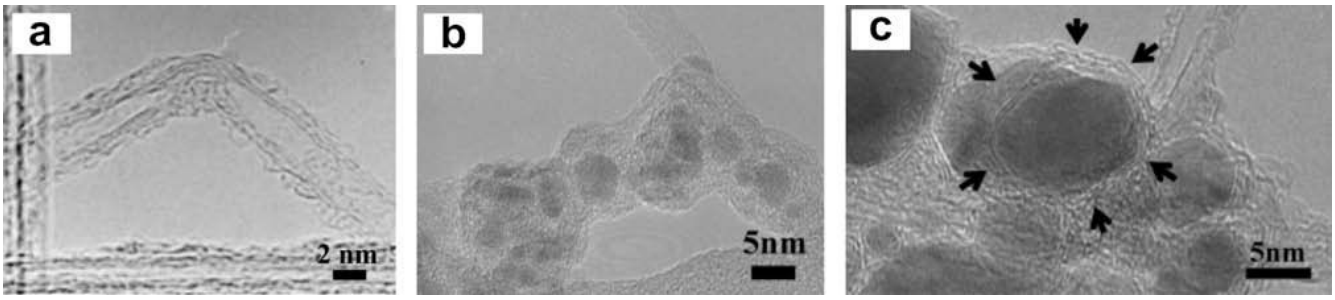

Figure 2.30 – TEM images of (a) amorphous carbon and fullerene molecules on the surface of CNTs [26]; (b) metal nanoparticles covered by amorphous carbon layer, (c) metal nanoparticles covered by graphitic carbon multi-layer [27].

2.8.1 Assessment of SWNTs purity

Rapid, convenient and unambiguous characterization methods are required to evaluate the purity of SWNTs, the efficiency of a purification method as well as changes in the structure during purification. Characterization of SWNT samples falls into three groups: metal catalyst, carbonaceous impurity, and CNT structure variation (defects, functional groups, cap opening, cutting, etc.). Their characterization mainly depends on electron microscopy (EM, including scanning EM (SEM), and transmission EM (TEM)), thermogravimetric analysis (TGA), Raman spectroscopy and ultra violet-visible-near infrared (UV–Vis-NIR) spectroscopy.

- EM is a useful technique allowing for direct observations of impurities, local structures as well as CNT defects, but, owing to the small volume of sample analyzed EM cannot give a quantitative evaluation of the purity of CNTs.

- TGA is effective in evaluating quantitatively the quality of CNTs, in particular, the content of metal impurity. It is easy and straightforward to obtain the metal impurity content using TGA by simply burning CNT samples in air. A higher oxidation temperature (T > 500 °C) is always associated with purer, less defective CNT samples. The real difficulty is qualitative or quantitative assessment of carbonaceous impurity, which is influenced by the amount of defects, forms of carbon, and so on.

- Raman spectroscopy is a fast, convenient and non-destructive analysis technique. To some extent, it can quantify the relative fraction of impurities in the measured CNT sample using the area ratio of D/G bands under fixed laser power density. In addition, the diameters and electronic structures of CNTs can be determined by using the resonance Raman scattering [43]. However, the drawback of Raman spectroscopy is that it cannot provide direct information on the nature of metal impurities.

- UV–Vis-NIR spectroscopy is a rapid and convenient technique to estimate the relative purity of bulk SWNTs. It is convenient to determine the concentration of SWNTs dispersed in solution once the extinction coefficient of SWNTs is known [44]. On the other hand, SWNTs give rise to a series of predictable electronic band transitions between van Hove singularities in the density states of nanotubes (S_{11}, S_{22}, and M_{11}), therefore this technique is also used to analyze SWNT types, i.e., metallic or semiconducting [45], according to their electronic structure. The drawback of this method is the difficulty in repeatedly preparing the standardized SWNT film or solution and controlling film thickness or solution concentration, making it difficult for quantification analysis. Furthermore, it is not yet possible to provide an absolute value of the purity of SWNTs because there is no 100% pure standard SWNT sample or accurate extinction coefficient for SWNTs.

2.8.2 Purification Methods

Purification methods of CNTs can be basically classified into two categories: chemical and physical.

- The chemical method purifies CNTs based on the idea of selective oxidation, wherein carbonaceous impurities are oxidized at a faster rate than CNTs, and the dissolution of metallic impurities by acids. This method can effectively remove amorphous carbon and metal particles except for those encaged in polyhedral graphitic particles. However, the chemical method always influences the structure of CNTs due to the oxidation involved. (This will be the only method discussed here)

- The physical method separates CNTs from impurities based on the differences in their physical size, aspect ratio, gravity, and magnetic properties, etc. In general, the physical method is used to remove graphitic sheets, carbon nanospheres (CNSs), aggregates or separate CNTs with different diameter/length ratios. In principle, this method does not require oxidation, and

therefore prevents CNTs from severe damage. However, the physical method is always complicated, time-consuming and less effective. Physical-based methods include filtration, chromatography, centrifugation, electrophoresis, and high temperature (1400–2800 °C) annealing.

Owing to the diversity of the as-prepared SWNT samples, such as nanotubes type, morphology and structure, as well as impurity type and morphology, it needs a skillful combination of different chemical and physical purification techniques to obtain SWNTs with desired purity.

2.8.3 Chemical Oxidation

The carbonaceous impurities co-existing with as-synthesized SWNTs are mainly amorphous carbon and CNPs. Compared with SWNTs, these impurities usually have higher oxidation activity. The high oxidative activity demonstrated by amorphous carbon is due to the presence of more dangling bonds and structural defects which tend to be easily oxidized; meanwhile the high reactivity of the CNPs can be attributed to their large curvature and pentagonal carbon rings [46]. Therefore, chemical oxidation purification is based on the idea of selective oxidation etching, wherein carbonaceous impurities are oxidized at a faster rate than CNTs. In general, chemical oxidation includes gas phase oxidation (using air, O_2, Cl_2, H_2O, etc.) and liquid phase oxidation (acid treatment and refluxing, etc.). The disadvantages of this method are that it often opens the end of CNTs, cuts CNTs, damages surface structure and introduces oxygenated functional groups (–OH, –C=O, and –COOH) on SWNTs. As a result, the purified CNTs in turn can serve as chemical reactors or a starting point for subsequent nanotube surface chemistry [47].

2.8.3.1 Gas phase oxidation

In gas phase oxidative purification, CNTs are purified by oxidizing carbonaceous impurities at a temperature ranging from 225 °C to 760 °C under an oxidizing atmosphere. The commonly used oxidants for gas phase oxidation include air [48–49], a mixture of Cl_2, H_2O, and HCl [50], a mixture of Ar, O_2, and H_2O [51], a mixture of O_2, SF_6 and $C_2H_2F_4$ [52], and steam [53].

Gas phase oxidation is a simple method for removing carbonaceous impurities and opening the caps of CNTs without vigorously introducing sidewall defects, although it cannot directly get rid of metal catalyst and large graphite particles. For purifying SWNTs, acid treatment to remove the metal catalyst is always necessary. Another point worth noting is that SWNTs in agglomerates prevent oxidant gas from homogeneously contacting the whole sample limiting the amount of starting material to be purified

2.8.3.2 Liquid phase oxidation

Liquid phase purification simultaneously removes both amorphous carbon and metal catalyst. Oxidative ions and acid ions dissolved in solution can evenly attack the network of raw samples, and therefore selection of oxidant type and precise control of treatment condition can produce high-purity CNTs in a high yield. The commonly used oxidants for liquid phase oxidation include HNO_3 [54,55], H_2O_2, a mixture of H_2O_2 and HCl [56], or a mixture of H_2SO_4, HNO_3 [57,58]. The shortcomings of this method are that it causes reaction products on the surface of CNTs, adds functional groups, and destroys CNT structures (including cutting and opening CNTs). Nitric acid is the most commonly used reagent for SWNTs purification for its mild oxidation ability, which can selectively remove amorphous carbon. In addition, it is inexpensive and nontoxic, capable of removing metal catalysts and no secondary impurities are introduced. Hydrogen peroxide (H_2O_2) is also a mild, inexpensive and green oxidant, which can attack the carbon surface. The disadvantage of H_2O_2 is that it cannot remove metal particles. Therefore, it is usually used together with HCl [59]. HNO_3, H_2O_2, can effectively remove metal particles, but they are not so effective in removing carbonaceous particles owing to the relative mildness in their oxidation. In order to get rid of carbonaceous impurities, liquid oxidants with stronger oxidation activity are required, such as H_2SO_4. A mixture of concentrated H_2SO_4/HNO_3 (3:1 by volume) to cut highly tangled long ropes of SWNTs into short, open-ended pipes, and thus produced many carboxylic acid groups at the open ends [57]. H_2SO_4/HNO_3 (3:1) is more effective than nitric acid in removing impurities. Furthermore, it was reported that the best purification condition could reach 98% purity of SWNTs with a yield of 40% within 2 h, without decreasing the number of small diameter nanotubes for a 3 h reflux process using a concentrated H_2SO_4/HNO_3 mixture (3:1) [58].

Liquid phase oxidation is a continuous process that can eliminate impurities and it often leads to surface modification that preferentially takes place on CNT sidewalls, which increases the chemical activity and the solubility of CNTs in most organic and aqueous solvents. This surface modification effect shows great potential for improving their physical and chemical properties for specific applications, e.g., in making mechanically reinforced composites, in use as scanning probe microscopy tips with tailored chemical sensitivity, and in producing nanotube derivatives with altered electronic structures and properties [60]. Furthermore, CNTs can be cut into short fragments decorated with oxygen functional groups under suitable treatment conditions, which greatly increases their dispersibility and facilitates their practical applications. For example, the application of CNTs in the field of emerging biotechnology is based on the premise that short CNTs are dispersible in water [61]. The main problem of this liquid oxidation strategy is the damage to CNTs, the inability to remove large graphite particles, and the loss of a large amount of SWNTs with small diameter. It is very difficult to obtain purified SWNTs with high-purity and high yield without damage by simply using liquid phase oxidation.

2.8.4 Carbonaceous Carboxylated Fragemnts

It is known that during the oxidation process of nanotubes, small polycyclic aromatic fragments can be generated from the fragmentation of nanotubes, originating from the oxidative attack to defect sites present in the raw material [62]. Due to their elevated reactivity, these fragments are functionalized during acid oxidation, mostly with the introduction of carboxylic groups. For these reason these fragments are referred to as carboxylated carbonaceous fragments (CCFs) (figure 2.31). Because of their aromatic structure, these CCFs tend to physisorb onto the sidewalls of the tubes through π-π interactions, screening the tubes in the interaction with the surrounding medium and hindering direct functionalization of the tubes.

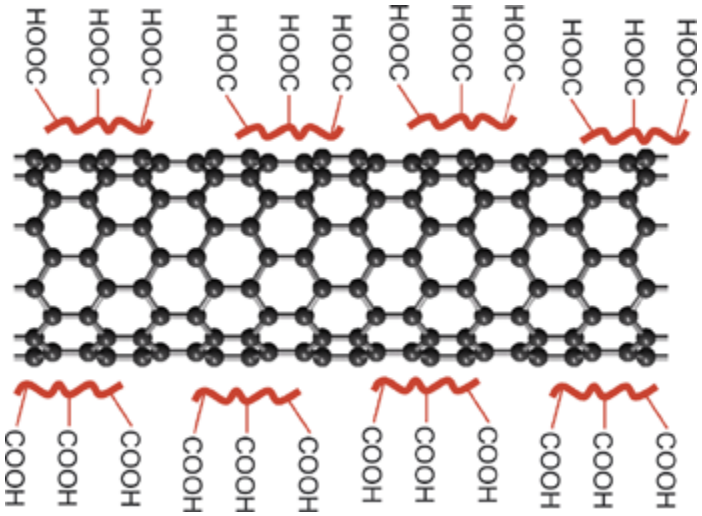

Figure 2.31 – Scheme of a SWNT with adsorbed carboxylated carbonaceous fragments.

It has been suggested that CCFs formed during acid oxidation are the principal site to be functionalized in following reactions, with nanotubes maintaining their structure unmodified [63]. In this view, CCFs tightly adsorbed onto nanotubes are the main responsible for the improved solubility of the tubes after the oxidation, considering that no functionalization actually occurs onto nanotubes surface. Removal of the CCFs is usually realized through a reflux step in strong alkaline conditions (NaOH 8M). It is thought that the ability of sodium hydroxide in removing CCFs is due to the deprotonation of the functional groups present on the CCFs, making them more soluble in the basic aqueous solution. But it was seen that the sodium hydroxide solution is also able to remove non functionalized fragments through the intercalation between the π-stacked structures, which reduce the π-π interactions between the CCFs and the nanotubes, similarly to graphite intercalation [64], facilitated by the heating at 100°C during the reflux. Therefore this base-washing step results effective in removing CCFs but also other carbonaceous impurities from acid-treated SWNTs samples.

2.9 Functionalization of Single Walled Carbon Nanotubes

Single-walled carbon nanotubes have mechanical, optical and electrical properties that make them ideal nanoscale materials [65]. However, all the proposed applications have so far been limited by their practical insolubility in aqueous and organic solvents [66]. Due to their high polarizability and smooth surface, SWCNTs form bundles and ropes, where several nanotubes are aligned parallel to each other with a high van der Waals attraction (0.5 eV/mm). In addition, CNTs are obtained as mixtures that exhibit different chiralities, diameters and length, in which non-NT carbon and metal catalysts are also present in the final material.

Some of these limitations can be overcome by the controlled defect and sidewall functionalization of CNTs [67,68]. The formation of covalent linkages can drastically enhance the solubility of CNTs in various solvents at the same time that guarantees the structural integrity of the nanotube skeleton, but it also alters the intrinsic physical properties of the CNTs because of a modification of the sp^2 carbon framework [69]. The most notable effect is that the inherent conductivity of the CNTs is basically destroyed. For these reason, covalent sidewall functionalization reactions will not be taken into account here.

An alternative strategy for preserving the intrinsic electronic and mechanical properties of CNTs consists in the noncovalent or supramolecular modification of CNTs [67]. Such interactions primarily involve hydrophobic, van der Waals, and electrostatic forces, and require the physical adsorption of suitable molecules onto the sidewalls of the CNTs. Noncovalent functionalization is achieved by polymer wrapping, adsorption of surfactants or small aromatic molecules, and interaction with porphyrins or biomolecules such as DNA and peptides.

2.9.1 Noncovalent Functionalization with Small Aromatic Molecules

The interactions between CNTs and a series of structurally related molecules: cyclohexane, cyclohexene, cyclohexadiene, and benzene, were investigated in the gas phase by Sumanasekera et al., and demonstrated that p–p interactions are fundamental for the adsorption on CNTs [70]. In particular, the highest adsorption energy was found for the molecule with the largest p-electronic system (benzene) and the lowest one for the molecule without p-electrons (cyclohexane). This result clearly indicates that the CNT–molecule interactions in this series are controlled by coupling of the p-electrons of the molecules with the electronic p-system of the CNT.

The adsorption of anthracene and several derivatives, substituted by groups with different electronic properties and volume size onto the sidewalls of cut SWCNTs (Figure 2.32) was investigated by considering the absorbance and fluorescence spectra of the aggregates formed.

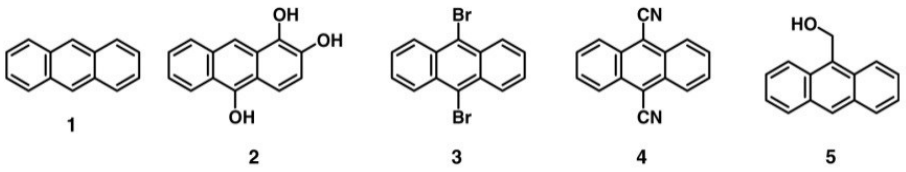

Figure 2.32 – Different anthracene derivatives used in the noncovalent functionalization of SWNTs.

The fluorescence spectra of anthracenes 1–5 on SWNTs are red-shifted, indicating a partial electron transfer from SWNTs onto anthracenes. In fact, the adsorption coverage varied with the aromatic ring substitution, since the π–π bond interactions governing the adsorption process are accompanied by an electron donor–acceptor charge transfer interaction between the aromatic adsorbates and the SWCNT sidewall. The extent in which the strength of the charge transfer interaction controls the relative degree of adsorption coverage follows the order: 4 > 3 > 5,1 > 2 (figure 2.32) [71].

The pyrene group is an aromatic system that demonstrates a very high affinity for nanotubes surface. Derivatives of pyrene can be efficiently deposited onto CNTs in all kind of solvents with a high surface coverage. In fact, the interaction of the aromatic system of pyrene with CNTs is so effective that functionalized pyrenes have been used for anchoring all kind of systems to CNTs with diverse applications. The development of reliable and reproducible methodologies to integrate CNTs into functional structures such as donor–acceptor hybrids, able to transform sunlight into electrical or chemical energy, has emerged as an area of intensive research the use of pyrene derivatives has been particularly crucial in the construction of versatile nanosized electron donor–acceptor ensembles through directed π–π interactions, such as pyrene-C_{60} [72] (figure 2.33).

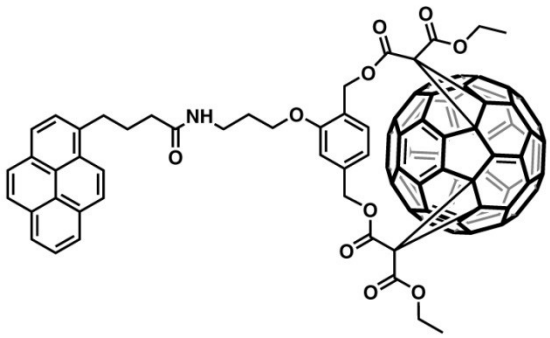

Figure 2.33 – Pyrene-bifunctional systems used for the immobilization of a C_{60} moieties onto CNT surfaces

The π–π stacking of small aromatic molecules could represent a very simple and efficient method to solubilize CNTs and introduce new opportunities for applications in chemistry, material sciences, or medicine.

2.9.2 Noncovalent Functionalization with Heterocyclic Polyaromatic Systems

Diverse heterocyclic polyaromatic molecules such as porphyrins and phthalocyanines can form effective interactions with CNTs. It is believed that the nature of the interaction is essentially the same van der Waals forces as in the case of the polyaromatic compounds. However, in some cases, the incorporation of a metal ion in the systems seems to weaken their interactions with the CNT sidewalls [73].

2.9.3 Noncovalent Functionalization with Surfactants

A significant progress toward the solubilization of CNTs in water has been achieved by using surfactants. In particular, the anionic surfactant sodium dodecyl sulfate (SDS) has been the most widely used [74–75] surfactant. TEM unambiguously demonstrated that SDS is adsorbed on the surface of CNTs and arranged into rolled-up half-cylinders with the alkyl group of each molecule pointed toward the nanotube. Depending on the symmetry and the diameter of the CNTs, ring, helices, or double helices were observed [76].

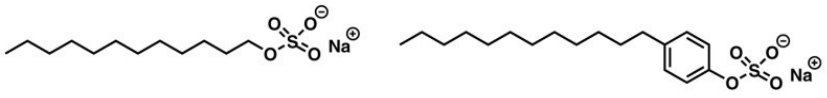

Figure 2.34 – (right) sodium dodecyl sulfate (SDS), (left) sodium dodecylbenzene sulfonate (SDBS).

Surfactant molecules containing aromatic groups are capable of forming more specific and more directional p–p stacking interactions with the graphitic surface of CNTs. Interactions of SDS and the structurally related sodium dodecylbenzene sulfonate (SDBS) with SWCNTs have been compared to demonstrate the role of the aromatic rings [77]. SDS and SDBS have the same length of the alkyl chain but the latter has a phenyl ring attached between the alkyl chain and the hydrophilic group (figure 2.34). The presence of the phenyl ring makes SDBS more effective for solubilization of CNTs than SDS, due to the aromatic stacking formed between the SWCNTs and the phenyl rings of the SDBS within the micelle. The diameter distribution of CNTs in the dispersion of SDBS, measured by atomic force microscopy (AFM), showed that even at 20 mg/ml ~63±5% of the SWCNT bundles exfoliate in single tubes [77].

2.9.4 Noncovalent Functionalization with Polymers

Creation of polymer/NTs composites is considered to be a useful approach for incorporating NTs into polymer-based devices. For noncovalently modified CNTs with polymers, several strategies have been developed. Currently, these strategies involve physical mixing in solution, in situ polymerization of monomers in the presence of CNTs, surfactant-assisted processing of composites, and chemical functionalization of the incorporated tubes. An interesting class of polymer composites that has

attracted much attention is that of the conjugated polymers. Since they are the main topic of this thesis, they will be separately discussed, in chapter 4.

Biological molecules have a wide variety of intricate structures tailored for controlled self-assembly that have somehow been adapted for the nanoscale self-assembly of nonbiological systems such as CNTs [78]. One structural motif used by proteins to promote self-assembly is the amphiphilic α-helix in which the polypeptide backbone forms a folded spring-like conformation stabilized by hydrogen, with the amino acid side chain extending outward from the exterior surface of the helix. These amphiphilic helical peptides were found to fold around the graphitic surface of CNTs and to disperse them in aqueous solutions by noncovalent interactions. Most importantly, the size and morphology of the coated fibers can be controlled by peptide–peptide interactions, affording highly ordered structures [79].

Within biological polymers, DNA is especially effective in dispersing CNTs in water, with resulting CNT–DNA hybrid solutions being stable for months at room temperature [80–82]. The oligonucleotides are found to readily adsorb on the CNT surface, after which they undergo a slow structural rearrangement (figure 2.35). The hybrids exhibit a complex morphology with DNA strands assuming a number of distinct backbone geometries, which depend on both DNA sequence and CNT diameter. In contrast, the nucleotide bases are found to align parallel to the CNT surface with a high degree of orientational order. While the binding appears to be primarily driven by energetically favorable π-stacking of DNA bases onto the CNT surface, equilibrium distribution of hybrid conformations is modulated by a complex interplay of forces, including the DNA conformation strain and solvent interactions.

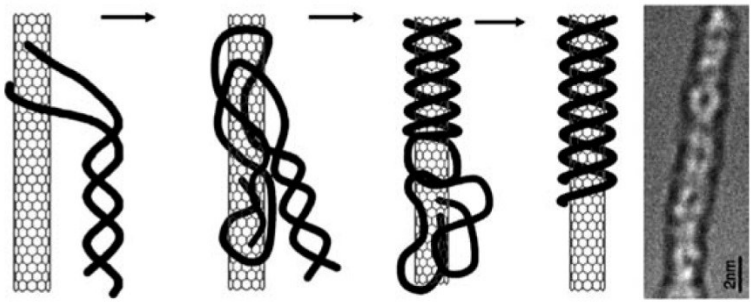

Figure 2.35 – DNA wrapping of CNTs. On the right side, a TEM image.

2.10 Dispersion of Single Walled Carbon Nanotubes

Pristine carbon nanotubes are characterized by a practical insolubility in aqueous and organic solvents [66] because of their high polarizability which drive their aggregation in bundles and ropes, held together by high van der Waals attraction forces (0.5 eV/mm).

Dispersion of carbon nanotubes could be viewed as being comprised of two different components. The first component is a kinetic process and consists of reducing the average bundle size, that is, debundling, and eliminating large yarn-like particulate aggregates. Simply placing nanotubes into a solvent either with or without a dispersing agent will not yield nanotubes dispersion without significant energy input (e.g. ultrasonication). In other words, this process is an activated process having a substantial energy barrier that must be overcome. During this stage, the energetics between the nanotube surface and the solvent are essentially irrelevant. The second part is the prevention of reaggregation of the dispersed nanotubes, which is where the energetics of the nanotube surface and the solvent are critically important.

2.10.1 Ultrasonication

Ultrasonication is probably the most common method to produce nanotubes dispersion. It works on the principle of generating alternating low- and high-pressure waves at a frequency corresponding to the frequency of sound waves. The low-pressure waves lead to the formation of bubbles that have an internal pressure less than atmospheric pressure, e.g. vacuum bubbles, while the high-pressure waves cause violent collapse of the bubbles. The collapse of the bubbles in turn generates the high forces associated with ultrasonic processing. The phenomenon of the generation and collapse of bubbles is termed cavitation. There are two typical devices used for sonication, sonicating baths and sonicating probes. The latter are also termed horn (or tip) sonicators. The latter generally produce much higher forces because the energy is localized to a very small area and hence ultrasonic probes are generally preferred for the separation of nanotubes. Because the tip diameter is typically of the order of 1 cm, forces are much localized. Sonication also creates an overall temperature rise that usually requires some sort of cooling.

2.10.2 Water dispersions of SWNTs

Water has many advantages as a dispersing liquid for carbon nanotubes. Water is inexpensive, nontoxic, nonflammable, and is easily removed via evaporation. These advantages mean that water is a very important dispersing liquid for many uses of carbon nanotubes. Water-soluble polymers also play a role in the importance of water dispersions of nanotubes, with particular importance for biological systems. Surfactants are the most common dispersing agents used to disperse nanotubes in water because surfactants have a propensity to accumulate at surfaces. Surfactants are water-soluble small molecules with a hydrophobic tail and a hydrophilic head group. Head groups can be ionic, typically

quaternary amines if cationic, sulfates or carboxylates if anionic, and typically ethylene oxide if nonionic. Hydrophobic chain can be a saturated hydrocarbons or a propylene oxide. Ionic surfactants have hydrophobic chain lengths typically between 8 and 18 carbon atoms because shorter chains do not have surfactant properties, while longer chains are not water soluble. Nonionic surfactants can have much longer hydrophobic lengths, because the hydrophilic part can also be much longer. Surfactants have the ability to disperse nanotubes in water because the hydrophobic tail is able to energetically interact with the nanotube favorably while the hydrophilic head is able to interact with the water. The ability of a surfactant to act as a good dispersing agent for nanotubes depends on the speed at which the surfactant diffuses into the interstitial sites when nanotubes are temporarily debundled due to high-shear forces and on the energetic interaction of the surfactant with the nanotube surface that includes surface–surfactant interactions as well as surfactant–surfactant interactions.

2.10.3 Organic solvents dispersions of SWNTs

The significant difference between some organic solvents and water is that it is possible to disperse nanotubes without functionalization or the use of a dispersant. A classical study published in 2000 tested a wide variety of solvents for their ability to disperse single-walled carbon nanotubes [83]. Some of the solvents that were found to disperse SWCNTs well include N-methyl pyrrolidone (NMP), cyclopentanone, α-caprolactone, and dimethyl formamide (DMF). In general, these solvents are good Lewis bases without hydrogen donors. A great deal of work has been carried out on NMP in particular because of its ability to do an excellent job at debundling [84].

It should be noted that generally the concentrations achievable with pure solvent dispersions tend to be much less than those that are possible with dispersant-assisted dispersions. The use of small molecules to assist dispersion in organic solvents is much less common than in water. Surfactants have many of the same properties in organic solvents as in water; of importance to nanotubes is that if the energetics are appropriate, surfactants can still adsorb to carbon nanotubes and play the same role as they do in water in enhancing dispersion of nanotubes in a low-viscosity liquid. The use of polymers to assist in the dispersion of nanotubes in organic solvents is quite widespread. Functionalization is a very common strategy to improve dispersion in organic solvents. As with water, the number of functional groups/small molecules/polymers that have been attached to nanotubes to promote dispersion in organic solvents is very wide.

2.10.4 SWNTs Sorting

Recently, the separation of SWNTs by exploiting subtle differences in the buoyant density of surfactant encapsulated CNTs in density gradient ultracentrifugation (DGU) has been reported [85–87]. As outlined by Green and Hersam [88], the buoyant density of a dispersed CNT is both a function of the geometry of the CNT (diameter) and the surfactant coating. On the one hand, a completely uniform surfactant coating results in separation by diameter [88], while on the other hand, the use of a surfactant

(or a combination of surfactants) that encapsulates CNTs in a manner dependent on the electronic structure, allows separation by electronic properties, as shown by cosurfactant DGU with 1 : 4 SDS/sodium cholate (SC) [88]. Therefore, the investigation of different surfactant systems and various cosurfactant experiments is crucial to exploit the tunability of the separation process by DGU.

2.11 Bibliography

[1] S. Iijima – *Nature*, **1991**, *354*, 56-58.

[2] S. Iijima, T. Ichihasi – Nature , **1993**, *363*, 603

[3] C.R. Martin – *Science*, 1994, *266*, 1961.

[4] R.F. Service – *Science*, **2001**, *294*, 2442.

[5] M. Turner, V.B. Golovko, O.P.H. Vaughan, P. Abdulkin, A.B. Murcia, M.S. Tikhov, B.F.G. Johnson, R.M. Lambert – *Nature*, **2008**, *454*, 981–983.

[6] Y.S. Zhang, K. Yu, D.S. Jiang, Z.Q. Zhu, H.R. Geng, L.Q. Luo – *Appl. Surf. Sci*, **2005**, *242*, 212.

[7] R.H. Baughman, C.X. Cui, A.A. Zakhidov, Z. Iqbal, J.N. Barisci, G.M. Spinks, G.G. Wallace, A. Mazzoldi, D.D. Rossi, A.G. Rinzler, O. Jaschinski, S. Roth, M. Kertesz – *Science*,**1999** , *284*, 1340.

[8] A. Bachtold, P. Hadley, T. Nakanishi, C. Dekker – *Science*, **2001**, *294*, 1317.

[9] H.W.Ch. Postma, T. Teepen, Z. Yao, M. Grifoni, C. Dekker – *Science*, **2001**, *293*, 76.

[10] A. Javey, J. Guo, Q. Wang, M. Lundstrom and H.J. Dai – *Nature*, **2003**, *424*, 654.

[11] E.T. Thostenson, Z.F. Ren, T.W. Chou – *Comp. Sci. Technol.*, **2001**, *61*, 1899.

[12] S. Berber, Y.K. Kwon, D. Tomanek – *Phys. Rev. Lett.*, **2000**, *84*, 4613.

[13] S.Y. Moon, W. Song, N. Kim, J.S. Lee, P.S. Na, S.G. Lee, J.W. Park, M.H. Jung, H.W. Lee, K. Kang, C.J. Lee, J. Kim – *Nanotechnology*,**2007**, *18*, 234201.

[14] S. Reich, C. Thomsen, J. Maultzsch – *Carbon Nanotubes: Basic Concepts and Physical Properties* (Wiley-VCH, Berlin 2004)

[15] M. S. Dresselhaus, G. Dresselhaus, P. C. Eklund – *Science of Fullerenes and Carbon Nanotubes* (Academic, San Diego 1995)

[16] M. S. Dresselhaus, G. Dresselhaus, P. Avouris (Eds.): *Carbon Nanotubes: Synthesis, Structure, Properties, and Applications*, vol. 80, Topics in Applied Physics (Springer, Berlin, Heidelberg 2001)

[17] R. Saito, G. Dresselhaus, M. S. Dresselhaus: *Physical Properties of Carbon Nanotubes* (Imperial College Press, London 1998)

[18] J. Kurti, V. Zolyomi, M. Kertesz, G. Sun – *New J. Phys.*, **2003**, *5*, 125.

[19] P. R. Wallace – *Physical Review*, **1947**, *71*, 622–634.

[20] R. Saito, M. Fujita, G. Dresselhaus, and M. S. Dresselhaus – *Applied Physics Letters*, **1992**, *60*, 2204–2206.

[21] J.W. Mintmire and C.T. White – *Phys. Rev. Lett.*, **1998**, *81*, 2506–2509 (1998).

[22] A. Ugawa, A. Rinzler and D.B. Tanner – *Phys. Rev. B*, **1999**, *60*, R11305–R11308.

[23] M.E. Itkis, S. Niyogi, M.E. Meng, M.A. Harmon, H. Hu and R.C. Haddon – *Nano Lett.*, **2002**, *2*, 155–159.

[24] C.L. Kane and E.J. Mele – *Phys. Rev. Lett.*, **1997**, *78*, 1932–1935.

[25] T. Pichler, M. Knupfer, M.S. Golden, J. Fink, A. Rinzler and R.E. Smalley – *Phys. Rev. Lett.*, **1998**, *80*, 4729–4732.

[26] Y. Murakami, E. Einarsson, T. Edamura and S. Maruyama – *Phys. Rev. Lett.*, **2005**, *94*, 087402/1–087402/4.

[27] S. M. Bachilo, M. S. Strano, C. Kittrell, R. H. Hauge, R. E. Smalley, R. B. Weisman – *Science*, ***2002, 298***, 2361.

[28] M. Kasha – *Disc. Faraday Soc.*, **1950**, 9, 14–19.

[29] Y.-Z. Ma, J. Stenger, J. Zimmerman, S.M. Bachilo, R.E. Smalley, R.B. Weisman and G.R. Fleming – *J. Chem. Phys.*, **2004**, *120*, 3368–3372.

[30] G.N. Ostojic, S. Zaric, J. Kono, M.S. Strano, V.C. Moore, R.H. Hauge and R.E. Smalley – *Phys. Rev. Lett.*, **2004**, *92*, 117402/1–117402/4.

[31] S. Reich, M. Dworzak, A. Hoffmann, C. Thomsen and M.S. Strano – *Phys. Rev. B*, **2005**, *71*, 033402/1–033402/4.

[32] M.S. Strano, C.B. Huffman, V.C. Moore, M.J. O'Connell, E.H. Haroz, J. Hubbard, M. Miller, K. Kittrell, C. Kittrell, S. Ramesh, R.H. Hauge and R.E. Smalley – *J. Phys. Chem. B*, **2003**, *107*, 6979–6985.

[33] G. Dukovic, B.E. White, Z.Y. Zhou, F. Wang, S. Jockusch, M.L. Steigerwald, T.F. Heinz, R.A. Turro, N.J. Turro and L.E. Brus, – *J. Am. Chem. Soc.*, **2004**, *126*, 15269–15276.

[34] R.B. Weisman, S.M. Bachilo and D. Tsyboulski – *Appl. Phys. A*, **2004**, *78*, 1111–1116.

[35] J. Maultzsch, S. Reich, C. Thomsen, H. Requardt, P. Ordejon – *Phys. Rev. Lett.*, **2004**, *92,* 075501.

[36] A. Jorio, R. Saito, J.H. Hafner, C.M. Lieber, M. Hunter, T. McClure, G. Dresselhaus, M.S. Dresselhaus – *Phys. Rev. Lett.*, **2001**, *86*, 1118–1121.

[37] M. Milnera, J. Kürti, M. Hulman, H. Kuzmany – *Phys. Rev. Lett.*, **2000**, *84*, 1324–1327.

[38] A.G. Souza Filho, S.G. Chou, Ge.G. Samsonidze, G. Dresselhaus, M.S. Dresselhaus, Lei An, J. Liu, Anna K. Swan, M.S. Ünlü, B.B. Goldberg, A. Jorio, A. Grüneis, R. Saito – *Phys. Rev. B*, **2004**, *69*, 115428.

[39] A. Jorio, A.G. Souza Filho, G. Dresselhaus, M.S. Dresselhaus, A.K. Swan, M.S. Ünlü, B. Goldberg, M.A. Pimenta, J.H. Hafner, C.M. Lieber, R. Saito – *Phys. Rev. B*, **2002**, *65*, 155412.

[40] R. Graupner – *J. Raman Spectrosc.*, **2007**; *38*, 673–683.

[41] V. M. Irurzun, M. Pilar Ruiz, D. E. Resasco – Carbon, **2010**, *48*, 2873 – 2881.

[42] F. Hof, S. Bosch, J. M. Englert, F. Hauke, and A. Hirsch – *Angew. Chem. Int. Ed.*, **2012**, *51*, 11727 –11730.

[43] M.S. Dresselhaus, G. Dresselhaus, A. Jorio, A.G Souza Filho, R. Saito – *Carbon*, **2002**, *40*, 2043–61.

[44] S.H. Jeong, K.K. Kim, S.J. Jeong, K.H. An, S.H. Lee, Y.H Lee – *Synthetic Met.*, **2007**, *157*, 570–4.

[45] T.J. Park, S. Banerjee, T. Hemaraj-Benny, S.S. Wong – *J. Mater. Chem.*, **2006**, *16*, 141–54.

[46] D.T. Colbert, J. Zhang, S.M. Mcclure, P. Nikolaev, Z. Chen, J.H. Hafner et al. – *Science*, **1994**, *266*, 1218–22.

[47] S. Banerjee, T. Hemraj-Benny, S.S. Wong – *Adv. Mater.*, **2005**, *17*, 17–29.

[48] P.M. Ajayan, T.W. Ebbesen, T. Ichihashi, S. Iijima, K. Tanigaki, H. Hiura – *Nature*, **1993**, *362*, 522–5.

[49] T.W. Ebbesen, P.M. Ajayan, H. Hiura, K. Tanigaki – *Nature*, **1994**, *367*, 519–9.

[50] J..L Zimmerman, R.K. Bradley, C.B. Huffman, R.H. Hauge, J.L. Margrave – *Chem. Mater.*, **2000**, *12*, 1361–6.

[51] R. Sen, S.M. Rickard, M.E. Itkis, R.C. Haddon – *Chem. Mater.*, **2003**, *15*, 4273–9.

[52] Y.Q. Xu, H.Q. Peng, R.H. Hauge, R.E. Smalley – *Nano Lett.*, **2005**, *5*, 163–8.

[53] G. Tobias, L.D. Shao, C.G. Salzmann, Y. Huh, M.L.H. Green – *J. Phys. Chem. B*, **2006**, *110*, 22318–22.

[54] E. Dujardin, T.W. Ebbesen, A. Krishnan, M.M.J. Treacy – *Adv. Mater.*, **1998**, *10*, 611–3.

[55] H. Hu, B. Zhao, M.E. Itkis, R.C. Haddon – *J. Phys. Chem. B,* **2003**, *107*, 13838–42.

[56] Y.H. Wang, H.W. Shan, R.H. Hauge, M. Pasquali, R.E. Smalley – *J. Phys. Chem. B*, **2007**, *111*, 1249–52.

[57] J. Liu, A.G. Rinzler, H.G. Dai, J.H. Hafner, R.K. Bradley, P.J. Boul, et al. – *Science*, **1998**, *280*, 1253–6.

[58] Y. Li, X.B. Zhang, J.H. Luo, W.Z. Huang, J.P. Cheng, Z.Q. Luo et al. – *Nanotechnology*, **2004**, *15*, 1645–9.

[59] X.L. Zhao, M. Ohkohchi, S. Inoue, T. Suzuki, T. Kadoya, Y. Ando – *Diam. Relat. Mater.*, **2006**, *15*, 1098–102.

[60] D. Tasis, N. Tagmatarchis, V. Georgakilas, M. Prato – *Chem. Eur. J.*, **2003**, *9*, 4001–8.

[61] D. Pantarotto, C.D. Partidos, R. Graff, J. Hoebeke, J.P. Briand, M. Prato et al. – *J. Am. Chem. Soc.*, **2003**, *125*, 6160–4.

[62] C.G. Salzmann, S. A. Lliwellyn, G. Tobias, M. A. H. Ward, Y. Huh and M. Green – *Adv. Mat.*, **2007**, *19*, 883-887.

[63] S. Fogden, R. Verdejo, B. Cottam, M. Shaffer – *Chem. Phys. Lett.*, **2008**, *460*, 162–167.

[64] K. Miyake, H. Shigekawa – Synth. Met., **1995**, *71*, 1753

[65] S. Reich, C. Thomsen and J. Maultzsch – *Carbon Nanotubes: Basic Concepts and Physical Properties*, **2004**, VCH, Weinheim, Germany.

[66] Special issue on carbon nanotubes – *Acc. Chem. Res.*, **2002**, *35*, 997.

[67] A. Hirsch – *Angew. Chem. Int. Ed.*, **2002**, *41*, 1853–1859.

[68] J.L. Barh and J.M. Tour – *J. Mater. Chem.*, **2002**, *12*, 1952–1958.

[69] V. Sgobba and D. M. Guldi – *Chem. Soc. Rev.*, **2009**, *38*, 165–184.

[70] G.U. Sumanasekera, B.K. Pradhan, H.E. Romero, K.W. Adu and P.C. Eklund – *Phys. Rev. Lett.*, **2002**, *89*, 166801.

[71] J. Zhang, J.-K. Lee, Y Wu and R.W. Murray – *Nano Lett.*, **2003**, *3*, 403–407.

[72] D.M. Guldi, G.M.A. Rahman, S. Qin, M. Tchoul, W.T. Ford, M. Marcaccio, D. Paolucci, F. Paolucci, S.Campidelli and M. Prato - *Chem. Eur. J.*,**2006**, *12*, 2152–2161.

[73] X.B. Wang, Y.Q. Liu, W.F. Qiu and D.B. Zhu – *J. Mater. Chem.*, **2002**, *12*, 1636–1639.

[74] M.J. O'Connell, S.M. Bachilo, C.B. Huffman, V.C. Moore, M.S. Strano, E.H. Haroz, K.L. Rialon, P.J. Boul, W.H. Noon,C. Kittrell, J. Ma, R.H. Hauge, R.B. Weisman and R.E. Smalley – *Science*, **2002**, *297*, 593–596.

[75] V.C: Moore, M.S. Strano, E.H. Haroz, R.H. Hauge and R.E. Smalley – *Nano Lett.*, **2003**, *3*, 1379–1382.

[76] C. Richard, F. Balavoine, P. Schultz, T.W. Ebbesen and C. Mioskowski – *Science*, **2003**, *300*, 775–778.

[77] M.F. Islam, E. Rojas, D.M. Bergey, A.T. Johnson and A.G. Yodh, – *Nano Lett.*, **2002**, *3*, 269–273.

[78] Tasis, D., Tagmatarchis, N., Bianco, A.,and Prato, M. (2006) Chem. Rev., 106,1105–1136.

[79] G.R. Dieckmann, A.B. Dalton, P.A. Johnson, J. Razal, J. Chen, G.M. Giordano, E. Muñoz, I.H. Musselman, R.H. Baughman and R.K. Draper – *J. Am. Chem. Soc.*, **2003**, *125*, 1770–1777.

[80] M. Zheng, A. Jagota, E.D. Semke, B.A. Diner, R.S. McLean, S.R. Lustig, R.E. Richardson and N.G. Tassi – *Nat. Mater.*, **2003**, *2*, 338–342.

[81] M. Zheng, A. Jagota, M.S. Strano, A.P. Santos, P. Barone, S.G. Chou, B.A. Diner, M.S. Dresselhaus, R.S. McLean, G.B. Onoa, G.G. Samsonidze, E.D. Semke, M. Usrey and D.J. Walls – *Science*, **2003**, *302*, 1545–1548.

[82] H. Cathcarth, V. Nicolosi, J.M. Hughes, W.J. Blau, J.M. Kelly, S.J. Quinn and J.N. Coleman – *J. Am. Chem. Soc.*, **2008**, *126*, 10640-10644.

[83] K.D. Ausman, R. Piner, O. Lourie, R.S. Ruoff, M. Korobov – *J. Phys. Chem. B*, **2000**, *104*, 8911–8915.

[84] S. Giordani, S.D. Bergin, V. Nicolosi, S. Lebedkin, M.M. Kappes, W. J. Blau, J.N. Coleman – *J. Phys. Chem. B*, **2006**, *110*, 15708–15718.

[85] M.S. Arnold, A.A. Green, J.F. Hulvat, S.I. Stupp and M.C. Hersam – *Nat. Nanotechnol.*, **2006**, *1*, 60–65.

[86] M.C. Hersam, – *Nat. Nanotechnol.*, **2008**, *3*, 387–394.

[87] C. Backes, F. Hauke, C.D. Schmidt and A. Hirsch – *Chem. Commun.*, **2009**, 2643–2645.

[88] A.A. Green and M.C. Hersam – *Mater. Today*, **2007**, *10*, 59–60.

3. Organic Semiconductors

3.1 Introduction

Organic materials, generally defined as those material that contain carbon, can be semiconductors. One of the first examples was the discovery of semiconducting properties of graphite in 1947 [1]. Research in organic electronics, pushed by the need for cheap electronic devices that cannot be fabricated by conventional inorganic semiconductors lead to the discovery that organic materials can be as conductive as metal [2], stimulating further advances in the fabrication of materials and devices, leading decades later, to commercial devices base on organic materials, e.g. organic light emitting diodes (OLEDs). Among different issues in organic semiconductor, the most important are probably the electronic processes which regulate the conduction of charge. Basically, from one "molecular" point of view, conduction can be seen as based on hopping from one molecular orbit to other. On the other hand, using a "solid-state" approach, organic semiconductors electronic states can be described with classical conduction and valence bands. Since electronics devices can only be made from semiconductor materials, devices fabricated with organic electronic materials are probably best described by classical semiconducting theory, with theoretical modification introduced when needed. A first significant difference that can be highlighted between inorganic and organic semiconductors concerns their band-gaps. In classical semiconductors, like silicon, germanium and GaAs, the band-gap between the conduction and the valence band is rather small, in the order of 1 eV. In most organic semiconductors, this band gap is much larger, in the order of 2 - 3 eV. Therefore, the optical processes have a larger range and, for instance, blue photovoltaic devices are possible. The application of organic materials is in the area of cheap electronics, large-area electronics [3], or electronic devices that cannot be fabricated by classical materials like flexible electronics [4]. With the ultimate goal of reaching the single-molecule electronics level, research is now focused on nanoscale technologies, such incorporating carbon nanotubes [5,6]. In contrast to inorganic materials, the number of organic materials is practically infinite, and organic materials can be synthesized and modified to meet any need for the specific application. In addition organic materials are highly compatible with biological material so they are the ideal candidates for bioelectronics. Another fundamental difference is the difficulty of making organic materials with the same level of purity and crystallinity as inorganic semiconductors. However, long range is not needed to give the material semiconducting properties [7], so noncrystalline, disordered materials can also be treated by semiconductor band theory in first approximation. Noncrystallinity and impurities cause also a large density of trap states which deeply affect the electronic behavior. Trap states are localized states that can capture charge carriers preventing them from contributing to conduction, i.e. their mobility is zero. There exists also models to include hopping or tunneling conduction via traps [8], but they are more related to insulating materials. Generally, when the (intrinsic) mobility is below 10^{-4} cm^2 V^{-1} s^{-1}, the conduction is most like to be of hopping type, while above this limit it is more likely to be of band type. Finally, there is a fundamental difference between organic and inorganic semiconductors, that is the mechanical and chemical

stability. In fact organic materials can show phase transition and conduction is not only based on electrons and holes, but in some material can be correlated to ionic transport, that is a much slower and less controlled process.

3.2 Conduction mechanisms in organic semiconductors

There is a debate between free carriers, meaning electrons in the conduction band and holes in the valence band, and polarons [9] or bipolarons [10], charged associated with a local lattice deformation and polarization. Another on-going debate is the distinction between hopping conduction and band conduction (figure 3.1). In the first case only localized states are involved in conduction because the delocalized bands are too far away or the temperature is too low for thermal excitation of trapped charges. These charges spend all of their time on these states and transport of charge occurs by hops between these states (figure 3.1a). This causes a field and temperature dependence of the effective mobility. In the second case, charges spend most of their time on localized deep states from where they cannot contribute to current, reducing the average mobility, but they can be excited in highly delocalized states and travel freely (Poole-Frenkel conduction) (figure 3.1b).

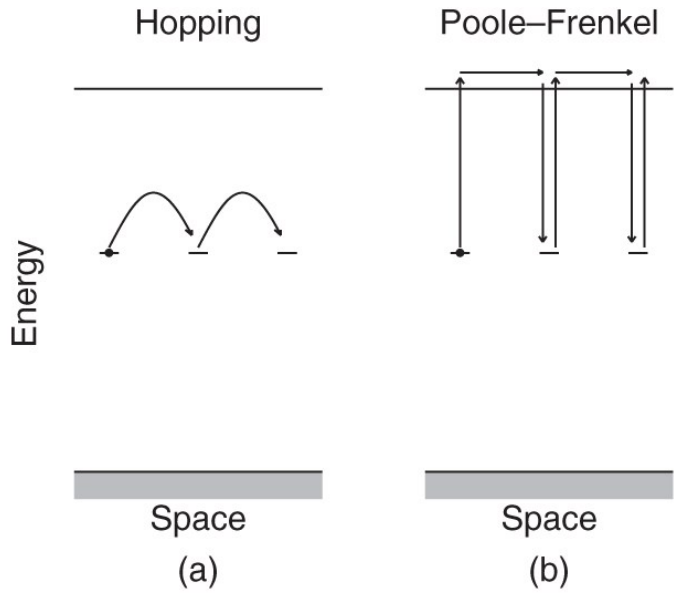

Figure 3.8 – Hopping conduction (a) and Poole–Frenkel conduction (b)

Poole-Frenkel conduction model is more adequate for devices showing substantial currents, when conduction is no longer a perturbation. In this view, all conduction processes occur through the conduction and valence bands; to contribute to current, a charge trapped on a deep level has to be promoted to a conductive band, i.e. no direct hopping from trap to trap is possible.

3.3 Mobility in organic semiconductors

Mobility is one of the most important parameter in electronic materials, because it determines the switching speed of the devices since charge have to drift or diffuse in and out of the active zone of the device, and these processes are both governed by mobility. Most research is therefore aimed to increase the mobility.

Mobility can be defined as the factor that links current to the product of density of charge (*qp*, where *p* is the hole density) and the electric field (*E*)

$$J = \mu_p \, q \, p \, E$$

where *J* is the current density.

Assuming that μ_p and p are constant, a more correct picture is one in which the charge density is temperature dependent.

$$J(T) = \mu_p \, q \, p(T) \, E$$

If a material has a remarkably low conductivity, this is often not because of low intrinsic mobility, but rather because unexpected low density of free carriers, for instance because most charge is located in traps and cannot contribute to current.

The mobility is defined as the proportionality between current and the product of field and total charge ρ.

$$J = \mu_{eff} \, \rho \, E$$

Where appears the effective mobility (μ_{eff}), in which the different contributions to current of free and trapped charges are distinguished.

$$\mu_{eff} = \frac{p\mu_p + p_T\mu_T}{p + p_T}$$

Where p is the density of free charges (holes) in the valence band and p_T is the density of trapped charges, μ_p is the intrinsic mobility of free holes in the valence band and μ_T is the mobility of trapped charges.

Since μ_T is equal to zero,

$$\mu_{eff} = \frac{p}{p + p_T}\mu_p$$

The efficient mobility is therefore given by the intrinsic mobility μp multiplied by the fraction of total charge that is in mobile states. Since this fraction can be strongly dependent on factors such as temperature or bias, so will be the effective mobility. In conclusion, saying that organic materials have low mobility is inaccurate, it is more correct to say that they are trap-ridden.

3.4 Conjugation in organic semiconductors

Conjugation is the base of the semiconducting properties of organic materials. Conjugation typically consists in the alternation of single and double bonds along a chain of carbon atoms (figure 3.2). This situation leads to two important results: the splitting of the energy levels with the opening of a band gap in the range of semiconductors, and the delocalization of charges in these levels.

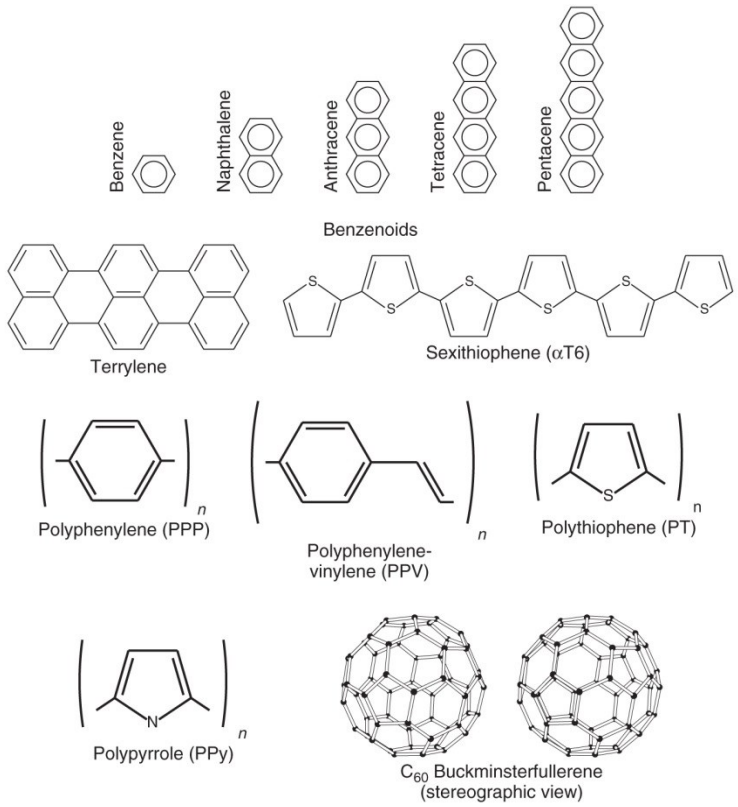

Figure 3.9 – Examples of organic semiconducting materials, such as oligomers, polymers and buckminsterfullerene (in which each atom is bound to three neighbors, i.e. has one double bond)

Of the four electrons on each carbon atom in the chain three can be considered to reside in sp^2 hybridized orbitals and the remaining electron in a p_z orbital. The three sp^2 electrons are used to form covalent bonds via σ molecular orbitals to neighboring carbon atoms in the chain on either side and to the sidegroup. The remaining electron in the p_z orbital is then used in a covalent bond via a π molecular orbital with a neighboring carbon atom in the chain on one side only. The result is a chain of alternating single (σ only) and double (σ and π) bonds.

Figure 3.3a shows the energy diagram of an interaction between two carbon atoms forming a double bond. After filling the levels from low to high it can be recognized that four electrons (two from each

carbon atom) are used in bonding, two in σ molecular orbitals, and two in π molecular orbitals. The remaining four electrons are in nonbonding (nb) orbitals and are still available for bonding to the rest of the chain and the ligands.

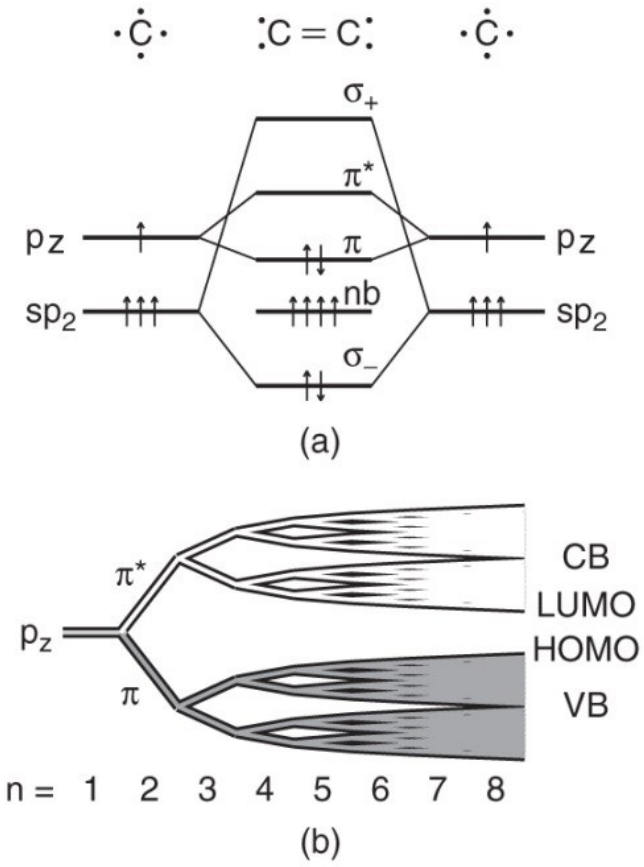

Figure 3.10 – (a) Energy diagram of two interacting carbon atoms. sp2 and pz atomic orbitals of the two individual carbon atoms combine to form π, σ and nonbonding molecular orbitals. (b) A band structure starts emerging with a narrowing band gap when the conjugation length of alternating single and double bonds is increased. A valence band with its HOMO and a conduction band with its LUMO are formed.

The key point is the splitting between the π and π ∗ molecular orbitals caused by the interaction between the p_z atomic orbitals. Interactions between p_z orbitals further away in the chain cause additional, smaller splitting of the levels (figure 3.3b) leading to a band structure. The formation of a chain of single and double bonds thus causes an energy structure with a HOMO and a LUMO level, with a splitting ('band gap') in the range of semiconductors. A material with only single σ bonds, like polyethylene, will have a much wider band gap and will not easily fall in to the category of semiconductors. To result in a semiconductor material, conjugation is essential. For polymeric organic electronic materials, the size of the chain of alternating single and double bonds is, in principle, infinite. For oligomeric organic materials, the chain is limited to the molecule. In both cases, the increasing chain length causes a narrowing of the band gap E_g. The term 'conjugation length' is used to designate

the length, or average length, of uninterrupted chain. For many molecules, the place of the double and single bonds is not uniquely determined, but has two distinct configurations with exactly the same energy. In these cases, resonance of the two forms causes a delocalization of the electrons (figure 3.4); it is no longer possible to identify the place of the single and double bonds; the electron wavefunction becomes one continuous cloud.

Figure 3.11 – Resonance between the two equal-energy configurations of single and double bonds

For other materials, for instance the linear chains with an odd number of atoms, the different forms have slightly different energies, but the difference is small enough to allow for this dislocation effect. In any case, this delocalization effect is essential for conduction. A charge injected into a π molecular orbit can relatively easily migrate along the chain.

For limited conjugation lengths, e.g. for oligomeric semiconducting materials, macroscopic conduction is then made possible by further overlap of molecular orbits with neighboring molecules, causing so-called Davydov splitting of the molecular levels (figure 3.5).

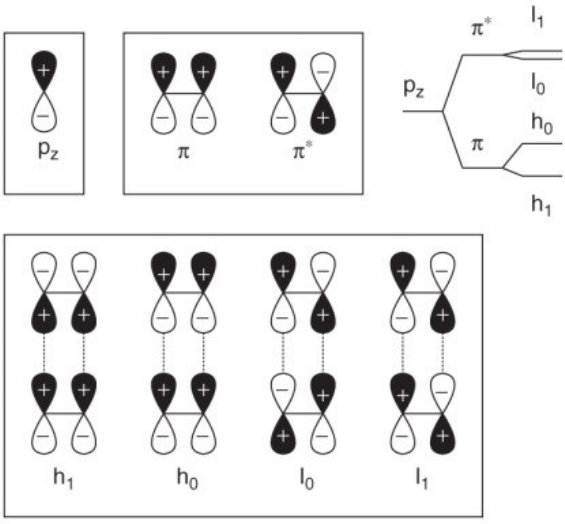

Figure 3.12 – Intramolecular interactions between p_z electrons causing molecular orbits π and π*. Intermolecular interactions cause a further spreading of the electronic levels.

Figure 3.5 summarizes the intramolecular interactions producing molecular orbitals and inter-molecular interactions further dispersing the energy levels, and delocalizing the electrons. The interactions cause the wavefunctions with maximum same-sign overlap to have lowest energy and those with proximity of

opposite-sign parts to have highest energy. Half of the electronic states are occupied and in this way a HOMO and LUMO can be identified. When the splitting between these two levels is relatively small, and a large delocalization of the electrons occurs, a semiconductor results. In this case it is more correct using valence and conduction bands instead than HOMO and LUMO. An electron is promoted from the top of the valence band (VB) to the bottom of the conduction band (CB). Both the electron in the CB and the missing electron, or 'hole', in the VB can contribute to current. In practice, most organic semiconductors conduct better via holes because of a higher efficiency of trapping (immobilizing) electrons. To summarize, the overlap of atomic and molecular wave functions causes a dislocation of electrons and the formation of valence and conduction bands. For insulating materials the overlap is minimal and the molecular orbitals (LUMO/HOMO) are good designations, whereas for the semiconducting materials, the overlap is strong and it is better to refer to conduction and valence bands. Roughly speaking, it can be said that materials for optical devices (light emitting diodes, LEDs, etc.) are more insulator-like, whereas materials for switching devices (FETs, etc.) are more semiconductor-like. Moreover, experience has shown that for LEDs, the polymers, for example PPV, are more suitable, whereas for FETs, the oligomeric materials, for example T6, are better [11]. This finds its basis on the requirement for transistors of high mobility and thus a need for regularly stacked units, more easily obtained with small molecules. Purity is not a big issue for these devices since it does not limit the mobility. However, for photovoltaics, purity is essential since impurities create nonradiative recombination centers.

3.5 Doping

Semiconductors energy bands involved in the electrical behavior are therefore the valence and the conduction bands, with the different in energy between them determining the energy gap of the material. At low temperatures, the valence band is completely full, whereas the conduction band is completely empty. Although the valence band has many electrons, none of them can contribute to current because for every electron with velocity +v there always exists an electron occupying a state with an exact opposite velocity −v, even when an electrical field is present. For low temperatures, the average velocity and thus conductivity of the material is therefore zero and this distinguishes semiconductors from metals. Conductivity in semiconductors can be achieved by promoting electrons from the valence band to the conduction band or by directly injecting electrons in the conduction band or removing them from the valence band. In either case, this allows for an imbalance of electrons with opposite speeds and conduction can occur. In this way, either electrons in the conduction band or holes in the valence band can contribute to current.

There are basically four ways of creating electrons in the conduction band or holes in the valence band (figure 3.6).

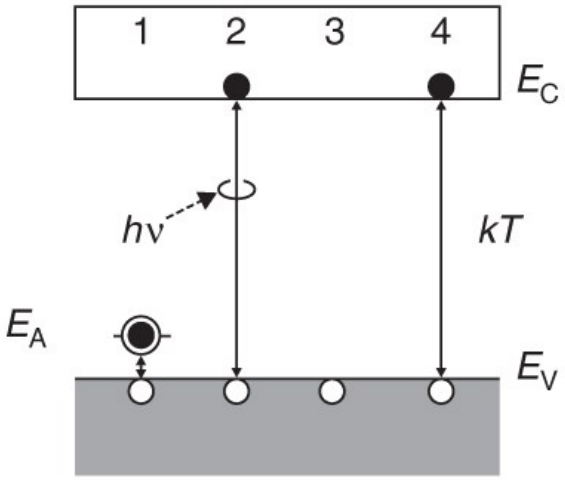

Figure 3.13 – Four ways of creating free charge carriers (holes ◦ or electrons •) contributing to external current: (1) chemically, e.g. by adding acceptors to the material that can capture electrons from the valence band, thus creating free holes ◦; (2) optically, using the energy of an absorbed photon for the creation of electron–hole pairs; (3) electrically, by changing the bias it can become energetically favorable to inject free holes; and (4) thermally, similar to optically, but the energy comes from the phonons of the crystal

1. Chemically: contaminating the material with chemically foreign dopants which either easily donate or accept electrons from the host material (called donors and acceptors, respectively). Doping in organic materials is not an important issue. This is because for the typical organic devices, LEDs and TFTs, purer materials work better. This is in contrast with some devices of classical semiconductors, such as pn-junction diodes and bipolar transistors, where doping is essential and device-dominating.

2. Optically: Electron–hole pairs can be created by the absorption of photons. This is the area of photovoltaics. The maximum absorption of light occurs for photon energies close to the band gap. This makes organic materials especially sensitive in the range of visible light. Likewise, recombination of electrons and holes causes the emission of photons and for organic materials blue LEDs are feasible because of their large band gap.

3. Electrically: Electrical bias can modify the energetic band diagram injecting free carriers in the bands. The FET may be used as an example. Even intrinsic materials can be induced into conduction by the presence of an electric field. Likewise, with enough voltage, even the most insulating materials can be made to conduct current. For LEDs, this is the preferred method of carrier generation. Doping of the materials can result in nonradiative recombination paths that can kill the luminescence.

4. Thermally: This way of creating free charges in the bands is very similar to the optical method. With high enough temperature, the lattice vibrations can thermally excite electrons from the valence band to the conduction band.

Of these effects, the optical and thermal ones create an equal amount of free electrons and holes. The chemical and electrical ways can create a mismatch of carriers. The chemical way creates uniquely one type of carrier, either electrons or holes. In principle this also applies to electrical creation of carriers. The electrical way can create both carriers only at opposing electrodes in, for instance, LEDs.

3.6 Devices

Organic semiconducting devices can be fabricated replacing classical inorganic semiconductors with organic semiconductors, conjugated polymers or conjugated molecules, taking advantage of their better and easier processability, their flexibility and their cheapness.

3.6.1 Ohmic contacts

In a semiconducting device, an ohmic contact is a junction between a metal and a semiconductor that allows current conduction following Ohm's law (i.e. shows a linear correlation between voltage and current) without blocking charge injection/extraction.

Work-function matching between metal and semiconductor is often used in organic semiconductor devices to form ohmic contacts (figure 3.7). The idea is to select a metal for the contacts that does not form Schottky barriers for the charges of interest. This implies that the Fermi level in the metal is aligned with the band of interest. Since the Fermi level is linked to the vacuum level in the metal by means of the work function ϕ_m (and the conduction band in the semiconductor by the electron affinity χ, and in turn the valence band is linked to the conduction band by the energy gap E_g), it means selecting a metal that has the appropriate work function.

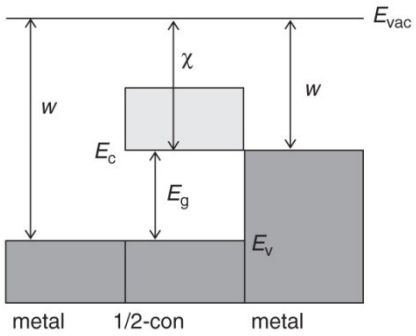

Figure 3.14 – Diagram showing how an appropriate choice of work function for the metallic contacts can avoid barriers. The left electrode metal has a high work function and this facilitates hole injection, whereas the right electrode has a low work function which is good for electron injection

Finding a good hole-injecting metal is often not a problem. The sum of electron affinity and band gap of the organic semiconductors lies in the range of work functions of most noble metals. Gold is a common choice for ohmic hole-injecting contacts. If transparent electrodes are needed, normally ITO (indium–tin oxide) is used. However, finding a good metal for electron injection is more difficult, since for that a low-workfunction metal is needed. These metals then suffer from the side effect of being highly reactive.

3.6.2 Schottky diode

Schottky diode is a two-terminal device consisting of a Schottky barrier and, in series, a purely resistive layer called the 'bulk'. The result is a rectifying element with current in one polarity ('forward') of the bias much larger than in the other polarity ('reverse'). Because of this asymmetry, the electrodes can be distinguished and are called 'anode' and 'cathode', where the anode is the one that has positive bias in forward polarity. A Schottky barrier is created from the intimate contact of a metal and a semiconductor (figure 3.8).

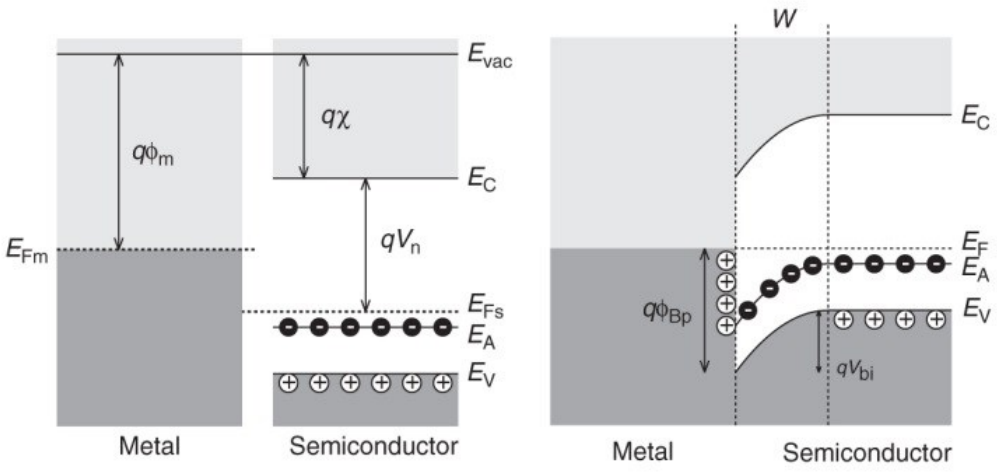

Figure 3.15 – Energy diagram of a metal – p semiconductor structure (Schottky diode) before (left) and after contact (right).

Because of a difference in Fermi level in the materials, E_{Fm} in the metal and E_{Fs} in the semiconductor, the system can gain energy by transferring charge. For a system with a p-type semiconductor, it implies electrons jumping from the metal into the semiconductor and consequently a build-up of negative charge in the semiconductor stored as immobile charge of ionized acceptors N^-_A. Alternatively it can be seen as free holes sucked out of the semiconductor.

The parameters that describe the barrier are:

- **Barrier height**, ϕ_{Bp}: This is the barrier as seen by the (majority) carriers, coming from the metal. This barrier is independent of bias. It is the difference between the top of the electron seas in the metal and the semiconductor before contact, $E_{Fm} - E_V$. Using the material parameters, this can be expressed as:

$$q\phi_{Bp} = (q\chi + E_g) - q\phi_m$$

where ϕ_m is the workfunction of the metal, χ is the electron affinity of the semiconductor and E_g is its electronic band gap.

- B**uilt-in voltage**, V_{bi}: This is the barrier as seen from the side of the semiconductor and is the band bending the holes have to overcome to reach the metal. It is the difference in Fermi levels before contact, thus

$$V_{bi} = \chi + V_n - \phi_m$$

where qV_n is the Fermi level depth relative to the conduction band.

- **Depletion width**, W: This is the extent of the zone in which the ionized acceptors are uncompensated by holes. This zone is therefore depleted of free carriers.

3.7 Optoelectronics and photovoltaics

The most prominent application of organic materials is in the area of optoelectronics and photovoltaics, meaning the conversion of electricity to and from light. They are commonly known as light emitting diodes (LEDs), that produce light, and solar cells that convert solar radiation into electric power.

3.7.1 Led

A LED is a device that converts electrical energy into light and this is the oldest semiconductor device. LEDs based on organic materials (OLEDs) were first studied in the 1990s [12], with as research aim the development of large-area displays [13].

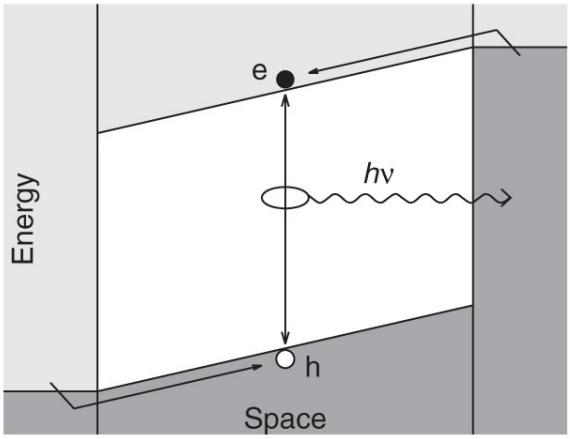

Figure 3.16 – Electrons and holes are injected into the conduction and valence band, respectively. Their recombination causes the emission of one photon

In an LED an electron and a hole can recombine and the liberated energy emitted in the form of a photon (figure 3.9). In this case the device does not need to be asymmetric. However, to control the injection of carriers into the device, and to create a well needed carrier balance, the work function of the electrode materials plays an essential role. Therefore, practical devices are often asymmetric, with one electrode adequate for hole injection into the valence band and the counter electrode having a work function adequate for electron injection into the conduction band. To optimize the light production, a balance between the two types of carriers is needed. Therefore, the choice of electrodes is essential.

There exist three possible reasons for a lower efficiency of LEDs (figure 3.10):

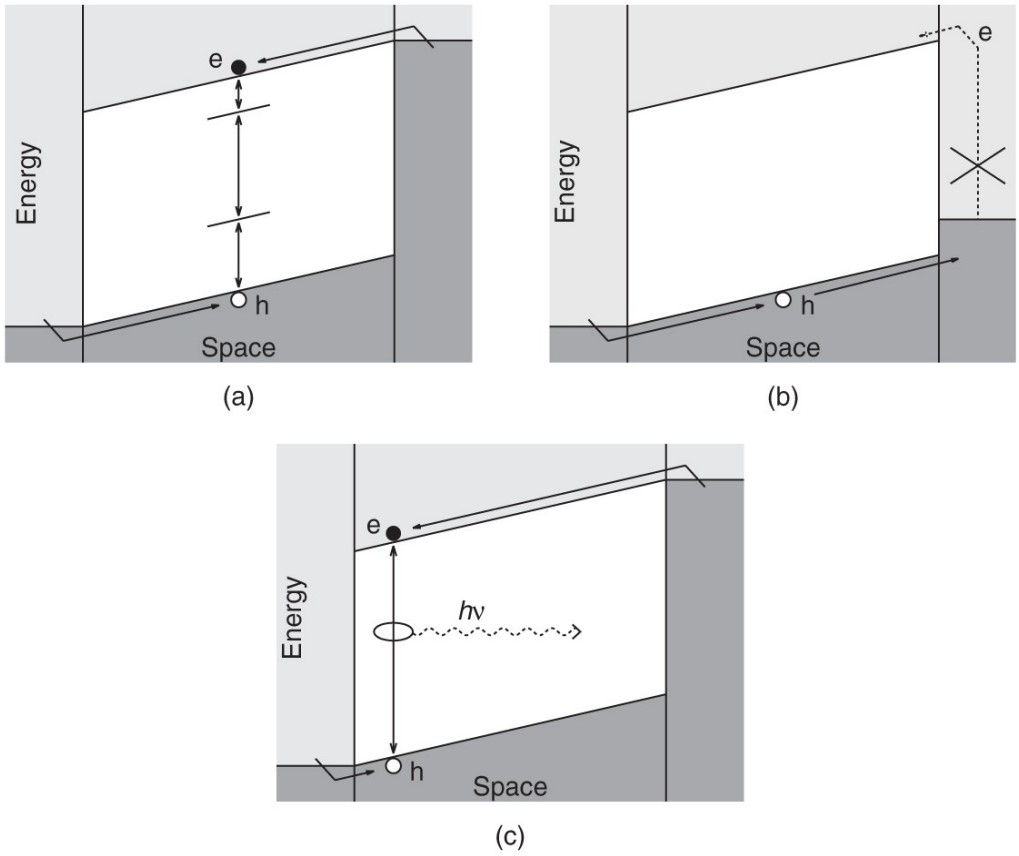

Figure 3.17 – (a) nonradiative recombination via defects; (b) mismatched carrier injection due to wrong choice of work function (resulting in current but no light); (c) mismatched carrier mobility (resulting in luminescence at electrode)

(a) When the material is not pure, nonradiative recombination centers such as impurities and lattice defects can reduce the quantum yield. It is obvious that making the material better (purer and more crystalline) will increase the yield.

(b) When the work function of the metal of one of the electrodes is not adequate for injection of that type of carrier, the result is that the current consists only of one type of carrier and no electron–hole recombination can take place. A large current without light emission results.

(c) When the mobility of one type of carrier is much larger than the mobility of the other type, the electron–hole recombination takes place close to an electrode. In these cases the luminescence is quenched.

The efficiency of a LED can be obtained by the external quantum efficiency, described as the number of emitted photons per electron-hole pairs injected.

$$EQE = \frac{photons\ s^{-1}}{I/q}$$

where *I/q* is the number of charged particles per second.

3.7.2 Solar Cell

A solar cell is an asymmetric device that converts solar radiation to electrical power. The energy of an incoming photon is absorbed by an electron which is thus promoted from the valence band to the conduction band, leaving behind a hole in the valence band. Because of the asymmetry of the device and the associated internal electrical fields, the electron–hole pair is dissociated and the electron and hole drift towards opposite electrodes. Here they are collected and contribute to an external current (figure 3.11).

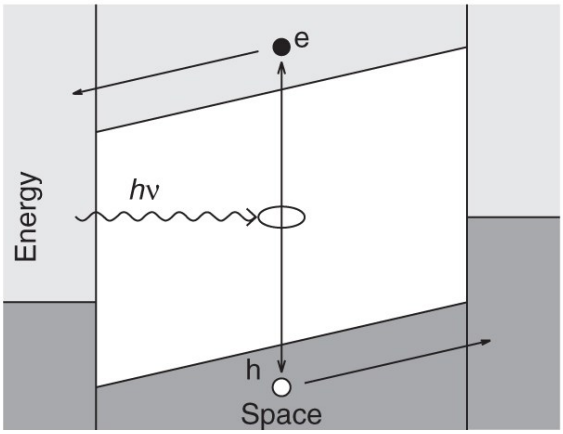

Figure 3.18 – An electron-hole pair, produced after absorption of a photon, is dissociated in free carriers by the internal electric field and those carriers migrate towards their respective electrode, giving a current.

The most important aspect of photovoltaic devices is the efficiency, given by the ratio of outgoing electrical power to the incoming solar radiation power. Commercial (silicon) solar cells can reach an efficiency of about 15%, where organic devices fall about one order of magnitude below that. Organic solar cells are still interesting because they can have unique properties such as mechanical flexibility. Moreover, much more interesting than the quantum efficiency is the cost-per-watt. In this respect, silicon is notoriously expensive, even in the polycrystalline or amorphous state.

The efficiency of a solar cell can be determined on basis of the I–V curves (figure 3.12).

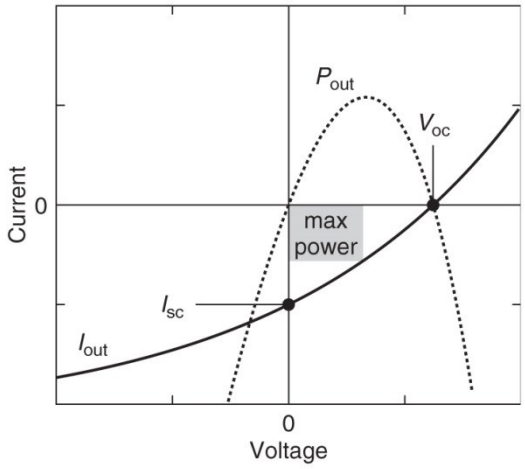

Figure 3.19 – I–V curve under illumination (solid curve) of a solar cell. The open-circuit voltage (Voc) and the short-circuit current (Isc) are indicated. The output power (P = −V × I) has a maximum that can be found by fitting a maximum-area rectangle under the curve. The filling factor is the ratio of the area of this rectangle to the total area under the curve with positive power.

The I–V curve of the device under illumination is represented by the solid trace (I_{out}). When the terminals are short-circuited a photovoltaic current can be measured (I_{sc}). An external bias of V_{oc} has to be applied to annihilate this current. This is also the voltage that results at the terminals when they are left in open-circuit. The maximum power output occurs for a voltage somewhere between 0 and V_{oc}, depending on the exact shape of the I–V curve. With power being the product of voltage and current, the maximum power can easily be found by fitting a rectangle with maximum area in the quadrant positive-V-negative-I.

The fill factor (*ff*) is a parameter used to quantify the quality of the device. It represents the ratio of the area of this maximum-power rectangle to the area of the $V_{oc} \times I_{sc}$ rectangle.

$$ff = \frac{V_{Max}\, I_{Max}}{V_{OC}\, I_{OC}}$$

Silicon-based devices have filling factors of about 40%. In principle, the filling factor is independent of the illuminated power, as long as the device output is linear with the illumination power. This because,

when the illumination is increased, the output current and power increase, but also the short-circuit current increases and the filling factor is invariant.

When using the fill factor (*ff*), the power conversion efficiency η can be calculated according to:

$$\eta = \frac{J_{SC}\, V_{OC}\, ff}{P_0} \times 100\%$$

where P_o is the optical power absorbed by the device.

Another way of measuring the quality of a photovoltaic device is the quantum efficiency. This is defined as the number of electron–hole pairs generated per incoming photon. The external quantum efficiency (EQE) is then defined by the external observables (current and photon flux), for instance by the electron–hole pairs that are effectively collected by the electrodes and result in an external current. For a solar cell:

$$EQE = \frac{I\ /\ q}{photons\ s^{-1}}$$

where I/q is the number of charged particles per second. The measurement of photon flux is straightforward for solar cells, since lasers are often used.

3.8 Bibliography

[1] P. R. Wallace – *Phys. Rev.*, **1974**, *71*, 622.

[2] A. J. Heeger – *Angew. Chem. Int. Ed.*, **2001**, *40*, 2591-2611

[3] C. D. Dimitrakopoulos, P. R. L. Malenfant – *Adv. Mater.*, **2002**, *14*, 99.

[4] G. H. Gelinck, H. E. A. Huitema, E. van Veenendaal, E. Cantatore, L. Schrijnemakers, J. B. P. H. van der Putten, T. C. T. Geuns, M. Beenhakkers, J. B. Giesbers, B.-H. Huisman, E. J. Meijer, E. Mena Benito, F. J. Touwslager, A. W. Marsman, B. J. E. van Rens, D. M. de Leeuw – *Nature Mater.*, **2004**, *3*, 106.

[5] K. Bradley, J.-C. P. Gabriel, G. Grüner – *Nano Lett.*, **2003**, *3*, 1353.

[6] P. Qi, A. Javey, M. Rolandi, Q. Wang, E. Yenilmez, H. Dai – *J. Am. Chem. Soc.*, **2004**, *126*, 11774.

[7] G. Caserta, B. Rispoli, A. Serra – *Phys. Status Solidi*, **1969**, *35*, 237.

[8] H. Bässler – *Phys. Status Solidi B*, **1993**, *175*, 15.

[9] T. Holstein, *Ann. Phys.*, **1959**, *8*, 325; T. Holstein – *Ann. Phys.*, **1959**, *8*, 343.

[10] S. Brazovskii, N. Kirova, Z. G. Yu, A. R. Bishop, A. Saxena – *Opt. Mater.*, **1998**, *9*, 502.

[11] L. Torsi, A. Dodabalapur, L. J. Rothberg, A. W. P. Fung, H. E. Katz – *Science*, **1996**, *272*, 1462.

[12] J. H. Burroughes, D. D. C. Bradley, A. R. Brown, R. N. Marks, K. Mackay, R. H. Friend, P. L. Burns, A. B. Holmes – *Nature*, **1990**, *347*, 539.

[13] R. H. Friend, R. W. Gymer, A. B. Holmes, J. H. Burroughes, R. N. Marks, C. Taliani, D. D. C. Bradley, D. A. Dos Santos, J. L. Bre´das, M. Lo¨ gdlund, W. R. Salaneck – *Nature*, **1999**, *397*, 121.

4. Carbon Nanotube – Conjugated Polymer Composites

4.1 Introduction

Conjugated semiconductor polymers can be used for a non-covalent surface modification of nanotubes that enhance the dispersion of small bundles and individual CNT in organic solvents [1–4]. The process is assisted by mild sonication that leads to momentary dispersion of the tubes in a solution. The co-dissolved polymers adsorb onto the CNTs and present a steric barrier that prevents re-aggregation of the CNT. While this approach is generic and applies to a variety of polymers, in the case of conjugated polymers it could be more interesting because products obtained from this non covalent approach between conjugated polymers and nanotubes are composite materials with different and peculiar properties resulting from their interaction at electronic level of the starting materials. Fabricating nanotubes composites using semiconducting polymers known for their optoelectronics and photovoltaics properties has allowed to produce hybrid system which can, for example, exhibit energy and charge transfer between conjugated polymers and nanotubes. Two of the most used semiconducting polymers are derivatives of poly(phenylenevinlene) (PPV) and poly(thiophene) (PT) such as poly[[(2-ethylhexyl)oxy]methoxy-1,4-phenylene]-1,2-ethenediyl], MEH-PPV and poly(3-hexylthiopehene) (P3HT) (figure 4.1). PPV and PT typically have very poor solubility. The introduction of a side chain increases the solubility of these macromolecules. For regioregular P3HT the functionalizing hexyl chain alternates regularly along the polymer backbone, which produces semicrystalline films when rrP3HT is cast onto a substrate: the side chains assist the self-assembly of the thiophene rings through π-π stacking into alternating layers containing the polymer backbone or the side chains. Within these layers the polymer backbone is in a stretched geometry with a conjugation length of up to 20-25 monomers [5]. This high degree of structure introduces high hole mobilities of up to 0.1 cm^2 $(V\ s)^{-1}$ observed in rrP3HT organic field effect transistors along the backbone and stacking direction [5] and is therefore beneficial for application in organic solar cells [6].

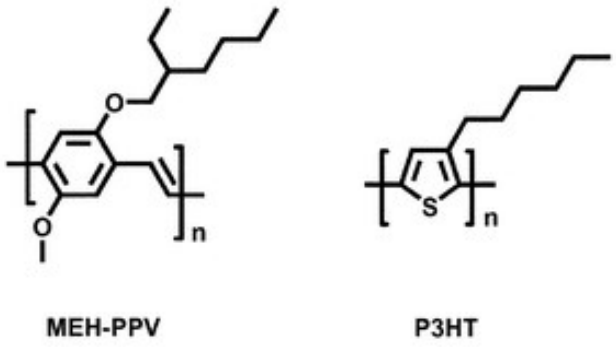

Figure 4.20 – Structures of poly[[(2-ethylhexyl)oxy]methoxy-1,4-phenylene]-1,2-ethenediyl], MEH-PPV and poly(3-hexylthiopehene), P3HT.

4.2 Interaction between CNT and conjugated polymers

Adsorption of conjugated polymers may result in either "wrapping" [3] or "stacking" [7] of the conjugated polymer onto the carbon nanotubes (figure 4.2). In the first model, the molecular geometry of the association of the conjugated polymer with the tube is helical (or double helical) wrapping of the tubes by the polymers. Wrapping of carbon nanotubes by a polymer may be driven by chemical interactions between the π-system of the CNT and the functional groups comprising the polymer or by electrostatic interactions in polar media [8]. It is now well accepted that polymer-wrapped carbon nanotubes are strongly associated, tightly bound systems (figure 4.2 a,b) where the tube surface chemistry, electronic structure and the intrinsic inter-tube interactions are modified by the wrapping [9]. In the second type of interaction, staking, part of the polymer chains adsorb via π–π interactions on top of the tubes, while additional chains stack upon the chains (figure 4.2c) [8]. Studies of the electronic structure of the formed hybrids suggest that they exhibit distinct electronic structure [9] as well as charge transfer at the ground state. Whether a conjugated polymer wraps or stacks onto a nanotube depends on the stiffness of the polymer and the chirality and diameter of the tubes. A semi-flexible polymer such as poly (m-phenylenevinylene-*co*-2,5-dioctyloxy-p-phenylenevinylene) (PmPV) was found to wrap around single walled nanotubes [9]. Functional conjugated polymers such as poly(p-phenyleneethynylene) (PPE) that are characterized by a rigid backbone were found to stack on the nanotube surface via π-stacking without wrapping [10,11]. Poly(3-alkilthiophene), P3ATs, represents an intermediate case, where the persistence length of a polymer is sensitive (among other properties of the polymer) to the length of the side chains and the regioregulairty. In good solvents for P3HT, a persistence length below 3 nm was measured [12] suggesting that P3HT acts as a semi-flexible polymer in dilute solutions [13]. Yet, planarization of the polymer backbone is observed in the solid state and in the aggregated state in poor solvents [14]. One may conclude that in the case of P3HT, the configuration should depend on the detailed structure of the nanotube and the processing conditions. The detailed adsorption mechanism of P3HT chains on the surface of nanotube was discussed by Boon [7]. In a study combining experiments and computer simulations, they showed that due to π–π interactions between thiophene units and the π–system of MWNT as well as CH–π interactions with the hexyl side chains, the polymer adopts a flat configuration on the MWNT. The initial adsorption of individual chains from solution was followed by gradual growth of P3HT fibrils by π-stacking of additional chains (figure 4.2c).

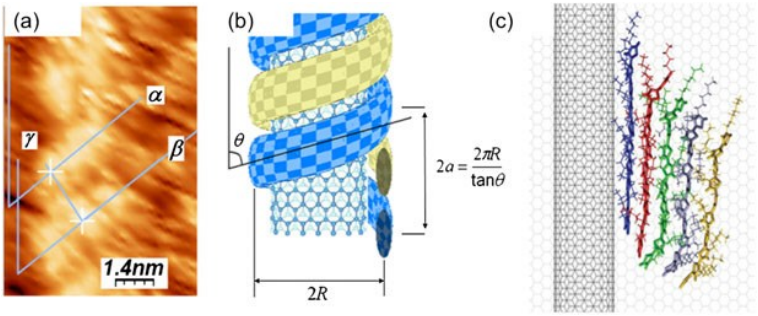

Figure 4.21 – Scanning tunneling microscopy image (a) and schematic representation (b) of a MWNT wrapped by P3HT self-organized into a coiled structure [3]. Molecular dynamics simulation of P3HT stacked on a SWNT [7].

In 2010, T. Schuettfort et al [15] used regioregular P3HT to fully isolate individual SWNT developing a route for the synthesis and extraction of a novel, highly ordered nanohybrid structure consisting of rrP3HT wrapped SWNTs (figure 4.3). They showed that the SWNTs serve as nanosubstrates for the rrP3HT, which self-organizes with a highly crystalline morphology on the nanotubes, so that increased charge carriers mobility is expected in the polymer. Additionally, rrP3HT nanocrystals of up to 10 nm height are attached to the rrP3HT coating of the nanotubes, indicating the ability of the nanohybrids to act as crystal seeds in a rrP3HT films.

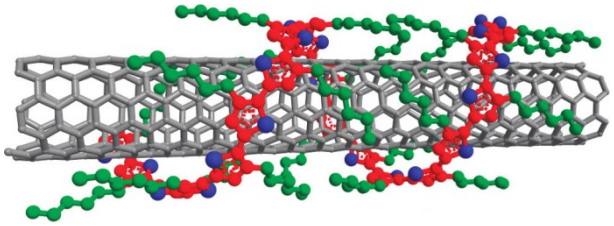

Figure 4.22 – Schematic drawing of a rrP3HT chain wrapping a (6, 5) SWNT at a 48° angle [16], forming a nanohybrid.

Another important potential advantage of noncovalent functionalization is the selectivity shown by specific conjugated polymers towards a specific (n,m) type of nanotubes. This allow to extract one family of nanotubes from the original ensemble and hence to obtain a material with specific electronic characteristics e.g. semiconducting (with a definite energy gap) or metallic. Nicholas and co-workers [17] have demonstrated that a polymer PFO exhibits high wrapping selectivity for specific diameters or chiral angles. Besides a high selectivity for large chiral angle SWNTs, enrichment of (7,5) species from the (6,5)-dominated SWNT ensemble (CoMoCAT) via PFO wrapping also corroborates the high selectivity on specific chirality of tubes. Similar results have also been achieved by Li and co-workers [18] when PFO is used to disperse the SWNT produced by chemical vapor deposition (CVD) based on CO disproportionation on Co-MCM-41 catalysts (Co-MCM SWNTs), where the PFO extracts a high purity (yield 79%) of the (7,5) species from the semiconducting SWNT ensemble (figure 4.4).

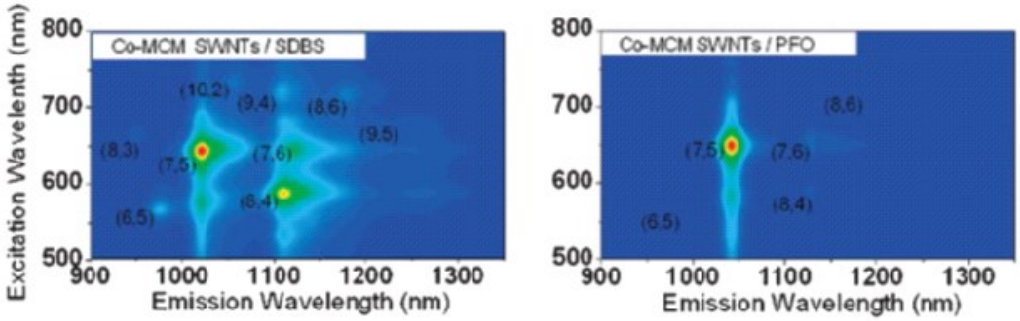

Figure 4.23 – Photoluminescence excitation (PLE) mappings for the SWNT ensemble dispersed in a typical sodium dodecylbenzene sulfonate (SDBS) surfactant (without tube selectivity) and that wrapped by PFO polymers

The high selectivity of PFO with a specific diameter is attributed to the formation of self-assembled intermolecular structures with an n-fold symmetry on SWNT surfaces. Not only limited to the PFO polymer, another fluorene-based polymer poly(9,9-dioctylfluorene-alt-benzothiadiazole) (F8BT) is also able to discriminately wrap SWNTs with larger diameters such as a (15,4) tube [19]. It has been suggested that a stable exciplex between poly[(9,9-dioctyl-fluorenyl-2,7-diyl)- co-(bithiophene)] (F8T2) and SWNTs exists, in which the energy level matching between SWNTs and fluorene-based polymers is responsible for the chirality selectivity. Structures of these conjugated polymers arereported in figure 4.5.

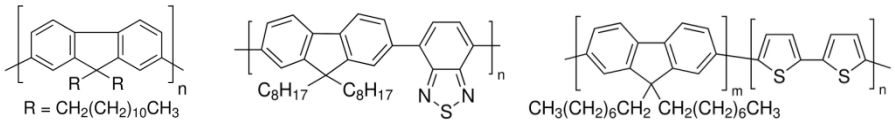

Figure 4.24 – PFO (left), F8BT (center), F8T2 (right)

4.3 Electrical properties of CNT - conjugated polymers composites

Since electrical conduction is a key aspect of nanotubes, their composites with electrically conducting polymers are critically important. In general, the classical percolation law used for composites of nanotubes and insulating polymer does not apply when nanotubes are mixed with a conducting polymer because a low-concentration region where conductivity increases slowly with nanotube amount does not exist. Instead, conductivity increases immediately with the addition of nanotubes, followed by a region where the conductivity increases less quickly [20]. Typical increases in conductivity depend primarily on the starting conductivity of the conducting polymer, and the higher the starting conductivity, the lesser the increase. In the region where the conductivity increases more slowly, the conductivity would be termed a "plateau" region in composites with insulating polymers, and the fact is that the conductivity increase in this region for composites of nanotubes and conducting polymers is approximately the same as that found for composites of nanotubes and insulating polymers.

The temperature dependence of the conductivity for an electrically conducting polymer generally follows a $\sigma = \sigma_0 e^{(-T_0/T)}$ dependence. With the addition of nanotubes in the plateau concentration region, the dependence with temperature is significantly less. The drop in conductivity from room temperature to ~ 10K is about one order of magnitude for an electrically conducting polymer containing nanotubes while that of the pure electrically conducting polymer is 20 orders of magnitude. In the lower nanotube concentration region where the conductivity increases more strongly with nanotube addition, the dependence is more complicated.

A Schottky diode is a device that has a metal attached to a semiconductor, and it conducts current in only one direction. Especially at low doping levels, conducting polymers can actually be classified as semiconductors, and hence laboratory devices as diodes are built with the conducting polymer acting as the semiconductor. The key characteristics are the reverse voltage that leads to device breakdown, the forward voltage required to cause conduction, and the relationship between voltage and current at high forward voltages. As expected, the addition of nanotubes to an electrically conducting polymer that is acting as one part of a Schottky diode causes an increase in conduction, although the nanotube level must be below a certain level so that the semiconductor does not become too conducting. At voltages greater than a value on the order of 1V, the conductivity is no longer ohmic but rather increases more rapidly than a linear relationship would predict and is consistent with Child's law of space charge limited emission. Such behavior is the result of electrical defects in the system, and possibly better fabrication procedures could improve the performance [21]. Not surprisingly, the forward voltage required to cause conduction decreases with an increase in carbon nanotube content [22].

4.4 Energy transfer in CNT - conjugated polymers composites

Photon absorption in semiconducting polymers forms bound-state electron–hole (called excitons.35) That can radiatively recombine and emit photons through band-to-band transition of the polymer, giving photoluminescence. The electron–hole pairs can also transfer from polymers to SWNTs, giving an energy transfer. Direct evidence of the PLE mapping proves that the photon-generated excitons in aromatic polymers are transferred from conjugated polymers to SWNTs, resulting in NIR photoemission from the semiconducting SWNTs [23]. A. Nish at al [21] succeeded in efficiently dispersing SWNTs in organic solvent using the semiconducting polymers MEH-PPV and poly(9,9-dioctylfluorenyl-2,7-diyl), (PFO). Through photoluminescence excitation mapping in the range of both the polymer's and the nanotube's optical absorbance, they showed that energy was transferred to the nanotubes when the polymer was photo-excited across its minimum band gap (figure 4.6).

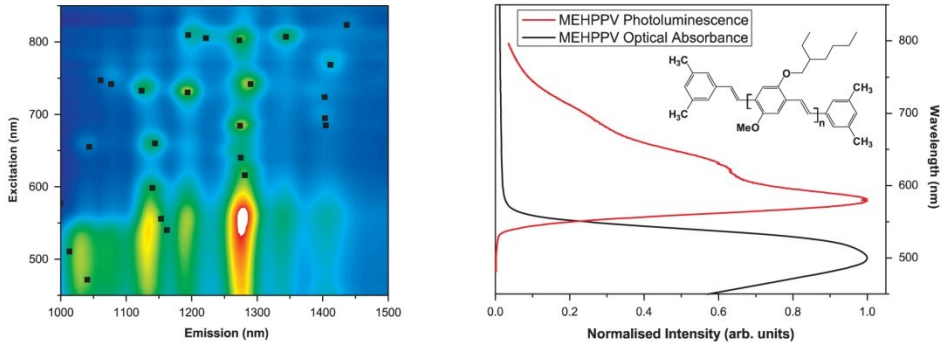

Figure 4.25 – Photoluminescence intensity from SWNTs (HiPCO) in solutions of MEH-PPV as a function of emission and excitation wavelengths. The black squares indicate the expected peak positions for all possible nanotube structures in this spectral range (left). Optical absorbance and emission from MEHPPV in toluene (right).

The enhanced band-gap emission of SWNTs in the NIR region is originated from the polymer wrapping layer which acts as a light-harvesting coating. Due to the strong interaction between the polymer and SWNTs, the absorbed photons can be utilized as the excitation light source for SWNTs band to band transition via energy transfer between SWNTs and polymer. The effect of polymer concentration on the energy transfer process from fluorene-based polymers to SWNTs has also been studied [25] where the polymer concentration governs the polymer aggregation on SWNTs which directly affects the energy transfer process.

4.5 Charge transfer in CNT - conjugated polymers composites

In addition to energy transfer from photosensitive polymers to SWNTs, the electron–hole pairs can also dissociate at the interface between SWNTs and polymers, which process is called charge transfer and is governed by the electronic energy alignment between SWNTs and polymers. The charge transfer process can be detected by the conductance change in SWNT-based electronic devices. The electrical responses to different wavelengths of light can be tuned by choosing different types of photosensitive polymers. Therefore, the photosensitivity of the semiconducting polymer greatly extends the photoelectrical responses of SWNTs. The charge transfer from photosensitive polymers to SWNTs is affected by many factors, such as Fermi energy alignment between polymer and SWNTs, the charge trapping, and the electrostatic gating. Furthermore, the one-dimensional geometry of individual SWNTs gives a low photon-capture cross-section which could limit the light harvesting. The large electron–hole recombination probability restricts the applications of SWNTs in photodetection. To solve this problem, SWNT networks have been used as the channel materials to increase the photon capture probability in the device. Self-assembled SWNT networks using an organic/inorganic phase separation method is one of the most practical way for SWNT network formation.

In 2009 T. Schuettfort [26] for the first time proved that hybrid rrP3HT–semiconducting SWNTs systems (figure 4.3) [15] exhibit a (theoretically predicted [27]) type II heterojunction at the interface which can promote the separation of the photo-generated charges, making this composite material a candidate for hybrid polymeric solar cells. They suggested that charge separation occur at the interface because the SWNT HOMO level E1 falls increasingly far below the rrP3HT HOMO level for decreasing diameters, forming a type II heterojunction between rrP3HT and small diameter SWNTs. Considering a (6,5) SWNT wrapped with a single monolayer of rrP3HT, after the creation of an exciton on the SWNT, the significant interaction will be between the hole in the nanotube valence band and the rrP3HT HOMO and is likely to lead to an extension of the hole wave function into the neighboring phase (figure 4.7).

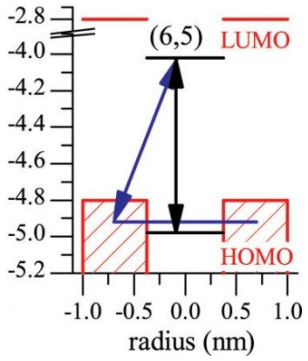

Figure 4.26 Energy levels of a (6,5) SWNT coated with one monolayer of rrP3HT (blue bar) compared to an isolated tube (black bar) showing a red shift upon hole delocalization.

By contrast, the electron in the SWNT conduction band is unaffected, as such conduction band does not overlap with allowed states in the polymer. This delocalization has a particularly strong effect on the Coulomb energy of the exciton, which scales with $E_C \propto 1/r$. Therefore, the delocalization of the nanotube valence band wave function caused by the type II band alignment result in a significant decrease in the strength of the Coulomb interaction, facilitating its dissociation.

This work was further extended by S. D. Stranks et al. [28] who showed that photoexcitation of the single P3HT layer wrapping the nanotube in nanohybrids led to an ultrafast electron transfer to the nanotube on a time scale of 400 fs. Since the remaining hole on the P3HT is confined to this single molecular layer, either a bound charge-transfer complex forms across the interface or non-radiative recombination takes places on the nanotube and no generation of free charge occur. However, the introduction of an excess of P3HT surrounding the molecular complexes allows transport of the hole away from the interface, leading to long-term charge separation (figure 4.8). Their results suggest that small diameter semiconducting SWNT-P3HT nanohybrids act as efficient charge generation interfaces for use in photovoltaic devices, provided that they are embedded in a matrix with a sufficient excess of P3HT.

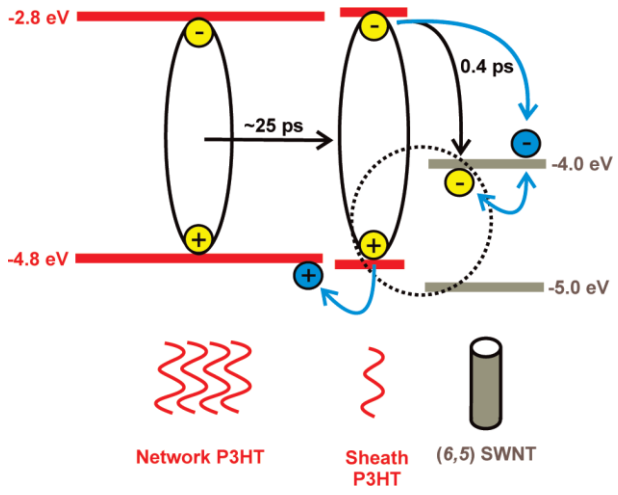

Figure 4.27 – Charge generation dynamics for a P3HT sheath monolayer around a (6,5) SWNT with an excess of P3HT acting as a surrounding network. A bound exciton is created on the network P3HT and migrates to a sheath-P3HT-NT interface within ~25 ps. At the interface the exciton dissociates and an electron is transferred to the nanotube while the hole remains on the P3HT. This produces free polarons (blue). In the presence of the network P3HT, the hole can migrate away from the interface (blue) and immediate charge separation is achieved. In the absence of network P3HT, the free polarons form a weakly bound exciplex or recombine nonradiatively as excitons within the nanotubes (both processes represented by dotted line).

The nanotube-polymer interfaces can provide comparable or better dissociation interfaces than all-polymer junctions. In addition, nanotubes offer greater electron mobility and longer percolation paths than conjugated polymers, suggesting that polymer-nanotube composites may be more effective active

media in OPVs than polymer-polymer or polymer-fullerene blends. Significantly, the presence of only 1% nanotubes is able to produce a similar efficiency of charge separation to that observed in an optimized 60:40 blend of P3HT-fullerene for which the fullerene electron acceptor does not contribute to light absorption. These findings thus establish a promising route for developing efficient OPV devices utilizing polymer-SWNT blends.

4.7 Solar Cells based on CNT - conjugated polymers composites

The essential difference between polymer-based organic and inorganic solar cells is the primary photoexcitation step: in organic materials, absorption of light does not lead to the formation of free charge carriers but to the formation of coulombically bound electron–hole pairs, the excitons, whose binding energy is of order of 100 meV (whereas it is about few meV for inorganic semiconductor).[28] The binding energy of excitons is a manifestation of weak (intermolecular) interactions among the molecules and the consequential low dielectric constant (typically 2–4) that characterizes organic materials.[29,30] Excitons may either recombine, and the absorbed photons will be wasted or they may diffuse in the active layer until they arrive at a dissociation site, a potential step formed at the interface between an electron donor and an electron acceptor in the active layer. As the diffusion length of excitons is in the range of 3 to 10 nm in polymers,[31] only dissociation sites located within this distance are relevant for splitting of the neutral excitons into charge carriers. Following exciton splitting, the free charge carriers further drift to the device's respective electrodes via two separate channels, holes via the electron donor phase to the anode and electrons via the electron acceptor phase to the cathode, generating the current (figure 4.9).

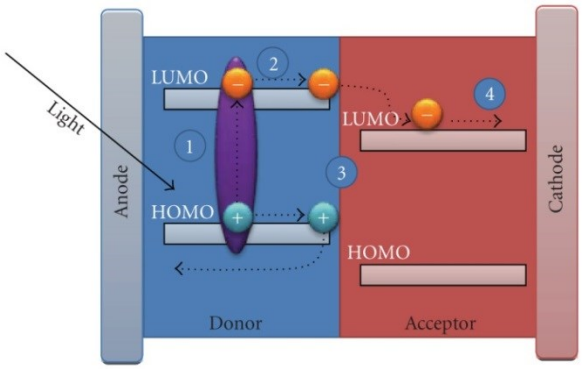

Figure 4.28 – Sequence of events in a polymer solar cell: 1) exciton formation upon light absorption, 2) exciton diffusion towards the donor-acceptor interface, 3) exciton splitting into free charges in separate phases, 4) charge migration toward respective electrodes.

The most common electron acceptors in polymer-based solar cell belong to fullerene family. Fullerenes are fully conjugated, all-carbon closed-cage molecules in the form of convex polyhedra containing only hexagonal and pentagonal faces. The most abundant and stable member of the family is C60, shaped as a soccer-ball truncated icosahedron.[32] LUMO of C60 is energetically low lying and triply degenerate, and capable of accepting at least six electrons upon reduction.[33] Experimental measurements have shown that that C60 is fully conjugated.[33–35] with high electron affinity and ionization potential and electrochemical. One of the most common chemically functionalized fullerenes is methanofullerene, [6,6]-phenyl C61 butiryc acid methyl ester, PCBM (figure 4.10). A short aliphatic chain (six carbons) with hydrophilic group at its end provides PCBM with improved solubility in organic solvents. PCBM is used as an electron acceptor in the active layers of molecular electronics and in particular in rr-P3HT-based POPV, allowing efficient exciton dissociation at the PCBM-polymer interface. The latter results from the good matching in the energy levels between P3HT and PCBM.

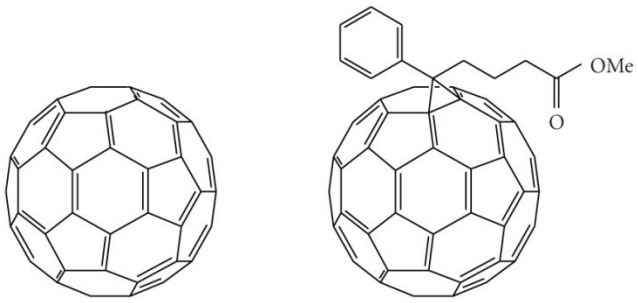

Figure 4.29 – Structures of fullerene C60 (left) and PCBM (right)

Carbon nanotubes were suggested as an efficient alternative to fullerenes and fullerene derivatives. In fact, in virtue of their high surface area [36] and high electron affinity [37] they can provide not only a tremendous opportunity for exciton dissociation, but also a percolation network to carry electrons to the electrode, while the holes are transported through polymer chains. At low doping levels, percolation pathways are established, providing the means for high carrier mobility and efficient charge transfer.

The idea of using SWNTs as acceptors in BHJ solar cells was proposed by Kymakis et al [36]. Enhancement of more than two orders of magnitude in the photocurrent, as compared to single component P3OT cells, was observed due to the addition of about 1 wt% SWCNT. While the authors speculated that the SWNT improved charge separation, the power conversation efficiency was 0.04% under 100 mW/cm2 illumination, well below that for typical BHJ POPV cells. The authors suggested that a poor dispersion of the SWNT and the presence of a mixture of metallic and semiconducting tubes were the reasons for the low efficiency. The same group demonstrated some years later [37] that the annealing of an active layer which contains P3HT/SWNT blend results in an increase in cell efficiency compared to un-annealed cells. Here, the improved efficiency may be related to improved hole

transport via the polymer matrix due to a higher degree of crystallinity induced by the presence of the SWCNT.

It is now evident that control over the structure and properties of the conjugated polymer-nanotubes blend, at length scales ranging from the molecular to the sub-micron range, is one of the most difficult as well as crucial issues for efficient photocurrent collection in CNT-based OPV devices.

In a recent study, Chang et al.[38] showed that the performance of CNT-P3HT POPV was correlated to the quality of the CNT dispersion in P3HT solutions and dominated by interaction of the CNT and the polymer with the solvent. This observation is not surprising, as it is well established that in fullerene–polymers solar cells, the morphology and performance of the device strongly depend on the interactions of both the conjugated polymer and the fullerenes with the solvent.

Arranz-Andres and Blau [39] studied the influence of the CNT dimensions (length and diameter) and their concentration in the POPV photoactive layer on the performance of a CNT-polymer device. They found that 5 wt% of CNT increased PCE by three orders of magnitude compared to that of the native polymer. The study reported that the introduction of CNTs into the P3HT matrix modified the energy levels of the P3HT (as evidenced by high V_{OC}) and the morphology of the active layer. They also found that the CNT acted as nucleation sites for P3HT chains, improved charge separation (as indicated by the large difference between light and dark conductivities) and served as networks for electron transport.

In 2010, Strano et coworker [40] fabricated a planar nano-heterojunction comprising well-isolated millimeter-long single-walled carbon nanotubes underneath a poly(3-hexylthiophene) (P3HT) layer (figure 4.11), evidencing its high-efficiency in the exciton dissociation at polymer/nanotubes interface. The resulting junctions display photovoltaic efficiencies per nanotube ranging from 3% to 3.82%, which exceed those of previously reported polymer/nanotube bulk-heterojunctions (BHJ) solar cells by a factor of 50–100.

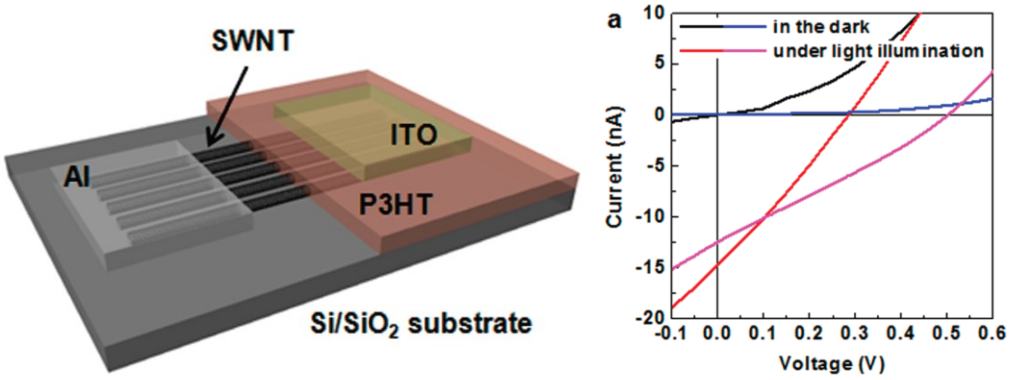

Figure 4.30 – Hybrid planar nanoheterojunction solar cell based on P3HT and SWNT (left). I–V curves of the device with p-type SWNTs (black and red) and n-type SWNTs (blue and pink) in the dark and under illumination from a solar simulator.

The increase is attributed to the absence of aggregate formation in this planar device geometry. It is shown that the polymer/nanotube interface itself is responsible for exciton dissociation. Typical open-circuit voltages are near 0.5 V with fill factors of 0.25–0.3, which are largely invariant with the number of nanotubes per device and P3HT thickness. A maximum efficiency is obtained for a 60 nm-thick P3HT layer. The most obvious reason for the increase in efficiency over BHJ devices based on the polymer/SWNT system is that the carbon nanotube interface is free from bundled aggregates compared to the interface of conventional polymer/carbon nanotube solar cells where fabrication proceeded from a colloidal dispersion of nanotubes. As the nanotubes were grown in parallel, there are no tube–tube junctions between metallic and semiconducting SWNTs. These junctions may be sources of exciton recombination sites in bundled aggregates. Having semiconducting SWNTs without the interruption of metallic SWNTs could give rise to a strong built-in electric field at the interface between semiconducting SWNTs and the P3HT layer where the separated charges are directly transported to the electrode through the nanotubes with little or no loss. Also the high quality of the SWNTs grown by CVD leads to higher efficiency. The implication is that high-efficiency photovoltaic devices involving SWNTs should use purified semiconducting nanotubes, preferably of low defect density and in an unbundled state (well-dispersed) to realize photovoltaic performances comparable or superior to that of BHJ solar cells. An additional advantage of their planar nanoheterojunction is that once charges dissociate, they reach their respective electrodes more easily and faster compared to free charge carriers generated in BHJ solar cells.

Another recent paper, by Arnold's group [41], report a study of the exciton dissociation and interfacial charge transfer from semiconducting single-walled carbon nanotubes (s-SWCNTs) to a variety of polymeric photovoltaic materials using a photoactive capacitor measurement technique. They succeeded in showing that photogenerated excitons on s-SWCNTs in thin films are dissociated at interfaces with P3OT and regioregular and regiorandom P3HT. Photocurrent bias dependencies reveal that poly(thiophene) derivatives serve as hole accepting materials to s-SWCNTs. In contrast, insufficient band offsets for dissociation and charge transfer result when s-SWCNTs are paired with wider gap materials such as MDMO-PPV, PVP, polycarbonate, and PFO. From these results, it is anticipated that photovoltaic devices with near-infrared photoresponsivity out to 1350 nm can be fabricated from pairings of P3HT/s-SWCNT, and these could represent a remarkable improvement since in conventional polymer-fullerene solar cells only the UV-Vis fraction of the solar spectrum is exploited, because of typical band gaps of such materials.

4.8 Bibliography

[1] B. Z. Tang, H. Xu – *Macromolecules*, **1999**, *32*, 2569–2576.

[2] A. B. Dalton, W. J. Blau, G. Chambers, J. N. Coleman, K. Henderson, S. Lefrant, B. McCarthy, C. Stephan, H. J. Byrne – *Synth. Met.*, **2001**, *121*, 1217–1218.

[3] M. Giulianini, E. R. Waclawik, J. M. Bell, M. De Crescenzi, P. Castrucci, M. Scarselli, N. Motta – *AIP*, **2009**, *95*, 013304.

[4] I. Szleifer, R. Yerushalmi-Rozen – *Polymer*, **2005**, *46*, 7803.

[5] Sirringhaus, H.; Brown, P. J.; Friend, R. H.; Nielsen, M. M.; Bechgaard, K.; Langeveld-Voss, B. M. W.; Spiering, A. J. H.; Janssen, R. A. J.; Meijer, E. W.; Herwig, P.; de Leeuw, D. M. – *Nature*, **1999**, *401*, 685–688.

[6] Thompson, B. C.; Frechet, J. M. – *Angew. Chem. Int. Ed.*, **2008**, *47*, 58–77.

[7] F. Boon, S. Desbief, L. Cutaia, O. Douhéret, A. Minoia, B. Ruelle, S. Clément, O. Coulembier, J. Cornil, P. Dubois, et al. – *Macromol. Rapid Comm.*, **2010**, *31*, 142–144.

[8] S. A. Ntim, O. Sae-Khow, F. A. Witzmann, S. Mitra – *J. Coll. Int. Sci.*, **2011**, *15*, 383-388.

[9] B. McCarthy, J. N. Coleman, R. Czerw, A. B. Dalton, M. in het Panhuis, A. Maiti, A. Drury, P. Bernier, J. B. Nagy, B. Lahr, H. J. Byrne, D. L. Carroll, W. J. Blau – *J. Phys. Chem. B*, **2002**, *106*, 2210–2015.

[10] J. Chen, H. Liu, W. A. Weimer, M. D. Halls, D. H. Waldeck, G. C. Walker – *J. Am. Chem. Soc.*, **2002**, *124*, 9034.

[11] J. Zhao, J. P. Lu, J. Han, C. K. Yang – *Appl. Phys. Lett.*, **2003**, *82*, 3746.

[12] G. W. Heffner, D. S. Pearson – *Macromolecules*, **1991**, *24*, 6295.

[13] T. Yamamoto, D. Komarudin, M. Arai, B. Lee, H. Suganuma, N. Asakawa, Y. Inoue, K. Kubota, S. Sasaki, T. Fukuda, et al. – *J. Am. Chem. Soc.*, **1998**, *120*, 2047.

[14] P. V. Shibaev, K. Schaumburg, T. Bjornholm, K. Norgaard – *Synth. Met.*, **1998**, *97*, 97–104.

[15] T. Schuettfort, H. J. Snaith, A. Nish and R. J. Nicholas – *Nanotechnology*, **2010**, *21*, 025201.

[16] R. G. S. Goh, N. Motta, J. M. Bell and E. R. Waclawik – *Appl. Phys. Lett.*, **2006**, *88*, 053101.

[17] A. Nish, J.-Y. Hwang, J. Doig, R. J. Nicholas – *Nature Nanotechnology*, **2007**, *2*, 640–646.

[18] F. Chen, B. Wang, Y. Chen and L.-J. Li – *Nano Letters*, **2007**, *7*, 3013–3017.

[19] M. Tange, T. Okazaki and S. Iijima, – *J. Am. Chem. Soc.*, **2011**, *133*, 11908–11911.

[20] T. Umeyama, N. Kadota, N. Tezuka, Y. Matano, H. Imahori – *Chem. Phys. Lett.*, **2007**, *444*, 263–267.

[20] V. Mottaghitalab, G. M. Spinks, G. G. Wallace – *Synth. Met.*, **2005**, *152*, 77–80.

[21] P. C. Ramamurthy, W. R. Harrell, R. W. Gregory, B. Sadanadan, A. M. Rao – *Polym. Eng. Sci.*, **2004**, *44*, 28–33.

[22] C. Nastase, F. Nastase, A. Vaseashta, L. Stan-Iatin – Prog. *Solid State Chem.*, **2006**, *34*, 181–189.

[23] A.Nish, J.-Y. Hwang, J.Doig,R. J. Nicholas – *Nanotechnology*, **2008**, *19*, 095603.

[24] F. Chen, W. Zhang, M. Jia, L. Wei, X.-F. Fan, J.-L. Kuo, Y. Chen, M. B. Chan-Park, A. Xia, L.-J. Li – *J. Phys. Chem. C*, **2009**, *113*, 14946–14952.

[25] T. Schuettfort, A. Nish, R. J. Nicholas – *Nano Lett.*, **2009**, *9*, 3871-3876.

[26] Y. Kanai, J. C. Grossman – *Nano Lett.*, **2008**, *8*, 908–912.

[27] S. D. Stranks, C. Weisspfennig, P. Parkinson, M. B. Johnston, L. M. Herz, and Robin J. Nicholas – *Nano Lett.*, **2011**, *11*, 66–72.

[28] S. R. Scully, M. D. McGehee – *J. Appl. Phys.*, **2006**, *100*, 034907–034909.

[29] C. J. Brabec, V. Dyakonov, U. Scherf, Organic photovoltaics: materials, device physics, and manufacturing technologies. Wiley-VCH, Weinheim, 2008.

[30] M. Helgesen, S. A. Gevorgyan, F. C. Krebs, R. A. J. Janssen – *Chem. Mater.*, **2009**, *21*, 4669–4675.

[31] E. Geckeler, S. Samal – *Polymer Int.*, **1999**, *48*, 74–78.

[32] H. W. Kroto, J. R. Heath, S. C. O'Brien, R. F. Curl, R. E. Smalley – *Nature*, **1985**, *318*, 162–163.

[33] R. C. Haddon, L. E. Brus, K. Raghavachari – *Chem. Phys. Lett.*, **1986**, *125*, 459–464.

[34] R. C. Haddon – *Acc. Chem. Res.*, **1992**, *25*, 127–133.

[35] R. D. Johnson, D. S. Bethune, C. S. Yannoni – *Acc. Chem. Res.*, **1992**, *25*, 169.

[36] M. Cinke, J. Li, B. Chen, A. Cassell, L. Delzeit, J. Han and M. Meyyappan - *Chem. Phys. Lett.*, **2002**, *365*, 69–74.

[37] M. Bansal, R. Srivastava, C. Lal, M. N. Kamalasanan and L. S. Tanwar – *J. Exp. Nanosci.*, **2010**, 5, 412–426.

[38] L. S. Schadler, S. C. Giannaris and P. M. Ajayan – *Appl. Phys. Lett.*, **1998**, *73*, 3842–3844.

[39] F. Li, H. M. Cheng, S. Bai, G. Su and M. S. Dresselhaus – *Appl. Phys. Lett.*, **2000**, *77*, 3161–3163.

[40] M. Ham, G. L. C. Paulus, C. Y. Lee, C. Song, K. Kalantar-zadeh, W. Choi, J. Han and M. S. Strano – *ACS Nano*, **2010,** *4*, 6251–6259.

[41] D. J. Bindl, N. S. Safron and M. S. Arnold – *ACS Nano*, **2010,** ***4*****,** 5657–5664.

5. Experimental

Experimental is conceptually divided in two main topics: the first concerns single walled carbon nanotubes, their purification and characterization, which are respectively discussed in section 5.1 and 5.2. The second part is focused on single walled carbon nanotubes/ poly(3-hexylthiophene) composites, their preparation and characterization of the electrical and optical properties, respectively in section 5.3 and 5.4. Final section of the experimental describes a nanostructuring technique for the preparation of SWNT/P3HT composite films with nanoscale phase separation.

5.1 Purification of Single Walled Carbon Nanotubes

CVD single walled carbon nanotubes (SWNTs) were purchased from Thomas Swan & Co. Ltd. in the form of dry powder (*Elicarb SW dry*). Purification of this raw material has been done using a liquid oxidation approach. Properties of the final purified products have been investigated by various complementary techniques such as Atomic Force Microscopy (AFM), Thermogravimetric Analysis (TGA), Raman Spectroscopy and Near Infrared Photoluminescence (NIR-PL), to obtain a characterization as complete as possible of purified SWNTs samples. The purification process was developed starting with a preliminary study where best reaction condition were find out and concluding then with a final study where purification process is improved to obtain the final product.

5.1.1 Preliminary Chemical Oxidation

Ox-SWNTs (1) and (2)

The oxidizing agent chosen to fulfill the oxidation reaction responsible for the purification process of raw nanotubes was a mixture of concentrated sulfuric and nitric acids in a 3:1 ratio [1]. This mixture was reported to be more effective than nitric acid in removing carbonaceous impurities and metallic catalyst nanoparticles [2,3], typical by-products of nanotubes synthesis.

Oxidation reactions were typically conducted on 50 mg of the raw SWNTs. The acid mixture was carefully prepared adding an appropriate volume of concentrate (70 %) nitric acid to a volume of concentrated sulfuric acid (98 %) in order to have a H_2SO_4:HNO_3 ratio equal to 3:1. This mixture was added to the raw SWNTs to have a concentration of 2 mg/ml. Dispersion of the tubes into the oxidizing solution was obtained by ultrasonication for short time (~ 10 min) in a ultrasonic bath. The ultrasonication allows to break the bundles of SWNTs so all the material is evenly exposed and the acids molecules can penetrate deeply between each tube, executing their oxidizing action.

In this preliminary study, two distinct oxidation reactions were conducted at different temperatures for a fixed time to investigate any possible effect of the temperature on the oxidation's effectiveness and on the final product purity. The selected temperature for these two preliminary oxidation reactions were 20 °C (i.e. room temperature) and 120 °C, while the reaction time was fixed at 30 min. The product were called Ox-SWNTs (1) and Ox-SWNTs (2), respectively.

$$Raw\ SWNTs \xrightarrow{H_2SO_4/HNO_3\ (3/1),\ \ 20°C,\ \ 30\ min} Ox-SWNTs\ (1)$$

$$Raw\ SWNTs \xrightarrow{H_2SO_4/HNO_3\ (3/1),\ 120°C,\ 30\ min} Ox - SWNTs \quad (2)$$

Tab 5.1 summarize the experimental conditions of these two preliminary SWNTs oxidation.

Reaction	Oxidant	Raw SWNTs concentration	Time	Temperature
(1)	H_2SO_4/HNO_3 3/1	2 mg/ml	30 min	20 °C
(2)				120 °C

Tab 5.1 – Experimental conditions of preliminary SWNTs oxidation

Oxidation reactions were conducted under reflux and dispersions were keep under stirring. Noticeably, during the oxidation, brownish vapors develop during reaction (2) but not for reaction (1). This is a first indication of the effect of the temperature on nanotubes oxidation. The oxidation reactions were stopped after 30 minutes with carefully adding of Millipore water into the round bottom flask containing the dispersion to dilute the acid mixture. During this procedure, flasks were also placed into an ice bath. After the acid dispersions were cooled, they were filtered through a specific filter-holder assembly (Millipore ^{TM}) using a hydrophilic, acid-resistant, polycarbonate-based membrane filter (Isopore ^{TM}) having pores size of 0.22 μm. The filtration of the dispersions allows to retain nanotubes onto the filter, separating them from the acid solution filtered away. The filtrate passed through the filter was colorless for reaction (1) while it was brownish for reaction (2). Millipore water was added to wash any acid trace from the nanotube-rich residues deposited onto the filter. In order to avoid the occlusion of the membrane's pores, the surface of the filter was often scratched gently with a spatula. The filtration was continued until the pH of the filtrate was neutral, i.e. no acid was left in the residue. The purified materials were then collected from the filter and vacuum-dried. In fact, acid-treated nanotubes tend to strongly adsorb a large amount of water because of the polar groups introduced on their surface by the oxidation, which increase their hydrophilicity.

The final yields of the two oxidation reactions were calculated as the percentage ratio between the weight of the final purified material and the weight of the initial raw material. The yields obtained for the two reactions were very different: reaction (1) had a 90% yield while reaction (2) had a 10% yield.

From the preliminary oxidation reactions performed, it was therefore possible to conclude that suitable oxidation conditions should be strong enough to oxidize the carbonaceous impurities but not too strong in order not to consume significant quantities of SWNTs. For these reasons, it was decided to perform next oxidation reactions using an intermediate temperature of 70°C, that should represent a compromise between the two requirements stated above, still keeping a reaction time of 30 minutes as previous reactions.

5.1.2 Chemical Oxidation

Ox-SWNTs (3)

Raw SWNTs were therefore acid treated in the same conditions as before, with the exception of the reaction temperature, that was set at 70 °C. The product of this oxidation was named Ox-SWNTs (3).

$$Raw\ SWNTs \xrightarrow{H_2SO_4/HNO_3\ (3/1),\ 70°C,\ 30\ min} Ox-SWNTs\ (3)$$

Experimental conditions of oxidation reaction (3) are summarized in tab.2.

Reaction	Oxidant	Raw SWNTs concentration	Time	Temperature
3	H_2SO_4/HNO_3 3/1	2 mg/ml	30 min	70 °C

Tab 5.2 – Experimental oxidation conditions of Raw-SWNTs to Ox-SWNTs (3)

The final yield of the oxidation reaction in these conditions was 60%, an acceptable value, intermediate between those of 90% and 10% obtained from the preliminary oxidations.

Ox-SWNTs (4)

In the attempt to further improve the final purity a different strategy was adopted. Considered the great differences observed in purified products due to different oxidation temperatures, it was decided to fix a "safe" oxidation temperature of 70 °C and to increase the reaction time with the intent to allow a more effective oxidation of all the impurities while limiting SWNTs destruction in virtue of the low reaction temperature. For all these reasons, raw nanotubes were oxidized by acid treatment in similar conditions of Ox-SWNTs (3) but prolonging the reaction time up to 150 min, to give Ox-SWNTs (4).

$$Raw\ SWNTs \xrightarrow{H_2SO_4/HNO_3\ (3/1),\ 70°C,\ 150\ min} Ox-SWNTs\ (4)$$

Experimental conditions of oxidation reaction (4) are summarized in tab.3.

Reaction	Oxidant	Raw SWNTs concentration	Time	Temperature
4	H_2SO_4/HNO_3 3/1	2 mg/ml	150 min	70 °C

Tab 5.3 – Experimental oxidation conditions of Raw-SWNTs to Ox-SWNTs (4)

At the end of the reaction, the dispersion was cooled in an ice bath, diluted with Millipore water and filtered through the membrane filter, following the same procedure used for previous samples. Noticeably, for this sample, the acid filtrate solution showed a pale yellow color, which very likely indicates the presence of Fe(III), in presence of sulfate and nitrate anions deriving from the acid mixture. From data sheet suppliers, iron is the principal component of catalyst nanoparticles for the SWNTs CVD synthesis, therefore the pale yellow color of the acid filtrate may indicate a more effective removal of the catalyst. Especially in CVD SWNTs, metallic nanoparticle are mostly covered by graphitic multilayers [4] (whose formation during synthesis causes the inactivation of their catalytic action). These are referred to graphite encapsulated metal nanoparticles. Their removal from SWNTs samples is made difficult because nanoparticles and nanotubes usually have comparable oxidation rates due to their similarly stable structures. So it is not surprising that only with stronger oxidation conditions these graphitic nanoparticles could be oxidized and the encapsulated metal particles dissolved.

The black residue collected on the filter was then washed with MQ water to eliminate any residual acid until the filtrate was clear ad its pH was neutral, giving the final purified product, Ox-SWNTs (4).

5.1.3 Base-wash

Ox-SWNTs (3) and Ox-SWNTs (4) were subjected to a further purification step: a long (12 h), high temperature (100°C), reflux in a strong alkaline medium (NaOH 4M). This step is usually called "base-wash" because the intent is to facilitate the detachment from nanotubes sidewalls of the functionalized and unfunctionalized carbonaceous fragments formed during the oxidation reaction [5] so to wash them away.

$$Ox - SWNTs\ (3) \xrightarrow{NaOH\ 4M,\ 100\ °C,\ 12h} Bw - SWNTs\ (3)$$

$$Ox - SWNTs\ (4) \xrightarrow{NaOH\ 4M,\ 100\ °C,\ 12h} Bw - SWNTs\ (4)$$

50 mg of Ox-SWNTs (3) and Ox-SWNTs (4) were separately dispersed in 200 ml of NaOH 4M by short ultrasonication. The resulting dispersion was transferred into a Teflon container which was heated at 100 °C, under stirring, for 12 hours in nitrogen atmosphere. The basic aqueous dispersion was then filtered with the same setup used before after the acid oxidation. During filtration, the base-washed tubes were retained on the filter while a dark filtrate was collected below, indicating the effective removal of carbonaceous impurities. Nanotubes-rich residue was first washed with Millipore water until the filtrate was clear. Then the residue was recovered from the membrane filter and a second base-wash step was run in the same conditions than the first one. Differently than before, the filtrate of the second base reflux was clear since the beginning, evidencing that most of the removable impurities were already eliminate during the first washing step.

5.1.4 Bibliography

[1] J. Liu, A. G. Rinzler, H. Dai, J. H. Hafner, R. K. Bradley, P. J. Boul, A. Lu, T. Iverson, K. Shelimov, C. B. Hufman, F. Rodriguez-Macia, Y. Shon, T. R. Lee, D. T. Colbert and R. E. Smalley – *Science*, **1998**, *280*, 1253-1256.

[2] Y. Li, X. Zhang, J. Luo, W. Huang, J. Cheng, Z. Luo, T. Li, F. Liu, G. Xu, X. Ke, L. Li and H. J. Geise – *Nanotechnology*, **2004**, *15*, 1645-1649.

[3] J. Zang, H. Zou, Q. Qing, Y. Yang, Q. Li, Z. Liu, X. Guo and Z. Du – *J. Phys. Chem. B*, **2003**, *107*, 3712-3718.

[4] B. Ballesteros, G. Tobias, L. Shao, E. Pellicer, J. Nogues, E. Mendoza and M. Green – *Small*, **2008**, *4*, 1501-1506.

[5] C.G. Salzmann, S. A. Lliwellyn, G. Tobias, M. A. H. Ward, Y. Huh and M. Green – *Adv. Mat.*, **2007**, *19*, 883-887.

5.2 Characterization of Single Walled Carbon Nanotubes

Purified nanotubes were characterized using complementary techniques able to provide different information such as Atomic Force Microscopy (AFM), Thermogravimetric Analysis (TGA), Raman Spectroscopy and Near Infrared Photoluminescence (NIR-PL), to obtain a characterization as complete as possible of purified SWNTs samples.

5.2.1 Atomic Force Microscopy

AFM was used to obtain a direct visualization of the quality of the treated nanotubes after their deposition on substrates, allowing to evaluate the presence of amorphous carbon and the aggregation of nanotubes in bundles.

Sample preparation

Dimethylformamide (DMF), a good solvent for nanotubes, was used to prepare nanotubes dispersions having 0.05 mg/ml concentration. These dispersions were deposited onto freshly cleaved mica substrates by spray-coating and the resulting nanotubes films were analyzed by AFM.

Raw–SWNTs

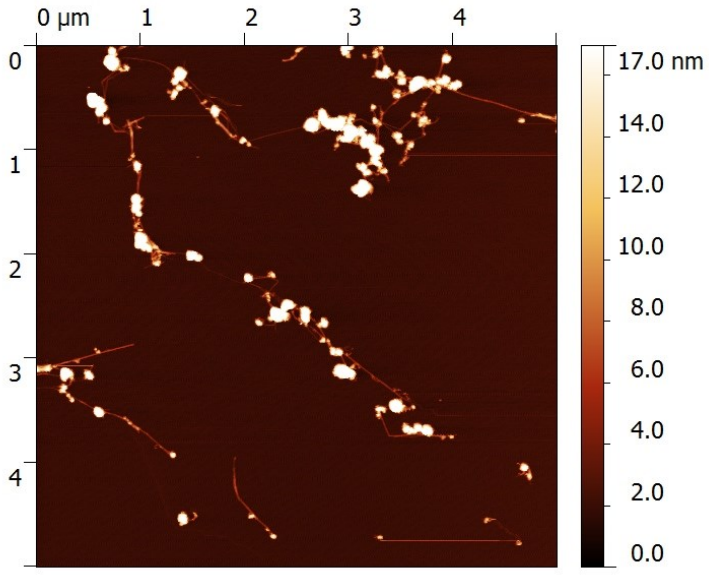

Figure 5.31 – AFM height image of raw SWNTs sprayed on mica.

AFM of raw nanotubes (figure 5.1) shows the presence of bundled SWNTs contaminated by characteristic carbonaceous impurities, mostly amorphous carbon, whose typical heights are about 20 nm.

Ox-SWNTs (1)

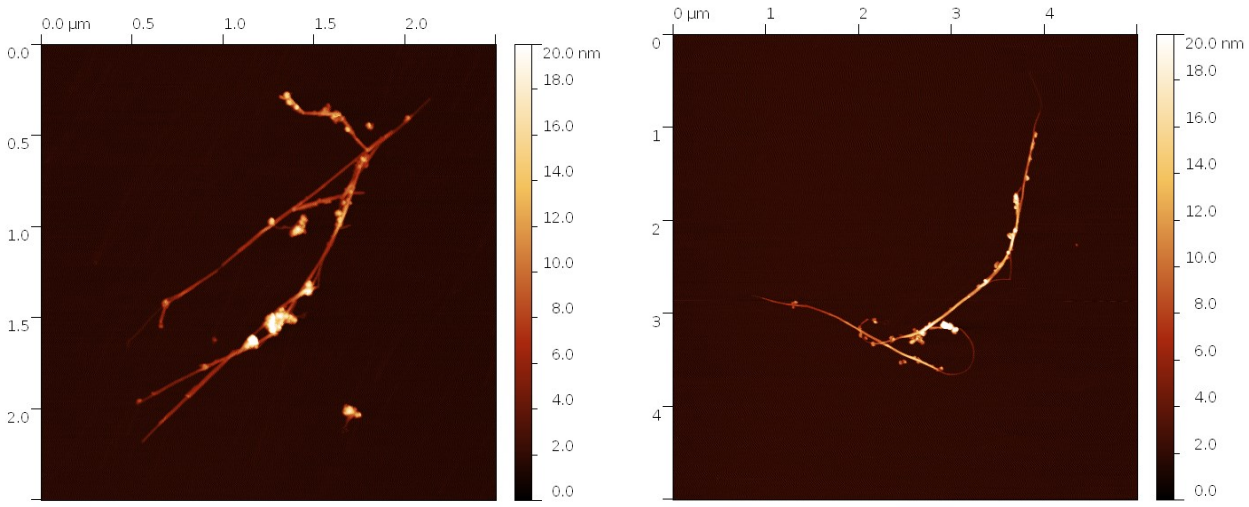

Figure 5.32 – AFM height images of Ox–SWNTs (1) sprayed on mica.

AFM of oxidized SWNTs obtained from the first oxidation reaction in tab.1 shows a result similar to raw nanotube, whith entangled nanotubes carrying amorphous carbon impurities attached to their sidewalls (figure 5.2).

Ox-SWNTs (2)

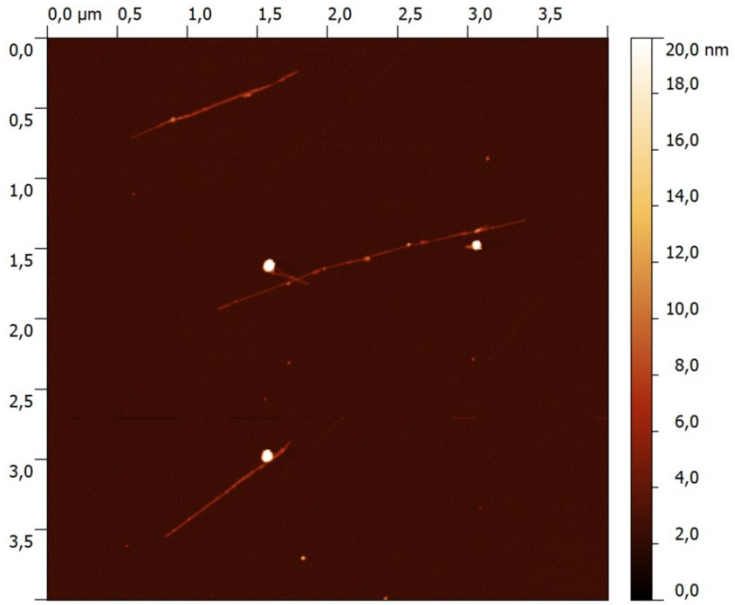

Figure 5.33 – AFM height image of Ox–SWNTs (2) sprayed on mica.

AFM image obtained from Ox-SWNTs (2) shows that stronger conditions due to the higher temperatures led to a more effective purification, because of removal of most of the amorphous carbon impurities and allowing also debundling of the tubes (figure 5.3). It has also to be noted that some nanotubes shortening due to the harsher conditions has probably occurred.

Drawing first conclusions from these preliminary oxidation reactions (tab.1), it can be observed that mild oxidation conditions of Ox-SWNTs (1) actually do not lead to any relevant improvement in the purity with respect to raw SWNTs, as confirmed by AFM where the amorphous carbon is clearly evident around the tubes, which are mostly present as small bundles. On the contrary, AFM of Ox-SWNTs (2) was interesting because it indeed showed a better purification degree with isolated tubes and very limited amounts of amorphous carbon, but it has to be said that the strong oxidation conditions led to a reaction yield too low to be acceptable. The strong difference in the final products obtained from these two oxidation reactions is a first indication of the marked effect of temperature on the oxidizing power of the acids mixture, even for short reaction times.

Ox-SWNTs (3) and Ox-SWNTs (4)

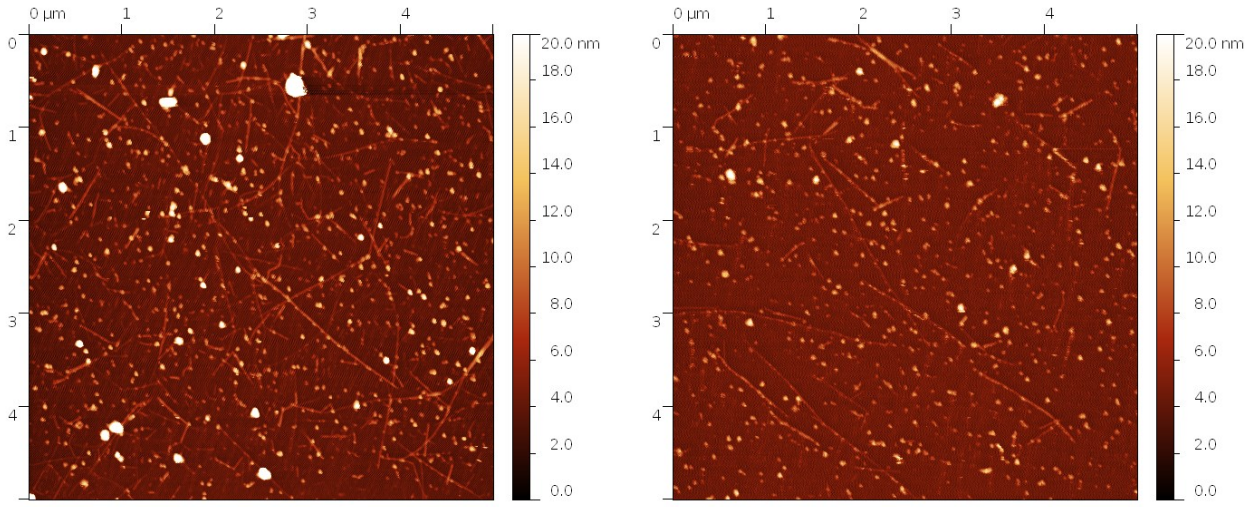

Figure 5.34 – (left) AFM height images of Ox–SWNTs (3) and (right) AFM height images of Ox–SWNTs (4) sprayed on mica.

AFM of Ox-SWNTs (3) (left image of figure 5.4) showed an intermediate situation between Ox-SWNTs (1) and Ox-SWNTs (2). It is evident the ability of the oxidation to cause the debundling of the nanotubes but a consistent amount of carbonaceous material is also present. Therefore it seemed necessary a further improvement of the purification process.

AFM analysis of Ox-SWNTs (4) (right image of figure 5.4) reveals that prolonging reaction time allows to obtain isolated nanotube with impurities of smaller dimension, which are therefore more likely removed by the base-wash step following the oxidation reaction.

Bw-SWNTs (3) and Bw-SWNTs (4)

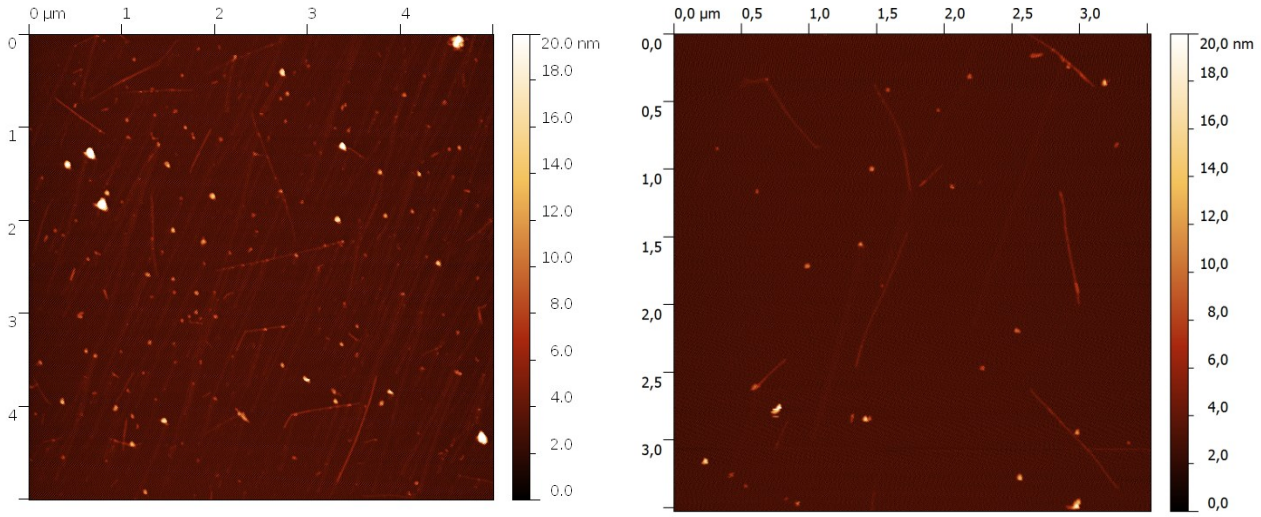

Figure 5.35 – (left) AFM height images of Bw–SWNTs (3) and (right) AFM height images of Bw–SWNTs (4) sprayed on mica.

AFM analysis of Bw-SWNTs (3) (left image of figure 5.5) showed indeed an great improving in the purification quality of the tubes compared to Ox-SWNTs (3) (fig.4). In fact, nanotubes in Bw-SWNTs (3) sample appear isolated, with lengths comparable with the raw (~ 1 µm), and with a limited amount of impurities, which remained in the sample because oxidation reaction did not succeed into their functionalization (so to make possible their removal by base washing) and much less into their completely oxidation. AFM analysis of Bw-SWNTs (4) (right image of figure 5.4) proved that a longer oxidation allows a higher degree of functionalization of the fragments, which permits a better purification through the base wash step, as evidenced by AFM. These final results undoubtedly highlight the successful of the developed purification scheme, able to produce nanotubes with an elevated purity degree.

5.2.2 Thermogravimetric Analysis

Thermogravimetric analysis (TGA) is typically used to estimate the amount of metal catalyst present in nanotubes sample. Metal particles are known to catalyze the thermal oxidation of carbon atom, so raw nanotubes containing the residual catalyst will burn at lower temperature with respect to purified nanotubes where catalyst was removed. The amorphous carbon has a much lower oxidation temperature than nanotubes, so the content ratio of SWNTs and amorphous carbon can be determined from their percentage mass loss in the TG curve [1].

Thermogravimetric analysis was executed on raw and oxidized nanotubes samples, summarized in tab 5.4.

Nanotube sample	Oxidation conditions
Raw	-
Ox-SWNTs (1)	20 °C – 30 min
Ox-SWNTs (2)	120 °C – 30 min
Ox-SWNTs (3)	70 °C – 30 min
Ox-SWNTs (4)	70 °C – 150 min

Tab 5.4 – Raw and oxidized nanotubes samples (with respective oxidation conditions) investigated by TGA.

TGA data were recorded in a range of temperature from 20 °C to 900 °C, but they were normalized at 100 °C in order to compare samples weights after water evaporation, because of the different tendency of raw and acid-treated nanotubes to adsorb humidity from the environment. In particular, acid treated are more sensitive because of the carboxyl, aldehyde, and other oxygen-containing functional groups created by oxidation, first on the surfaces of the non-nanotube carbonaceous fractions and then directly on nanotubes [2]. As a result, the carbonaceous fraction coating the nanotubes is extremely hygroscopic and reactive towards oxidation.

Since dangling bonds, defect and residual metal can initiate oxidation reactions, decomposition temperature, defined as the inflection point during oxidation of the tubes, is an estimate of sample's purity: higher value mean higher nanotube purity. Usually carbonaceous fractions begin to burn at 350°C and are mostly removed by oxidation below 550°C, whereas nanotubes are oxidized in air starting from 600°C.

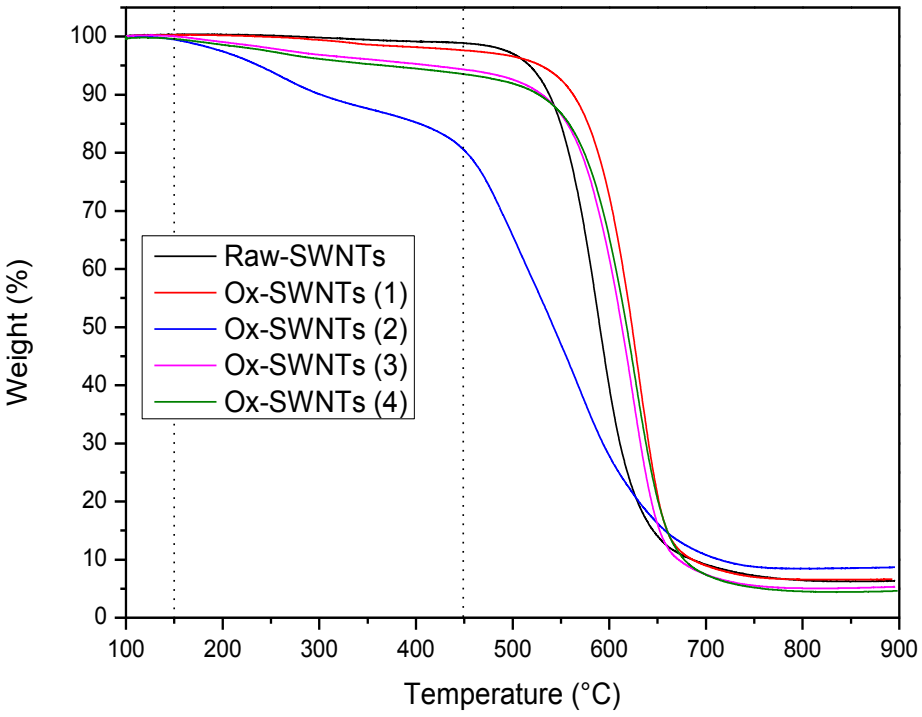

Figure 5.6 – Thermogravimetric curves for raw and oxidized nanotubes samples

The weight loss curves of SWCTs (figure 5.6) were divided into three regions corresponding where three different processes typically occur. A first region below 150 °C, mostly characterized by the evaporation of remaining physisorbed water, often accompanied by loss of few functional groups. A second region, between 150 and 450 °C, where loss of functional groups and oxidation of amorphous carbon occur, and finally a third region, above 450 °C where the oxidation of the SWNTs graphitic structure take place.

First derivative of thermogravimetric curves (figure 5.7) is used to obtain the oxidation temperature, defined as the maximum in the weight loss rate, in other words, the maximum of the thermal oxidation rate.

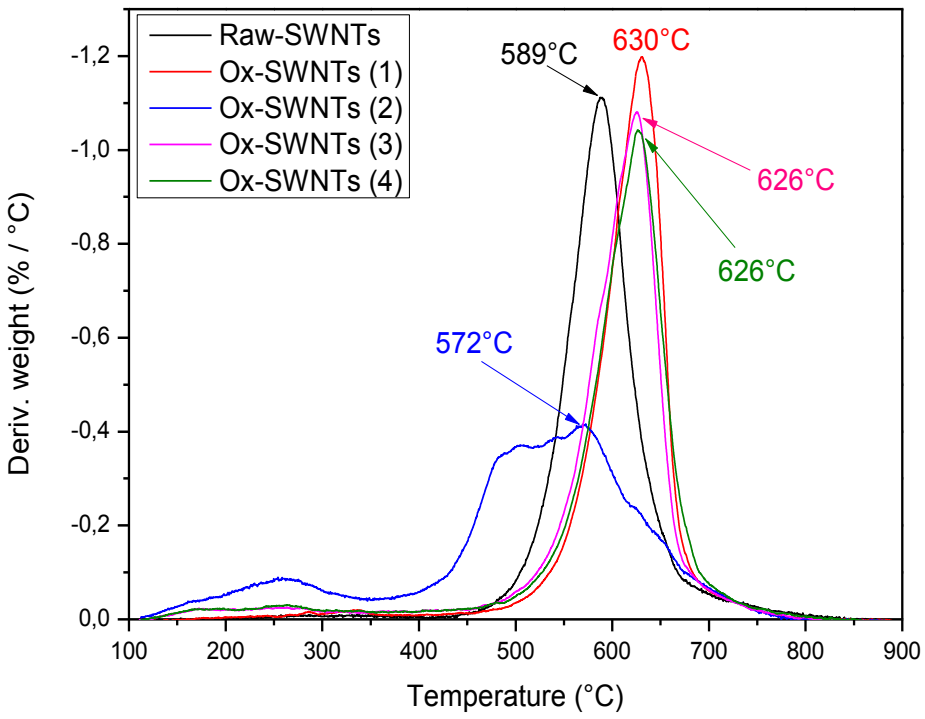

Figure 5.7– First derivative of thermogravimetric curves for raw and oxidized nanotubes samples

Raw-SWNTs

Raw nanotubes thermogravimetric curve exhibits a quasi-plateau in the region 150-450 °C with negligible weight loss, suggesting a limited presence of amorphous carbon and functional groups on SWNT. At higher temperatures, starting from 550°C, weight decreases rapidly indicating nanotubes oxidation. The oxidation temperature, defined as the maximum in the weight loss rate, can be inferred by the first derivative of the thermogravimetric curve obtaining a value of 589 °C. After the carbon material is completely oxidized, the final residue, consisting of metal oxides originating from the metallic catalyst present in the sample, is 6%.

Ox-SWNTs (1)

After the acid treatment at 20 °C for 30 min, the initial plateau starting from 150°C show no big deviations compare to raw nanotubes and this is easily predictable considering the soft oxidation conditions. Between 300 and 500°C a small weight loss occurs (~ 2-3%). This is very likely due to the thermal oxidation of some carbon material partially oxidized (i.e. made more reactive) by the acid treatment. Oxidation of the tubes occurs at higher temperatures (630°C) with respect to raw sample as can be seen from DTGA. Despite this, the final residue remains unchanged (~ 6%).

Ox-SWNTs (2)

TGA data of the nanotubes acid-treated at 120 °C for 30 min highlights that temperature used during the purification process has a strong effect on the integrity of the tubes. The weight loss curve starts to decrease at 150 °C and this trend proceeds markedly so that at 450 °C, before nanotubes oxidation formally begins, 20% of the initial weight is already lost. This behavior clearly evidence that reaction conditions used for purification are too harsh. The high temperature boosts the oxidizing power of the acids allowing them to attack directly the tubes in addition to the non-nanotube carbon material. The acid oxidation of the tubes creates defects (vacancies in the sp^2-framework), introduces oxygen-containing functional groups on their surface and it can lead to the extreme case of tube shortening [3,4]. All these factors lower nanotubes thermal stability. In fact, DTGA shows two broad bands instead than a sharp peak, indicating the presence of a large distribution of species with varying oxidation temperatures. The first band is centered at ~ 250 °C and it can be correlated to the oxidation of the amorphous carbon but also with dehydration and decarboxylation because of the increased number of functional groups on SWNTs sidewalls. The second band has a wide profile, extending between 500-600 °C, being the convolution of different peaks related to nanotubes with a variable degree of defect/functionalization and hence a variable susceptibility towards thermal oxidation. The higher oxidation temperature of this sample is 572 °C. The above statements further clarify the need to lower oxidation temperatures for nanotubes purification. The very high residue of is a common result whit strongly oxidized samples [5].

Ox-SWNTs (3)

Reducing the temperature of the acid oxidation of the tubes from 120°C to 70°C allows to obtain a weight loss curve showing a compromise between the two previous oxidation reactions. TGA data in fact show a limited weight loss of ~ 5 % in the first region (150-450°C), and a final 5 % residue, while DTGA give an oxidation temperature of 626 °C, higher than that of raw nanotubes, suggesting hence an improved quality of the sample.

Ox-SWNTs (4)

The increase of the reaction time to 30 to 150 minutes, keeping constant the temperature at 70 °C, showed some improvement in the final residue (4 %) and without decreasing the oxidation temperature 626 °C compared to Ox-SWNTs (3).

Tab 5.5 summarize all the data extrapolated from TGA and DTGA for raw and oxidized nanotubes samples, showing that finale oxidation conditions for purification represent a good compromise between nanotubes weight loss, oxidation temperature and final residue.

	Weight loss 150-450 °C	Weight loss 450-900 °C	Finale residue	Oxidation temperature
Raw-SWNTs	1 %	93 %	6 %	589 °C
Ox-SWNTs (1)	3 %	91 %	6 %	630 °C
Ox-SWNTs (2)	20 %	71 %	9 %	572 °C (broad band)
Ox-SWNTs (3)	6 %	89 %	5 %	626 °C
Ox-SWNTs (4)	7 %	89 %	4 %	626 °C

Tab 5.5– TGA and DTGA data for raw and oxidized nanotubes samples

5.2.3 Raman Spectroscopy

Raman spectroscopy was executed on raw nanotubes and on the oxidized and base-washed samples which showed best results in terms of final purification degree, namely Ox-SWNTs (3) and Bw-SWNTs (3), Ox-SWNTs (4) and Bw-SWNTs (4).

Sample Preparation

For Raman analysis, nanotubes in their powder form were simply placed onto a gold covered silicon substrate. Acquisition parameters were: 10 seconds exposition, 10% laser power, 1 accumulation. All Raman spectra were obtained using two different lines emitted from an Argon ion laser, a blue laser (488 nm) and a green laser (514 nm).

Raman spectra

Figure 5.8 and 5.9 show Raman spectra of nanotubes samples, between 1200 and 1700 cm^{-1}, the region characterized by the presence of the D and G bands, obtained using 488 and 514 nm laser, respectively. All Raman spectra were baseline corrected and normalized to the intensity of the G-band.

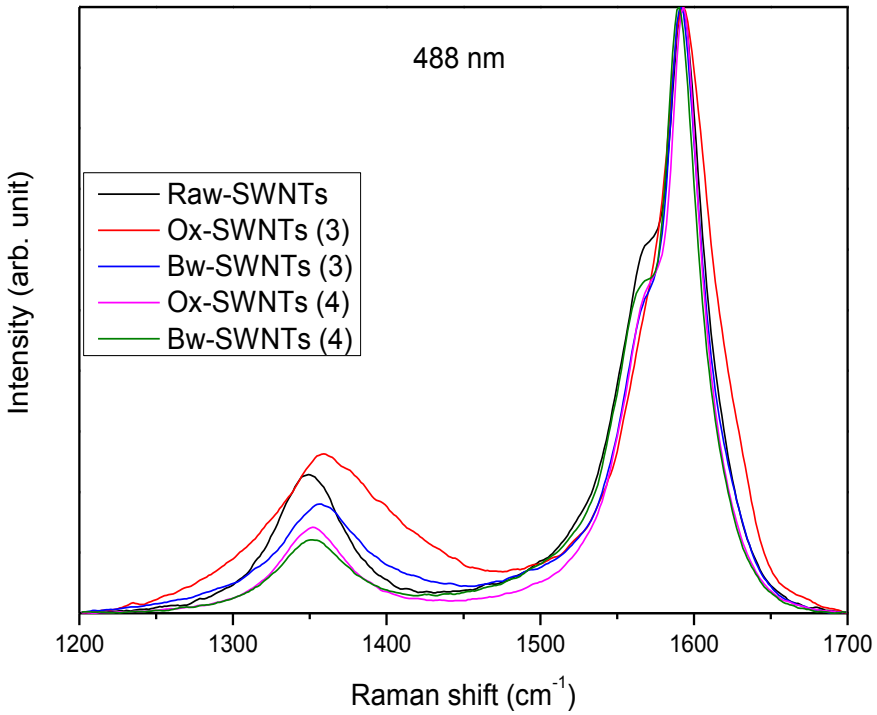

Figure 5.8 – Raman spectra of raw, oxidized and base-washed nanotubes (488 nm laser).

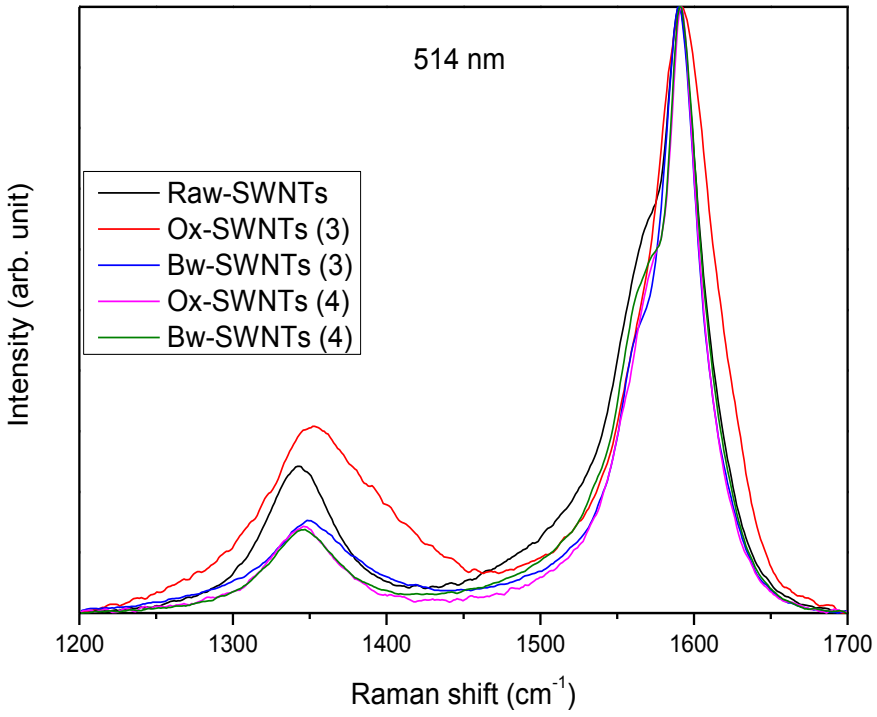

Figure 5.9 – Raman spectra of raw, oxidized and base-washed nanotubes (514 nm laser).

It is clearly evident that, compared to raw nanotubes, both D and G bands change their profile after chemical modification of the nanotubes through acid oxidations and following base-wash reactions.

Raw-SWNTs

Raman spectra of Raw SWNTs (black curve in figure 5.8 and 5.9) show a D-band at 1349 cm^{-1} and a G-band which exhibits an asymmetric line shape due to two components, G^+ at 1590 cm^{-1} and G^- at 1566 cm^{-1}. This profile can be fitted to a so-called Breit–Wigner–Fano line shape and is associated to metallic SWCNT. The intensity of the asymmetric shoulder can vary upon functionalization [6].

Ox-SWNTs (3)

Raman spectra of Ox-SWNTs (3) (red curves in figure 5.8 and 5.9) highlight a marked increase of the D-band area (whose peak is now shifted at 1360 cm^{-1}) correlated with an increase of the number of defects on the sample, namely vacancies and functional groups introduced onto nanotubes sidewalls, but also with the formation of amorphous carbon through partial oxidation of graphitic carbon, which is

known to confer a broader profile to the D-band. The G-band lineshape is strongly affected by the oxidation treatment, showing a reduction of the intensity of the G^- component. This is a common effect in acid-treated nanotubes and it is often correlated to a doping phenomenon by the intercalated acid molecules [7].

Bw-SWNTs (3)

Raman spectra of Bw-SWNTs (3) (blue curves in figure 5.8 and 5.9) show a reduction of the D-band area (now peaked at 1355 cm^{-1}) compared to Ox-SWNTs (3), evidencing a decrease in the amount of defects present in this sample. This is due to the effective removal of the functionalized carbonaceous fragments, formed during the first oxidation step. Noticeably the G-band reacquire its two components profile, probably because the base washing step allow to better wash away the intercalated acid molecules responsible of the doping in Ox-SWNTs (3) G-band.

Ox-SWNTs (4)

Raman spectra of Ox-SWNTs (4) (magenta curves in figure 5.8 and 5.9) are characterized by the D-band at 1351 cm^{-1} and the G-band at 1593 cm^{-1}. Comparing Raman spectra of Ox-SWNTs (4) and Ox-SWNTs (3), two main differences stand out: the area of the D-band of Ox-SWNTs (4) is almost half of the correspondent band in Ox-SWNTs (3) and the lineshape of the G-band of Ox-SWNTs (4) shows a smaller reduction of the G^- component, which still remains observable in the spectrum, in contrast to Ox-SWNTs (3). These two effects could seems contradictory considering that oxidation reaction that produce Ox-SWNTs (4) is five-times longer than that relative to Ox-SWNTs (3), so it would been expected the creation of a greater number of defects in nanotubes and therefore a bigger D-band in Ox-SWNTs (4). This results, on the contrary, suggest that longer reaction time allows to better digest the carbonaceous impurities both present in the as-received SWNTs and generated in the early phase of the oxidation (as confirmed by AFM). Hence, the increase of Ox-SWNTs (3) D-band of can be rationalized as due to the incomplete oxidation of the amorphous carbon, which creates new defects, dangling bonds and functional groups, all factors contributing to the increase of the D-band area. Increasing reaction time allows to better oxidize the carbonaceous impurity present.

It was actually proposed that acid oxidation of nanotubes proceeds through two different steps: an initial defect-generating step followed by a defect consuming step [8].

Bw-SWNTs (4)

Raman spectra of Bw-SWNTs (4) (green curves in figure 5.8 and 5.9) seem to confirm what stated above because both D-band and G-band show no shift compared with Ox-SWNTs (4) and D-band shows a limited area decrease after this base-washing step, indicating that there were less carbonaceous

fragments to wash away with respect to Bw-SWNTs (2). The G-band lineshape shows an increase in its G^- component to level comparable to Raw-SWNTs, due to the removal of residual intercalated acid molecules, as seen for Bw-SWNTs (2).

D/G Ratio

The structural quality of samples was characterized through the I_D/I_G ratio, which is the ratio between the intensities of D and G bands, conventionally considered an index of SWNTs purity (the lower, the better). The effect of the various chemical treatments on the two Raman bands of interest can be therefore highlighted through the I_D/I_G ratio.

I_D/I_G ratios for raw, oxidized and base-washed nanotubes samples were calculated on the average of three measures for both laser energies (figure 5.10).

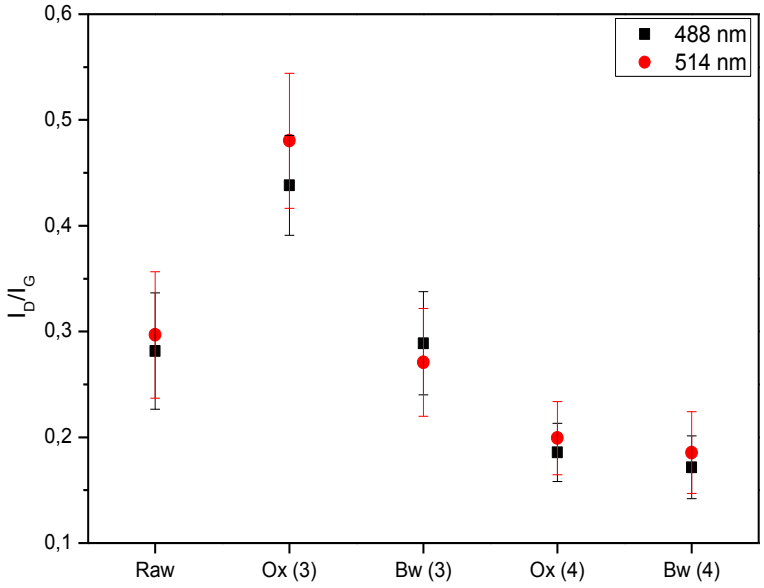

Figure 5.10 – I_D/I_G ratio for raw, oxidized and base-washed nanotubes

Compared to raw nanotubes, it is evident the initial increase of I_D/I_G after the acid oxidation at 70 °C for 30 minutes - Ox-SWNTs (3) - followed by a decrease due to the base-washing – Bw-SWNTs (3). I_D/I_G ratios of sample acid-oxidized at 70 °C for 150 minutes - Ox-SWNTs (4) – show a minor value compared to raw nanotubes, confirming the better efficacy of the longer oxidation reaction. Following base-wash step cause only a small decrease in the I_D/I_G ratios, indicating that most impurities are oxidized in the previous step, unlike the shorter oxidation reaction.

FWHM of D and G bands

D and G bands of raw and treated nanotubes samples, respectively in figure 5.11 and 5.12, highlight marked differences between the two oxidation reactions differing in time (Ox-SWNTs (3) and Ox-SWNTs (4)) and their respective successive base-wash steps (Bw-SWNTs (3) and Bw-SWNTs (4)) in terms of band profile and width.

Figure 5.11 show D-band profiles for raw, oxidized and base-washed nanotubes samples, measured after excitation with different lasers.

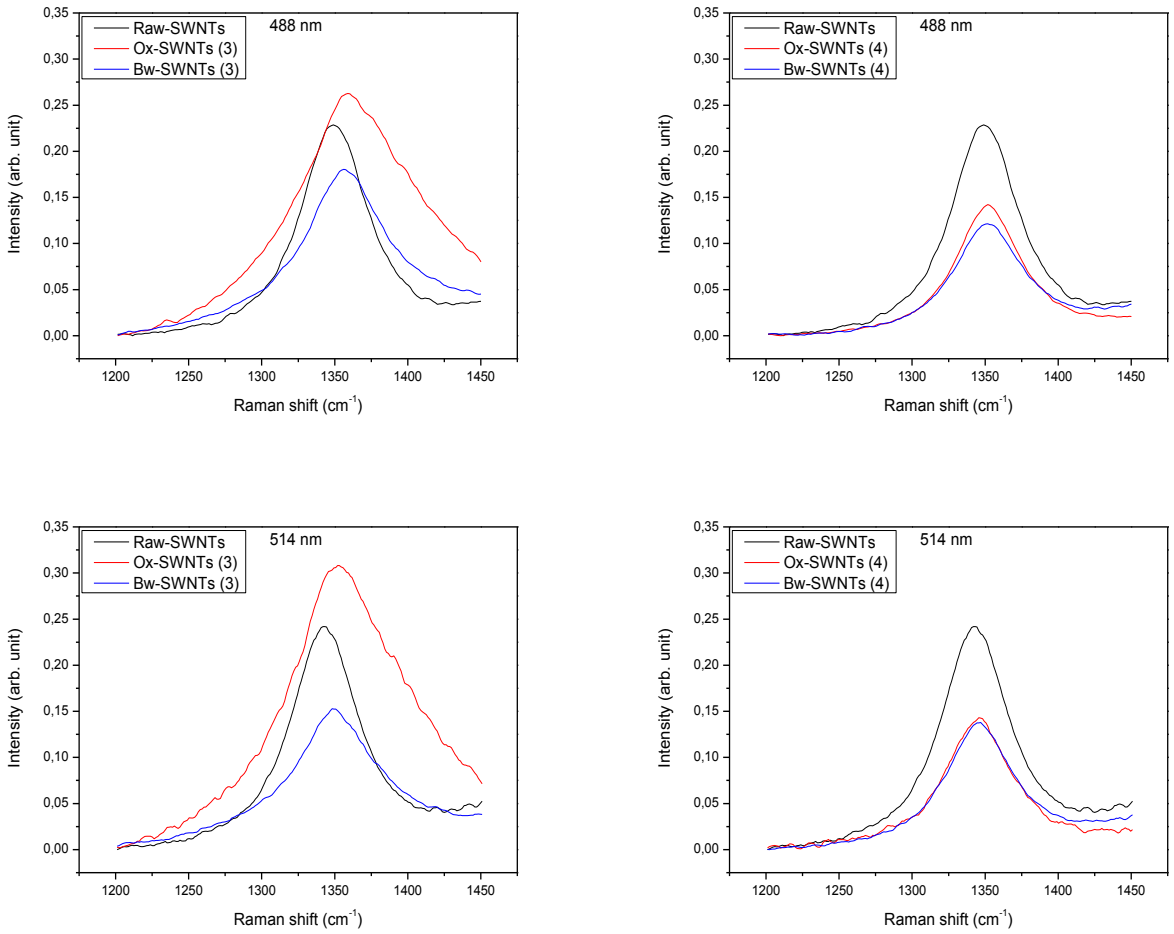

Figure 5.11 – D band of raw, oxidized and base-washed nanotubes

The relatively wide D band for raw nanotubes (FWHM ~ 55 cm^{-1}) suggests that other carbon species besides SWNTs are present in the as-produced material [9]. After short time acid oxidation - Ox-SWNTs (3) - the FWHM of the D band increase significantly to 99 cm^{-1}. The broadening of the D-band strongly suggests an increase amount of amorphous carbon, that is partially removed after the

next base washing step - Bw-SWNTs (3) - with a consequent reduction of the D-band FWHM (~70 cm^{-1}). Ox-SWNTs (4) shows a D-band FWHM similar to raw (~ 54 cm^{-1}), giving further indication of a minor degree of impurities compared to Ox-SWNTs (3), as evidenced by relative I_D/I_G ratios. Bw-SWNTs (4) exhibits a limited increase of the D-band FWHM (~ 59 cm^{-1}) despite the smaller area of the D-band, while the profile remains practically unaffected.

Figure 5.12 show G-band profiles for raw, oxidized and base-washed nanotubes samples, measured after excitation with different lasers.

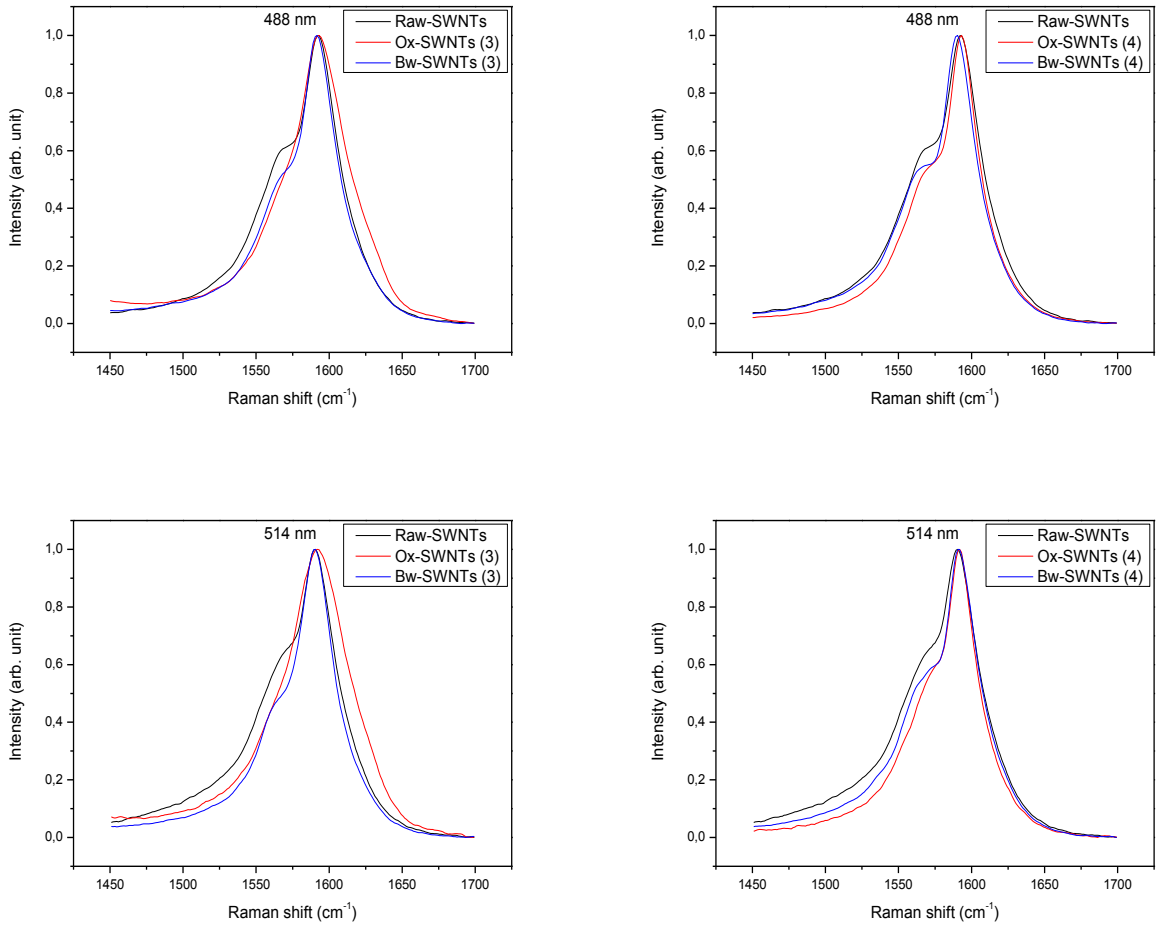

Figure 5.12 – G-band of raw, oxidized and base-washed nanotubes

For raw nanotubes, FWHM of G-band is ~ 50cm^{-1} for both lasers. The short acid oxidized sample - Ox-SWNTs (3) - shows a small decrease of G-band FWHM to ~ 48 cm^{-1} because of the upshift of the G^- component after the acid oxidation that narrows the G-band. Bw-SWNTs (3) shows a further decrease (FWHM ~ 43 cm^{-1}) despite the recovering of the G^- component lineshape because of its minor intensity

after the oxidation. Ox-SWNTs (4) G-band FWHM is ~ 44 cm^{-1} because of a smaller upshift of the G^- component compared to Ox-SWNTs (3) while G-band FWHM of Bw-SWNTs (4) is ~ 47 cm^{-1} due to recovering of the G^- component lineshape after base-washing step.

Full width at height maximum (FWHM) was used to quantify the effect of the various purification steps on the bandwidths (figure 5.13), showing that the D-band FWHM increase after short oxidation is partially recovered with the following base-wash, whereas long oxidation does not produce a similar increase, indicating a higher quality of the nanotubes. The following base-wash step shows limited effect on the D-band FWHM. On the other hand, it appears evident that G-band FWHM is less influence by chemical treatments, since its frequency mostly depend on the vibrations of the graphitic carbon atoms. Nevertheless, acid doping due to residual acid molecules can alters G-bands profile and FWHM, as evidenced by the variations between acid oxidized and base-washed samples.

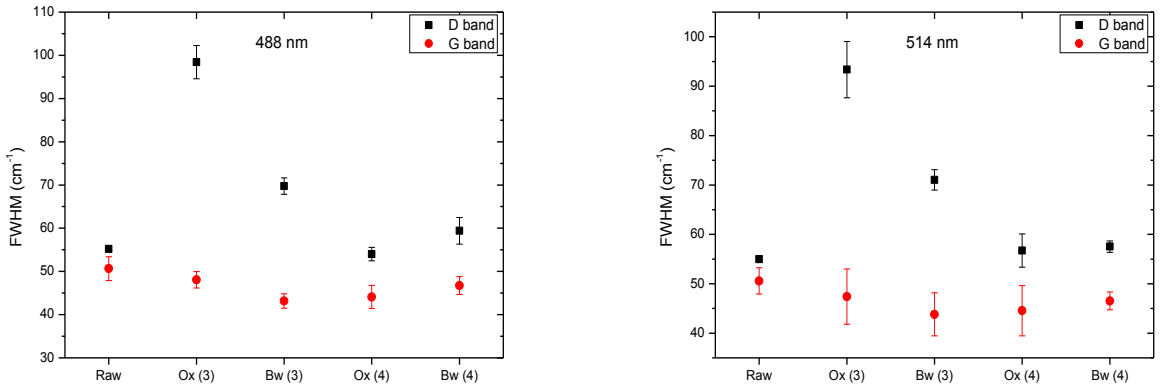

Figure 5.13 – D and G bands FWHM for raw, oxidized and base-washed nanotubes using 488 nm (left) and 514 nm (right) lasers

Peak shift of D and G bands

Peak shift of D and G bands in Raman spectra is usually observed upon heavy chemical functionalization of nanotubes [1]. In particular, downshift is interpreted as a softening and elongation of the C–C bonds upon electron transfer to the SWNTs, whereas upshift is caused by electron withdrawal from the sp^2 lattice that leads to a contraction and hardening of the lattice.

Peak shifts for D and G bands of raw, oxidized and base-washed nanotubes samples are reported in figure 5.14.

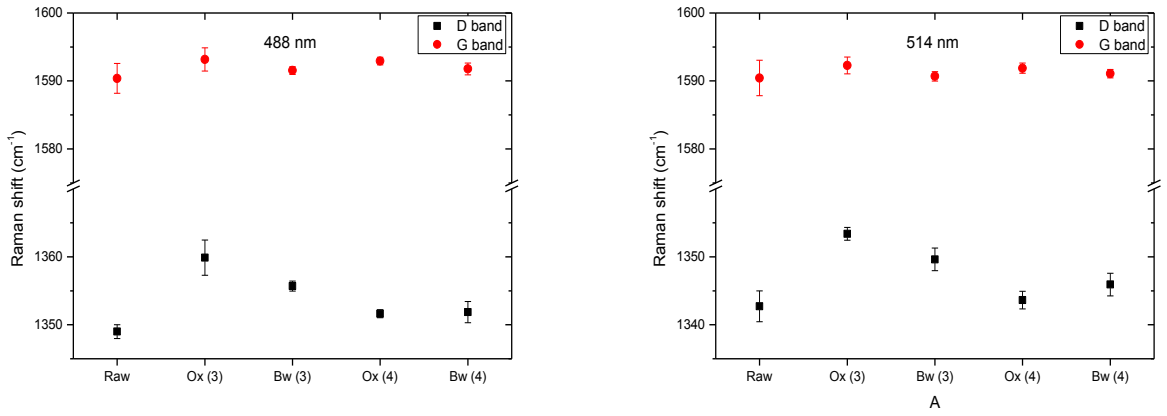

Figure 5.14 – D and G bands peak shifts for raw, oxidize and base-washed nanotubes samples

Observed D band peak shifts (black squares in figure 5.14) are generally larger compared to G band (red rings in figure 5.14) because D band is more deeply affected by chemical functionalization (as seen in figure 5.11). The short oxidation (Ox-SWNTs (3)) and following base-wash (Bw-SWNTs (3)) show the largest peak shifts for the D band, indicating strong modifications on the treated nanotubes with respect to raw sample. D band peak shifts of long oxidation (Ox-SWNTs (4)) and following base-wash (Bw-SWNTs(4)), on the contrary, are limited, suggesting a situation without deep functionalization, more similar to raw sample.

Nitric acid and sulfuric acid are known to lead to a p-type doping of SWCNTs that causes upshift of the G bands [6]. In fact, both acid-oxidized SWNTs samples show a small upshift compared to raw nanotubes, which is very likely induced by intercalated acid molecules [7]. Base-wash steps lower these upshifts because of the removal of the intercalated acid molecules.

Radial Breathing Modes - RBMs

Generally, oxidation of SWNTs leads to a modification of the RBMs compared to the starting material because of the destruction of smaller diameter SWNTs which have higher curvature and hence a higher reactivity towards oxidants. This is inferred from the lowering of the intensities of high wavenumber RBMs, since $\omega_{RBM} \sim 1/d_t$. In addition, changes in RBMs intensities can be also attributed to the reduction in resonance enhancement of functionalized SWNTs or to doping phenomena that modify populations of electronic levels and resonance conditions. It is important to note that changes in RBM intensities can also be induced by a variation in sample morphology.

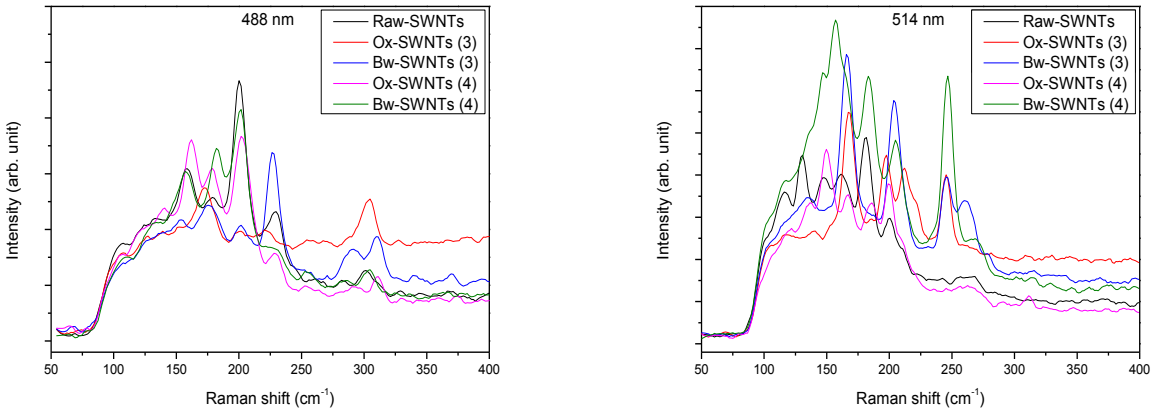

Figure 5.36 – RBMs for raw, oxidized and base-washed nanotubes

From the analysis of RBMs relative to raw, oxidized and base-washed nanotubes, it is possible note that most (practically all) RBM peaks are maintained and there is no evident RBM peak disappearing after oxidation, indicating that the oxidative process used for purification is capable to preserved nanotubes integrity even for smaller diameter SWNTs. The RBMs intensities are also generally preserved. Some peak shift due to functionalization or to the different aggregation state is also detected.

5.2.4 Near-Infrared Photoluminescence Spectroscopy

Near-infrared photoluminescence (NIR-PL) spectroscopy was executed on the same samples characterized by Raman spectroscopy, namely raw nanotubes, oxidized nanotubes Ox-SWNTs (3) and Ox-SWNTs (4) and base-washed nanotubes Bw-SWNTs (3) and Bw-SWNTs (4).

Sample preparation

Nanotubes were dispersed in an aqueous solution of sodium dodecylbenzenesulfonate (SDBS), one of the most used surfactant able to individually suspend nanotubes in water. Dispersion were prepared with a SWNT/SDBS/H_2O weight ratio of 1/25/12 and then sonicated for 30 minutes to facilitate nanotubes exfoliation from bundles so to be stabilized in water by surrounding surfactant molecules, remaining isolated and well dispersed in solution. After sonication, dispersions were centrifuged for 30 minutes at 13.000 g to precipitate heavier bundles, which are known to quench photoluminescence [11], leaving in solution only isolated tubes and smaller bundles comprising few tubes.

NIR-PL spectra

NIR-PL spectra of aqueous dispersion of nanotubes were obtained using a dedicated fluorimeter (*Applied Nanofluorescence*) that uses three distinct laser wavelengths of 638, 683, 785 nm to excite nanotubes in solution.

Raw-SWNTs

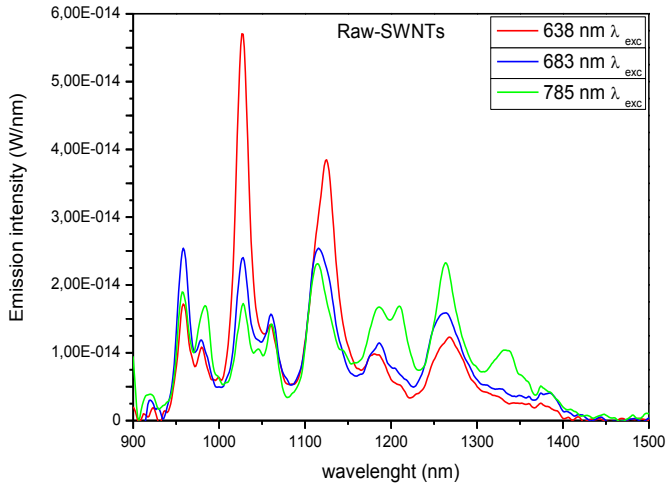

Figure 5.37 – NIR-PL spectra of Raw-SWNTs obtained using three different excitation wavelengths

Figure 5.16 shows raw nanotubes NIR-PL spectra, with typical sharp features due to the emission of photons with different energies, direct consequence of the ensemble of different nanotubes with different band-gap present in the sample [12].

Ox-SWNTs (3) and Ox-SWNTs (4)

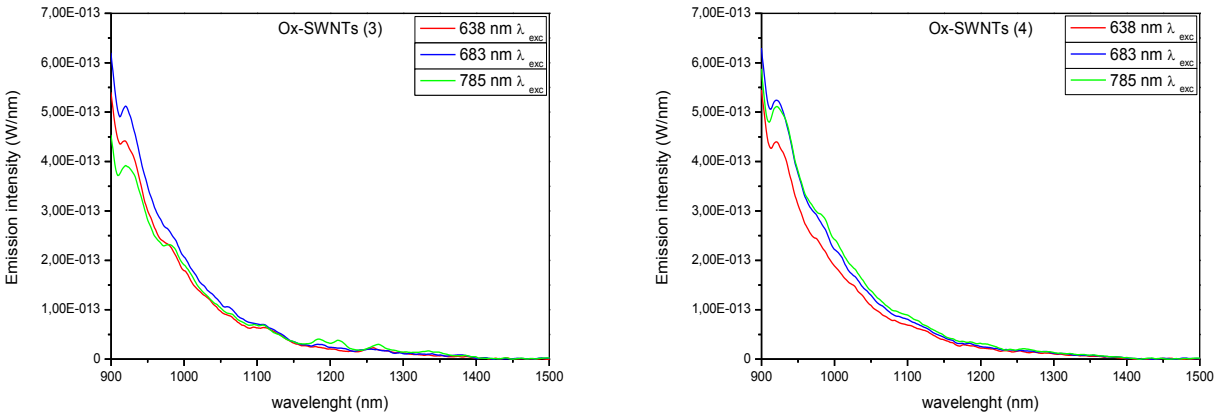

Figure 5.38 – NIR-PL spectra of Ox-SWNTs (3) (left) and Ox-SWNTs (4) (right) obtained using three different excitation wavelengths.

Figure 5.17 shows NIR-PL spectra of acid oxidized nanotubes, both for short time, Ox-SWNTs (3) (left image of figure 5.17) and for long time, Ox-SWNTs (4) (right image of figure 5.17). It is immediately evident a totally different behavior compared to raw nanotubes for both oxidized samples. These spectra are characterized by the total absence of sharp features and by a continuous background that increases at lower wavelengths. Although the first conclusion could be that acid oxidation caused severe damage to nanotubes electronic structure so that photoluminescence was quenched, it is worth noting that the intensities of the spectra for these oxidized nanotubes are roughly one order of magnitude higher than those characteristic of raw (fig.11), so it could be reasonable to make the hypothesis that nanotubes are still able to emit but their photoluminescence is covered by the higher-intensity background.

Bw-SWNTs (3) and Bw-SWNTs (4)

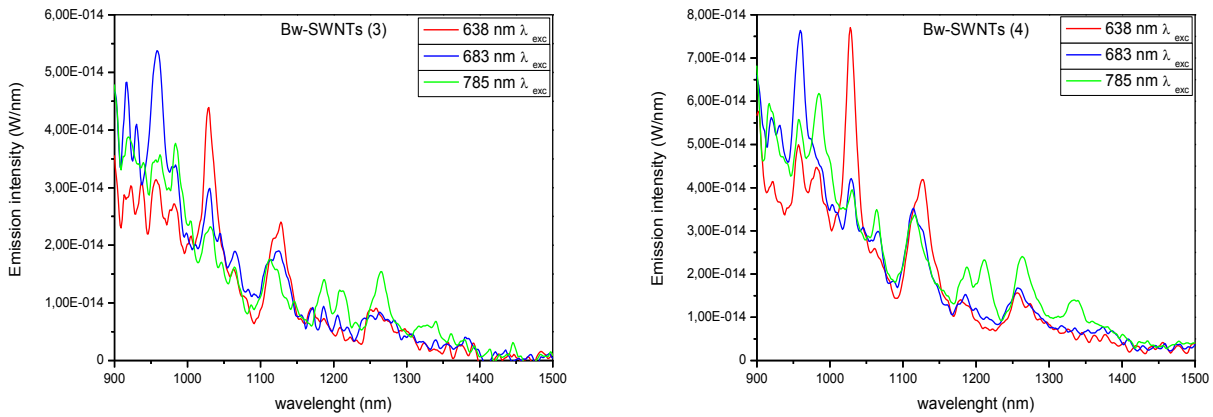

Figure 5.39 – NIR-PL spectra of Bw-SWNTs (3) (left) and Bw-SWNTs (4) (right) obtained using three different excitation wavelengths.

Figure 5.18 show NIR-PL spectra of base-washed nanotubes, after for short time oxidation, Bw-SWNTs (3) (left image of figure 5.18) and after long time oxidation, Bw-SWNTs (4) (right image of figure 5.18). These spectra allow to confirm the above hypothesis that nanotubes are still able to emit despite the acid oxidation they withstood. In fact both base-washed samples exhibit again typical photoluminescence spectra of nanotubes, characterized by the sharp features, which have comparable intensities to those relative of raw nanotubes, with the exception of a residual, low intensity, background, similar to that observed for oxidized samples.

The origin of the intense background in oxidized samples is still under investigation. No study are present in recent scientific literature about this effect but, in author's opinion, this background could be correlated to nanotubes acid oxidations, in particular, to the formation of carbonaceous fragments deriving from the breaking of nanotubes structures. The aromatic structure of such fragments, beyond being responsible for their π–π interactions with nanotubes sidewalls, confers to them the ability to interact with radiations, in particular emitting photons after excitation, in a totally similar way to that of the structure-correlated polycyclic aromatic hydrocarbon [13].

The restoration of nanotubes photoluminescence after base-wash processes seems to confirm this hypothesis, since base-washing does not affect directly nanotubes structure, but simply remove functionalized carbonaceous fragments adsorbed on nanotubes sidewall.

For comparison, NIR-PL spectra of raw and base-washed samples were reported for each laser energy.

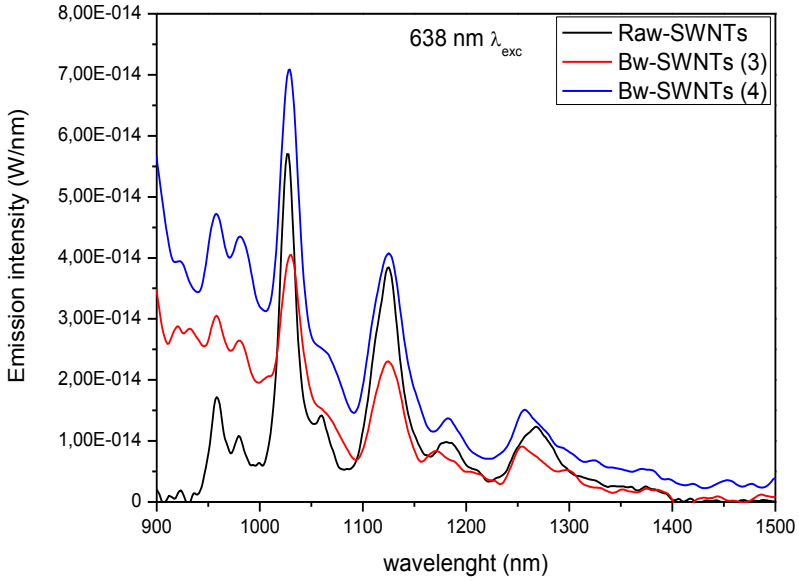

Figure 5.40 – NIR-PL spectra or raw and base-washed nanotubes obtained using 638 nm excitation

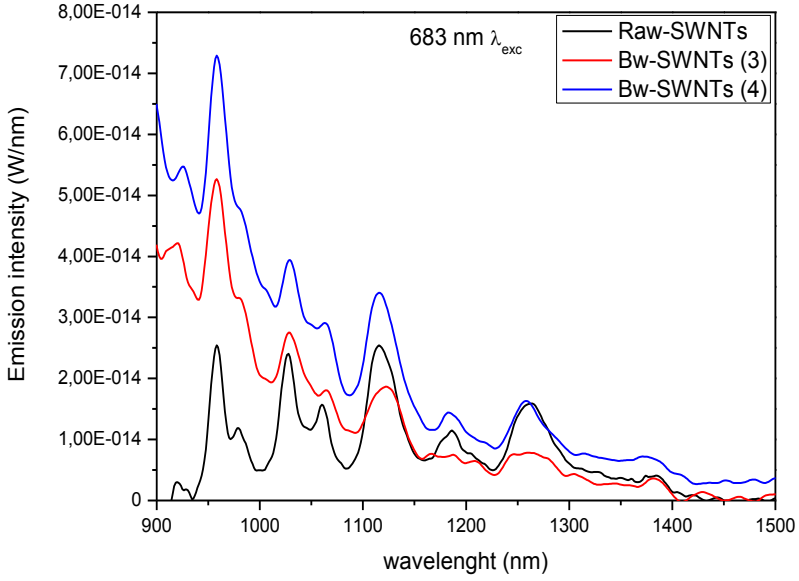

Figure 5.20 – NIR-PL spectra or raw and base-washed nanotubes obtained using 638 nm excitation

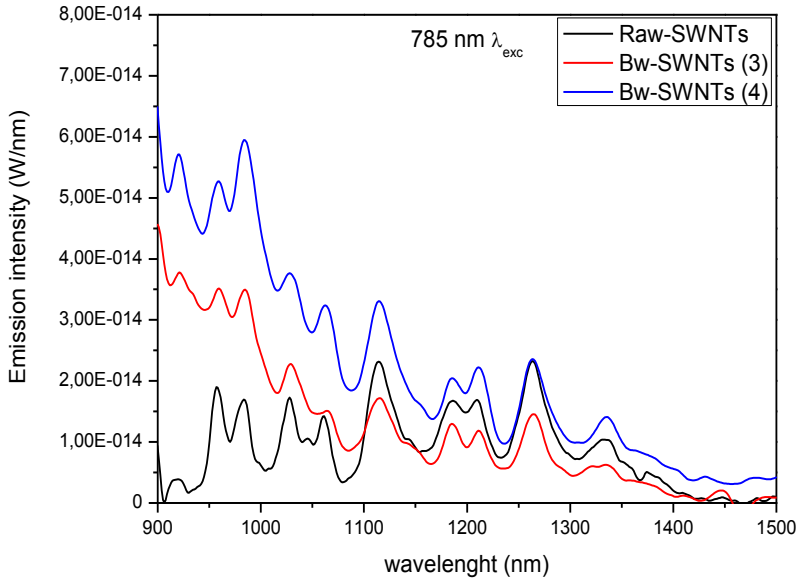

Figure 5.21 – NIR-PL spectra or raw and base-washed nanotubes obtained using 638 nm excitation

Comparison of NIR-PL spectra of raw and base-washed nanotubes clearly demonstrate that, despite the strong acid oxidation executed on the nanotubes, despite the unexpected photoluminescence spectra with no detectable characteristic emission from nanotubes measured for acid-treated samples, base-washed samples are again able to emit photoluminescence, in a similar way to raw nanotubes. In fact, spectra of base-washed samples show equal positions and comparable intensities of the peaks, considering the contribute of the non-linear background for treated samples.

Therefore considering that optical properties are strictly correlated to the integrity of the electronic structure, it is possible to affirm that this spectroscopic analysis proved that developed purification method based on the acid oxidation has effectively allowed to improve the purity of the nanotubes without affecting their electronic properties, legitimating their utilization in the preparation of organic electronic devices.

5.2.5 Bibliography

[1] R. Schönfelder, F. Avilés, A. Bachmatiuk, J. V. Cauich-Rodriguez, M. Knupfer, B. Büchner and M. H. Rümmeli – *Appl. Phys. A*, **2012,** *106*, 843–852.

[2] C. G. Salzmann, S. A. Llewellyn, G. Tobias, M. A. H. Ward, Y. Huh and M. L. H. Green – *Adv. Mater.*, **2007**, *19*, 883-889.

[3] K. J. Ziegler, Z. Gu, H. Peng, E. L. Flor, R. H. Hauge, and R. E. Smalley – *J. Am. Chem. Soc.*, **2005**, *127*, 1541-1547.

[4] K. J Ziegler, Z. Gu, J. Shaver, Z. Chen, E. L Flor, D. J Schmidt, C. Chan, R. H Hauge and R. E Smalley – *Nanotechnology*, **2005**, *16*, S539-S544.

[5] B. Ballesteros, G. Tobias, L. Shao, E. Pellicer, J. Nogues, E. Mendoza and M. Green – *Small*, **2008**, *4*, 1501-1506.

[6] M.S. Dresselhaus, G. Dresselhaus, R. Saito, A. Jorio, *Phys. Rep*., **2005**, *409*, 47.

[7] R. Graupner – *J. Raman Spectrosc.,* **2007,** *38*, 673–683.

[8] J. Zhang, H. Zou, Q. Qing, Y. Yang, Q. Li, Z. Liu, X. Guo and Z. Du – *J. Phys. Chem. B*, **2003**, *107,* 3712-3718

[9] A.C. Dillon, M. Yudasaka, M.S. Dresselhaus, *J. Nanosci. Nanotechnol.,* **2004***, 4*, 691.

[10] M. S. Dresselhaus, G. Dresselhaus, A. Jorio, A. G. Souza Filho, M. A. Pimenta and R. Saito. – *Acc. Chem. Res.*, **2002**, *35*, 1070-1078.

[11] M. J. O'Connell, S. Bachilo, C. B. Huffman, V. C. Moore, M. S. Strano, E. H. Haroz, K. L. Rialon, P. J. Boul, W. H. Noon, C. Kittrell, J. Ma, R. H. Hauge, R. B. Weisman and R. E. Smalley – *Science*, **2002**, *297*, 593-596

[12] R. B. Weisman – *Anal. Bioanal. Chem.*, **2010**, *396*, 1015-1023

[13] I. B. Berlman – Handbook of florescence spectra of Aromatic Molecules – Academic Pr. **197**

5.3 Electrical Properties of SWNT/P3HT Composites

Electrical properties of composites films were investigated through I-V curves in a Schottky diode configuration depositing composite P3HT/SWNTs thin films between the electrodes.

5.3.1 SWNT/P3HT dispersions

Regioregular poly(3-hexylthiophene) (rr-P3HT) (Aldrich, M_n 54000-75000, $M_w/M_n \leq 2.5$, head-to-tail regioregularity > 98%) was solubilized in chlorobenzene (CB) by gentle warming to give 0.5 mg/ml solution (1). Purified SWNTs were then dispersed in polymeric solutions with the aim to prepare composite dispersions with different P3HT/SWNTs weight ratios such as 10/1 - solution (2) – and 1/1 – solution (3). Ultrasonication through a tip sonicator (Hiescler, diameter of the tip 2mm, power 100W) was used to facilitate the dispersion of the tubes. The tip sonicator was used at 50% of its nominal power, with pulse of 0.5 seconds for 30 minutes. During the ultrasonic treatment, the solution was kept in an ice bath to minimize overheating with consequent solvent evaporation and/or polymer damage. Following the gradual dispersion of the tubes, color of solutions change from bright orange, characteristic of solution (1) to brown and then to black, when most of the tubes are exfoliated from the aggregates they were forming in the dry powder. For comparison, solution (1) was also subjected to the ultrasonic treatment of solution (2) and (3), in order to make comparable data from composites and pure polymer films. Solution (1), (2) and (3) will be deposited on a substrate as organic active layer between the electrodes of the diode. Characteristics of these solutions are summarized in tab 5.6.

		P3HT concentration	P3HT/SWNT ratio
Solution (1)	P3HT	0.5 mg/ml	-
Solution (2)	P3HT/SWNT		10/1
Solution (3)	P3HT/SWNT		1/1

Tab 5.6 – P3HT and P3HT/SWNTs composite solutions used as active layer in diodes

5.3.2 Substrate preparation

Substrates used for film deposition are obtained from a p-type silicon wafer (*Siegert Wafer*, orientation <100>, resistivity 10-20 Ohm/cm), cut in 1 cm^2 squares. They were first washed with MQ water and then shortly bath-sonicated in an ethanol-acetone solution to remove any organic adsorbed contaminant. After being dried under a stream of nitrogen, substrates were immersed for very short

time (~ 30 seconds) in a 5% aqueous solution of hydrofluoric acid to remove the native silicon oxide layer (which otherwise would act as a dielectric in the diode). Substrates were then extracted from the HF solution, washed with copious amount of acetone and stored under acetone to limit the re-oxidation of the surface. They were extracted from the solvent and dried with a stream of nitrogen just prior to organic film deposition.

5.3.3 Diode fabrication

All the diodes were fabricated using the HF-cleaned p-Si substrate as Schottky contact and Au as metal contact. In particular gold contacts are deposited onto substrates by sputtering evaporation, using a mask that allows to deposit gold spot with controlled diameter (2 mm).

The simplest diode prepared has no organic active layer between the electrodes. It consists only of the gold contact deposited onto the p-Si substrate (figure 5.22). This system is used as reference.

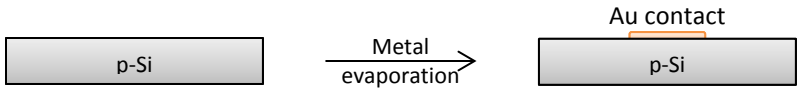

Figure 5.22 – Scheme of Si-Au diode fabrication.

Afterwards, organic active layers were deposited by spin-coating (50 µl, 500 rpm) on p-Si substrates using solutions (1), (2) and (3), obtaining, respectively, thin organic films (1), (2) and (3).

A batch of these three different samples were subjected to a thermal annealing treatment at 150°C under reduced pressure for 30 minutes, followed by a slow, stepwise cooling, with the intention to induce the reorganization of quickly-spun polymer films into more organized domains with higher crystallinity, which are characterized by improved charge transport, i.e. higher holes mobility for P3HT.

Gold contacts were then deposited onto each sample, annealed and not annealed, to complete the fabrication of the different diodes (figure 5.23).

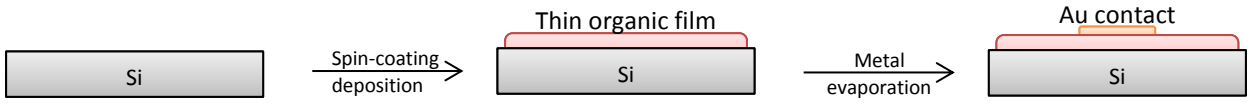

Figure 5.23 – Scheme of Si-thin organic film-Au diode fabrication.

5.3.4 Instrumentation

Electrical characterization of the fabricated diodes was executed using a Source Meter Unit (SMU) (*Keightley Instruments*), a device able to generate and measure currents and potentials. Samples are contacted placing them on a plate electrode and a needle electrode. The plate electrode is grounded while needle electrode is used to apply a sweeping voltage from negative to positive values (figure 5.24).

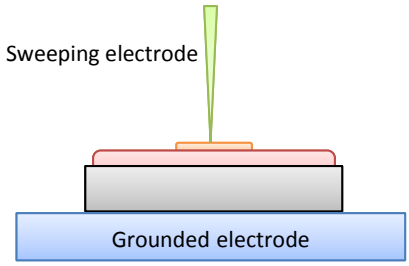

Figure 5.24 - Scheme of I-V measures set-up.

5.3.5 I-V curves

Current-Voltage characteristic of each diode were recorded sweeping the applied potential from -2 V to 2 V with 0.01 V steps and measuring the resultant current flowing through the device. The obtained current values were then reported as current densities J (mA/cm^2). J-V curves were measured in dark and in light, under the illumination of a yellow lamp which is part of the instrument equipment.

Silicon - gold diode

J-V curves of Si-Au diode (figure 5.25) were recorded as reference, in dark and light conditions (fig.4).

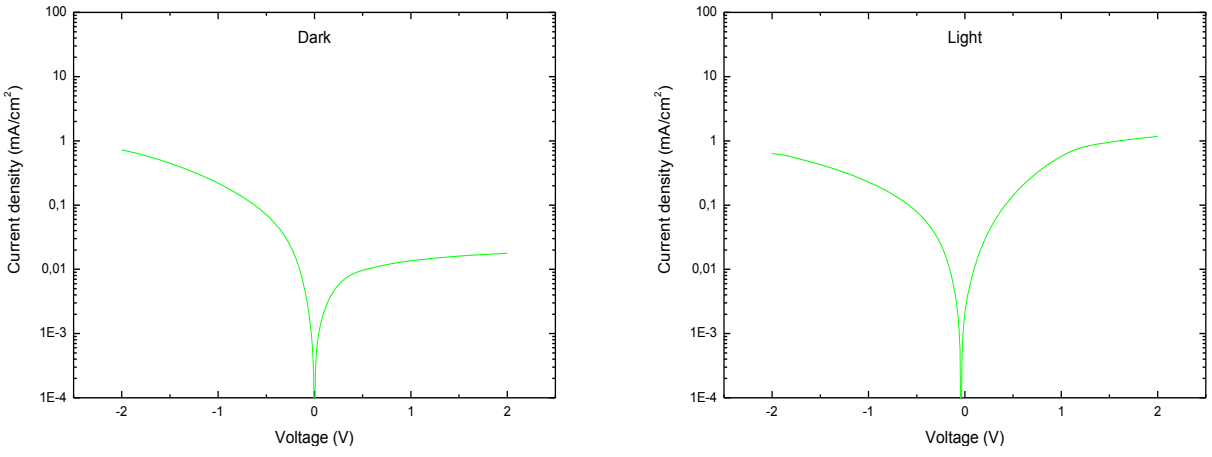

Figure 5.25 – Current density - Voltage curves for Si-Au diode, measured in dark (left) and under illumination (right).

In dark, the Si-Au diode shows a typical rectifying behavior, with forward and reverse current differing of two orders of magnitude (left image of figure 5.25). In this diode, characterized by a p-type semiconductor, the forward current is conventionally measured at negative potentials, because of the higher density of positive charge carriers. On the other hand, the current measured at positive potential is due to the minority carriers transport and it shows a saturation profile because of their lower density. In light (right image of figure 5.25), forward current is not affected by illumination whereas reverse current shows a marked increase because of the creation of new negative charge carrier created in the p-Si by photovoltaic effect.

Silicon - thin organic film – gold diodes

Diodes with different thin films deposited between electrodes (figure 5.23) are summarized in tab 5.7. The effect of thin film thermal treatment on the electrical properties of the device was also investigated.

Diodes thin organic films					
P3HT		P3HT/SWNT - 10/1		P3HT/SWNT - 1/1	
Unannealed	Annealed	Unannealed	Annealed	Unannealed	Annealed

Tab 5.7 – Different thin organic and composites films, unannealed and annealed, deposited between diodes electrodes

- **Diodes with unannealed organic films**

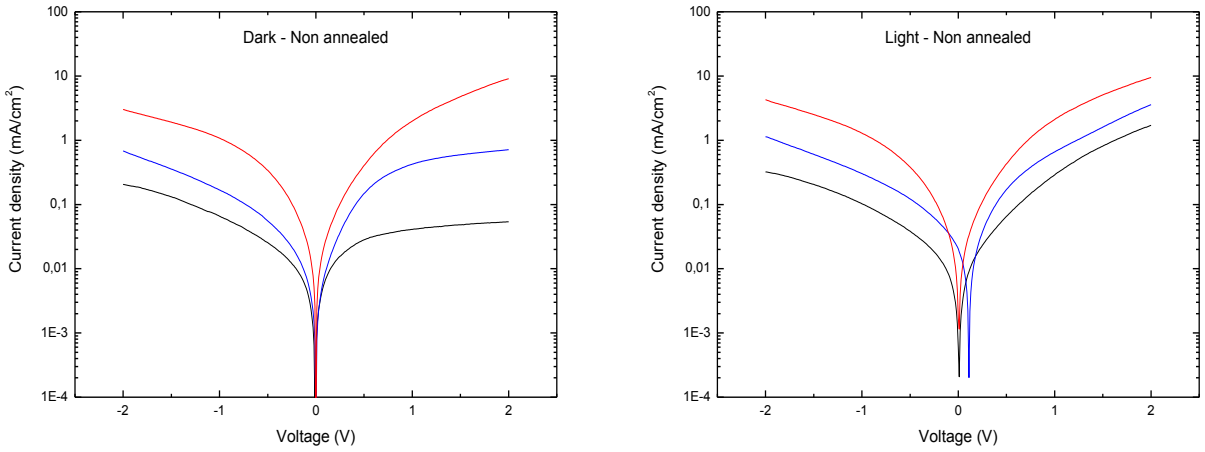

Figure 5.26 – J-V curves measured in dark (left) and under illumination (right) for diodes with unannealed organic thin films between electrodes. Black curve refers to P3HT, blue curve to P3HT/SWNT–10/1 and red curve to P3HT/SWNT–1/1.

P3HT

J-V curve in dark of diode with unannealed P3HT thin film (black curve in left images of figure 5.26) shows that rectifying properties are maintained because of the p-type nature of the polymer. Direct current is almost one order of magnitude higher of reverse current but measured current densities are slightly lower compared to the reference Si-Au diode because of the intrinsically different conductivity of the polymer. The behavior under illumination is different for the two branches of the curve (black curve in right images of figure 5.26) Direct current is practically not affected whereas reverse current is deeply modified. The effect of the illumination at positive voltages is correlated to the substrate (cf. right image of figure 5.25) where the photogeneration of free electrons occurs. These electrons are then able to pass through the polymeric layer to be finally collected by the sweeping electrode. The current measured at positive potential is even higher than that of the reference diode, indicating a contribute of the semiconducting polymer in the photogeneration of negative charge carriers.

P3HT/SWNT 10/1

J-V measures of this diode (blue curves in figure 5.26) shows that adding nanotubes modify the profile of the curves both in dark and under illumination. Noticeably nanotubes are able to increase the conductivity of both curve branches, so they are thought to facilitate both holes and electrons transport. In dark, direct current benefits of a smaller enhancement compared to the reverse current, whose increase is more than one order of magnitude. Therefore nanotubes seem to have a greater effect on electronic mobility. Despite the higher values of current densities, it has also to be noted that the profile of both branches of the J-V curve is analogue of the

previous P3HT diode, with a direct current increasing linearly with more negative potentials and a reverse current maintaining the saturation profile, characteristic of a diode with p-type semiconductor, in which current at positive potentials is limited because electrons are the minority charge carriers. Under illumination, the direct current is not influenced by the light, while reverse current shows an increase which is anyway lesser than that relative to the P3HT diode.

P3HT/SWNT 1/1

Diode characterized by such high nanotubes content shows enhanced currents densities of one and two orders of magnitude at negative and positive potentials, respectively (red curves in figure 5.26). The system is no more rectifying since comparable current densities are obtained at the end of the branches of the curves. Moreover, current at positive potentials becomes slightly higher than that at negative potentials, highlighting the deep effect of the nanotubes in the electrical transport properties of the composite material deposited between the two electrodes. From the profile of the curve, both in dark and under illumination, it is possible to conclude that nanotubes contribute to the electrical behavior is predominant over polymer and substrate, as also evidenced by the absence of any effect of the illumination on the measured current.

- **Diodes with annealed organic films**

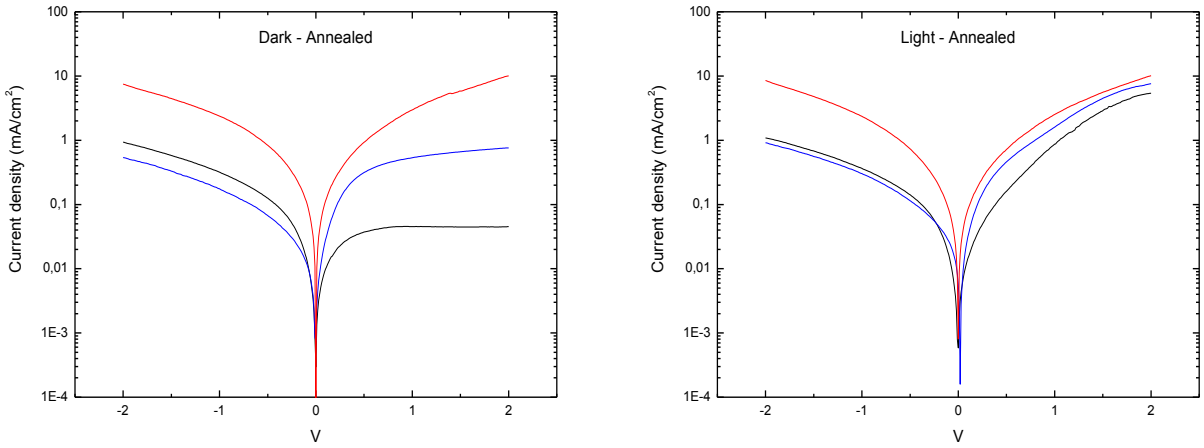

Figure 5.27 – J-V curves measured in dark (left) and under illumination (right) for diodes with annealed organic thin films between electrodes. Black curve refers to P3HT, blue curve to P3HT/SWNT – 10/1 and red curve to P3HT/SWNT – 1/1.

P3HT

J-V curve of diode with annealed P3HT thin film (black curves in figure 5.27) measured in dark shows the beneficial effect of the thermal treatment on the polymer hole mobility. In fact, direct current is almost one order of magnitude higher compared to unannealed sample (cf. black curve in figure 5.26). This is a direct consequence of the increased dimensions of crystalline domains after the annealing, which allows a higher interchain hole mobility. On the other hand, the reverse current is lower than the unannealed related sample, and the saturation current reveals that increasing the order of the polymer phase decrease its electronic mobility. Under illumination reverse current is increased to higher values than the direct current, similarly to the unannealed P3HT samples.

P3HT/SWNT 10/1

J-V curves of the device with the annealed P3HT/SWNT 10/1 composite thin film (blue curves in figure 5.27) show that in presence of nanotubes, the thermal treatment has a less pronounced effect on the conductivity. In fact, direct current density is lower compared to the annealed P3HT sample (black curves in figure 5.27). This effect could be attribute to the nanotubes in the polymer matrix, which hinder the polymer chains reorganization to form more crystalline domains, especially because of high aspect ratio of the nanotubes. On the other hand, reverse current is dramatically increased by nanotube presence, as seen also for unannealed sample (cf. blue curve in figure 5.26), further testifying that, in dark at positive potentials, conduction is strictly nanotube dependent and it is therefore not affected by the annealing of the polymer. Illumination is shown to have a small positive effect on the direct current, which reaches value

comparable to those of pure polymer, and a more pronounced effect at positive potentials where photogenerated electrons are more efficiently transported compared to the analogue unannealed sample.

P3HT/SWNT 1/1

Diode having the 1/1 composite annealed thin film shows J-V curves in dark and under illumination (red curves in figure 5.27) very similar to the ones measure for the unannealed sample (red curves in figure 5.26). Also in this case current densities are enhanced at least of one order of magnitude compared to the other samples, with the exception of the branch of the curve at positive potentials under illumination, where current densities of the three devices with different active layer are very similar. Like the analogue unannealed system with the same polymer/nanotube ratio, this device shows no more rectifying ability, since comparable current densities are obtained at the end of the branches of the curves. The quasi symmetric profile of the curves, whether they are recorded in dark or under illumination, whether the film was annealed or not, clearly indicates that electrical behavior of the device is exclusively dictated by nanotube, which allow to reach this very high current densities.

The ability to transport comparable quantity of electrical charge at opposite values of applied potentials makes these device characterized by a 1/1 polymer/nanotubes ratio a system capable of the so-called ambipolar charge transport, a peculiar electronic properties that can be used to fabricate field effect transistor and light emitting diodes characteristic based on nanotubes/polymer composite active layer.

For comparison, new composites films were prepared using as-received, CoMoCat, (7,6) semiconducting-enriched nanotubes (s-SWNT) (SouthWest NanoTechnologies) and P3HT.

Composite dispersions were prepared following the same procedure used before, with polymer/nanotube ratios of 10/1, 5/1, 2/1. Composites films were deposited on HF-cleaned p-Si substrates and gold contact were deposited to complete diodes fabrication.

J-V curves of these diodes characterized by different ratios between P3HT and s-SWNT were recorded in dark and under illumination (figure 5.28).

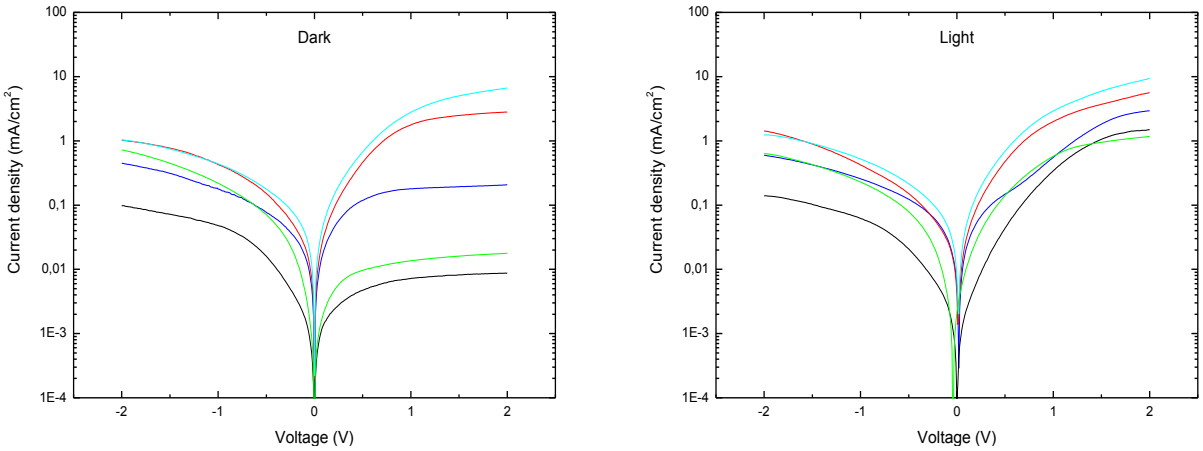

Figure 5.28 – J-V curves measured in dark (left) and under illumination (right) for diodes with organic thin films between electrodes. Black curve refers to P3HT, blue curve to P3HT/s-SWNT – 10/1, red curve to P3HT/s-SWNT – 5/1 and green curve to P3HT/s-SWNT – 2/1. Green curve refers to reference Au-Si diode.

P3HT

In dark, the diode with the polymeric film between electrodes conducts inevitably lower current compared to Si-Au diode because the semiconducting polymer represents a dielectric due to its lower conductivity with respect to the metals. In fact, direct current drops about one order of magnitude while the reverse current has a smaller decrease. In light, as before, only the branch at positive voltages is influenced by the illumination, carrying higher current than in dark, but lower than the illuminated Au-Si diode.

P3HT/s-SWNT 10/1

In dark, compared to pure P3HT, this system shows higher direct current while reverse current shows higher conductivity but a different profile, with an evident saturation regime caused by the limited number of the minority charge carriers (electrons) in the system. Under illumination direct current equals the original value of Si-Au diode while shows a reverse current even higher.

P3HT/s-SWNT 5/1

The increased nanotubes content in this system leads, in dark condition, to a resulting increase of the current both for negative and positive applied potential. It is notable that for this polymer/nanotubes ratio, the current due to the electrons migration is higher than that due to the holes moved by negative potentials, i.e. the inversion of the sign of the majority charge carriers has occurred. Therefore in this system the effect of the SWNTs on the electrical properties of the device is predominant, very likely because of the increase of electronic mobility nanotubes induces. For this same reason, illumination has no effect at negative potentials and it has only a limited effect on the electronic conductance, very likely induced by the substrate, as before.

P3HT/s-SWNT 2/1

In dark, the higher nanotubes concentration compared to previous sample has no measurable effect on the hole transport, hence current at negative potentials seems to become independent from nanotubes content. At positive voltages current continues to increase without any saturation plateau, indicating an efficient electron transport through the network formed by the nanotubes inside the polymer matrix. It is worth to emphasize that electron current in this system has increased of three orders of magnitude with respect to the diode with pure P3HT layer. The effect of the illumination on the current follows the previously evidenced trend, continuing to become less relevant with the increase of nanotubes fraction. Remarkably, using this 2/1 P3HT/s-SWNT ratio composite has led to the inversion of diode configuration. In fact, the higher (and hence direct) current is now obtained applying positive potentials and it is increased of one order of magnitude with respect to the reverse current measured at negative potentials. In other words, a simple variation of the weight fractions of the same two components has allowed to diametrically change the electrical properties of the device.

5.4 Optical Properties of SWNT/P3HT Composites

Optical properties of SWNTs/P3HT composites were investigated through UV-Vis absorption and emission spectroscopy to investigate the interaction between nanotubes and poly(3-hexylthiophene) and in particular the effect of the nanotubes on the optical properties of the polymer when they are in contact at molecular level because of their weak-forces driven self-assembly in supramolecular hybrid complexes [1].

5.4.1 Sample preparation

Three samples were prepared: (1) a pure P3HT solution, (2) a composite solution of P3HT/SWNTs in ratio 10/1 (w/w), (3) a composite solution of P3HT/SWNTs in ratio 1/1 (w/w). Chlorobenzene was used as solvent. P3HT concentration was always 0.5mg/ml, while SWNTs concentration was 0.05 mg/ml in solution (2) and 0.5 mg/ml in solution (3). Preparation of the two composite solutions required 1h of ultrasonic treatment to obtain the full dispersion of the nanotubes in the polymer solution. Solution (1) underwent an analogue ultrasonic treatment for comparison.

5.4.2 UV-Vis Absorption Spectroscopy

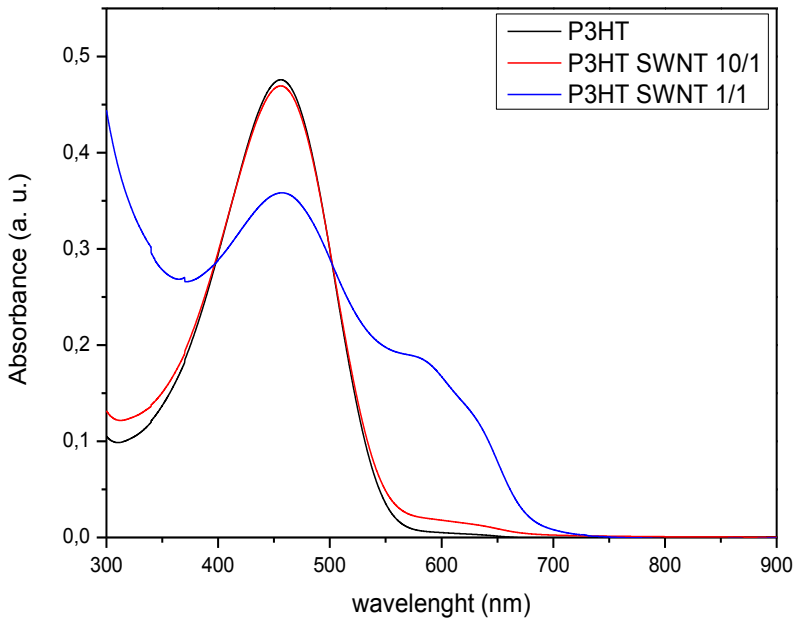

Figure 5.29 – UV-Vis absorption spectra of pure P3HT and composite P3HT/SWNTs solutions.

Absorption spectra of pure P3HT and composite P3HT/SWNTs solutions are showed in figure 5.29.

- P3HT solution exhibits an absorption spectrum with one single wide band characteristic of the π–π* transitions in the polymer, with an absorption maximum (λ_{max}) at ~ 455 nm.
- P3HT/SWNT 10/1 solution shows a spectrum very similar to that of pure polymer with the notable exception of the emergence of a red-shifted shoulder around 600 nm having very low intensity.
- P3HT/ SWNT 1/1 solution is characterized by the strong increase in intensity of the above-mentioned red-shifted shoulder at ~ 600 nm.

A red-shift in the absorption of a conjugated polymer is correlated with the formation of ordered polymer domains [2,3] which induce a greater delocalization of the electronic system, narrowing the band gaps between the electronic levels involved in the absorption of the light.

The appearance of the shoulder at ~ 600 nm is due to the presence of the nanotubes in the polymer solution. In fact, P3HT chains tend to interact strongly with SWNTs sidewalls through dispersive forces such as π–π interactions. This causes the chains to extend over the surface of the nanotubes, promoting their planarization, which in turn increase the conjugation length, red-shifting the absorption wavelengths [4].

Therefore the shoulder in the P3HT/SWNT 1/1 UV-Vis spectrum evidences the close interaction in solution between nanotubes and polymer. This interaction causes the formation of the so-called polymer/nanotube nanohybrid, which represents a two-component, nanoscale-composite system [5].

Another interesting point emerges comparing the absorption spectra of the P3HT/SWNT 1/1 solution and of a P3HT film (figure 5.30). This film was deposited by spin-coating at 500 rpm using 200 µl of solution (1).

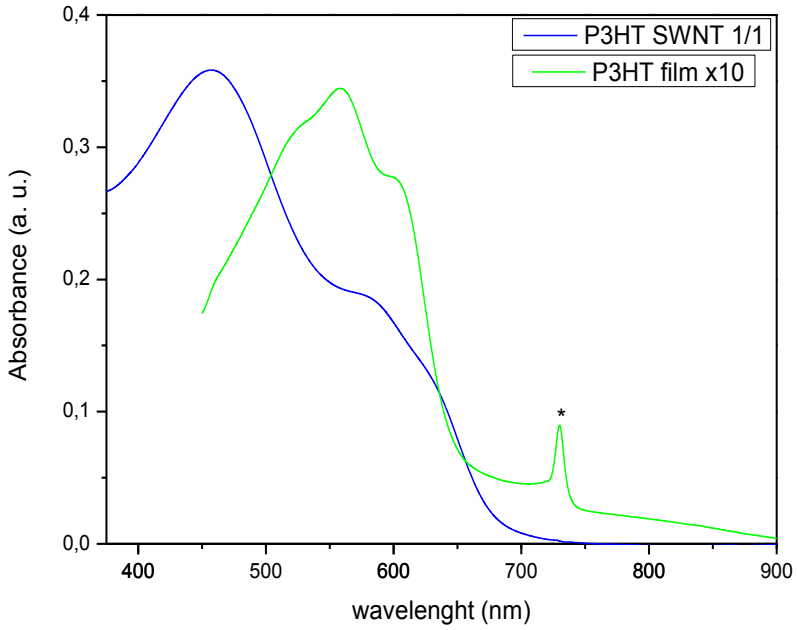

Figure 5.30 – Absorption spectra of the composite P3HT/SWNTs 1/1 solution (blue) and a spin-coated P3HT film (green). (marked peak is due to the transparent substrate)

Absorption peaks in the polymeric film are red-shifted in comparison to solution because of the higher order due to the self-organization of the P3HT during the formation of the film.

Neglecting the obvious different in intensity, it is worth noting that higher wavelength features in the spectrum of the polymeric film, relative to π–π^* interchains transition at 600 nm and 0–0 vibronic intrachain transition at 560 nm [6], fairly coincide with the absorption wavelengths of the nanohybrids in solution, clearly indicating that polymer chains adsorbed on nanotubes in solution show similar energy levels as in a pure polymeric film, This is a direct consequence of the high local order that polymer chains gain (despite being in liquid) after interacting with the nanotubes to form the nanohybrids.

5.4.3 Fluorescence Spectroscopy

Poly(3-hexylthiophene) is a highly fluorescent polymer. Fluorescence spectroscopy was used to investigate any modification of its emission profile after the interaction with the nanotubes.

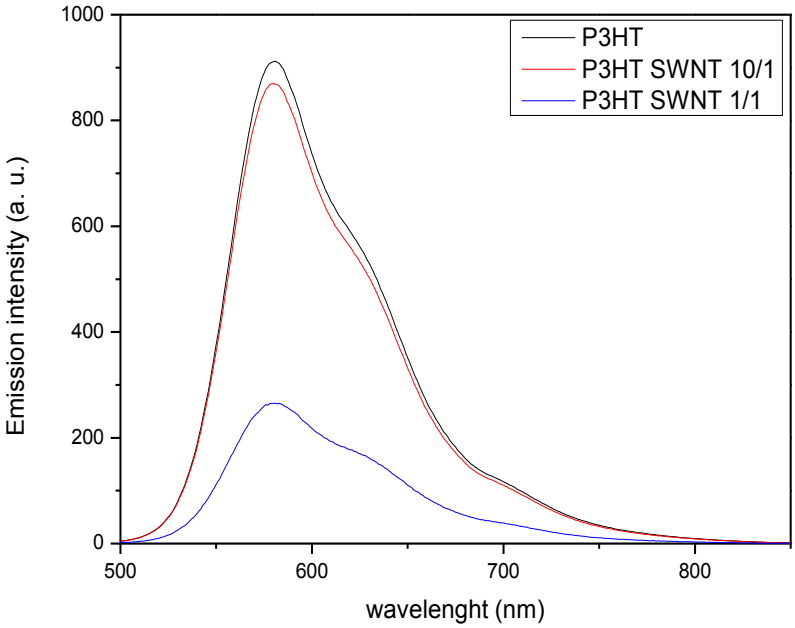

Figure 5.31 – Fluorescence spectra of pure P3HT and composite P3HT/SWNTs solutions.

Fluorescence spectra of pure P3HT and composite P3HT/SWNTs solutions are showed in figure 5.31.

- P3HT solution shows a typical fluorescence spectrum whose profile is determined by the contribute of different peaks, at ~ 669, 623 and 616 nm [6].
- P3HT/SWNT 10/1 solution exhibits the same profile of the pure polymer solution with very small decrease in the emission intensity.
- P3HT/SWNT 1/1 solution shows a strong quenching of the fluorescence induced by nanotubes.

It has been suggested that the exciton quenching occurs at the interface between the polymer and the nanotubes [7,8], and this was explained through of a type II band offset at these interfaces [4,9]. Spectroscopic studies on polymer-nanotube system have concluded that photoinduced interfacial charge separation occurs [10].

A fast transfer of photoinduced charges from a donor to an acceptor material is essential for an efficient photovoltaic device. In fact, after the exciton is generated, if the electron is not transferred

within few femtoseconds to the acceptor, it will decay to ground state emitting photoluminescence, resulting in poor efficiency of the photovoltaic device (i.e. photoinduced charge transfer and photoluminescence are competitive processes).

The photoinduced charge transfer occurring in the hybrid P3HT-SWNT system under investigation renders therefore this composite materials very promising for photovoltaic applications [11].

5.4.4 Bibliography

[1] T. Schuettfort, H. J. Snaith, A. Nish and R. J. Nicholas – *Nanotechnology*, **2010**, *21*, 025201.

[2] A. Ikeda, K. Nobusawa, T.Hamano and J. Kikuchi – *Org. Lett.*, **2006**, *8*, 5489-5492

[3] M. Giulianini, E. R. Waclawik, J. M. Bell, M. De Crescenzi, P. Castrucci, M. Scarselli and N. Motta – *App. Phys. Lett.*, **2009**, *95*, 013304.

[4] T. Schuettfort, A. Nish and R. J. Nicholas, *Nano Lett.*, **2009**, *9*, 3871-3876.

[5] T. Schuettfort, H. J. Snaith, A. Nish and R. J. Nicholas – *Nanotechnology*, **2010**, *21*, 025201.

[6] P. J. Brown, D. S. Thomas, A. Kohler, J. S. Wilson, J. Kim, C. M. Ramsdale, H. Sirringhaus and R. H. Friend – *Phys. Rev. B*, **2003**, *67*, 064203.

[7] P. J. Goutam, D. K. Singh and P. K. Iyer – *J. Phys. Chem. C*, **2012**, *116*, 8196−8201.

[8] P. Imin, F. Cheng and A. Adronov – *Polym. Chem.*, **2011**, *2*, 411-416.

[9] Y. Kanai and J. C. Grossman – *Nano Lett.*, **2008**, 8, 908-912.

[10] A. J. Ferguson, J. L. Blackburn, J. M. Holt, N. Kopidakis, R. C. Tenent, T. M. Barnes, M. J. Heben and G. Rumbles – *J. Phys. Chem. Lett.*, **2010**, *1*, 2406-2411

[11] S. D. Stranks, C. Weisspfennig, P. Parkinson, M. B. Johnston, L. M. Herz, and R. J. Nicholas – *Nano Lett.*, **2011**, *11*, 66-72

5.5 SWNT/P3HT Nanohybrids

It is well known the tendency of semiconducting polymer to interact with nanotubes driven by weak forces. This interaction leads to the adsorption of the polymer onto nanotubes sidewalls. Polymers chain can adhere in a straight or in a spiral conformation depending on the polymer's flexibility and on nanotube's diameter. The latter case is referred as wrapping. The results of this interaction is a self-assembled nanohybrid system which exhibits interesting properties because the intimate contact between these two materials makes possible interactions such as energy and electron transfer from one component to the other [1–4].

For these reasons, a method for the preparation of the nanohybrids (NHs) [5–7] was developed and NHs films were deposited and analyzed by Atomic Force Microscopy (AFM).

5.5.1 Nanohybrids synthesis and purification

Nanohybrids synthesis was based on the initial mixing of equal amounts of Single Walled Nanotubes (SWNTs) and poly(3-hexylthiophene) (P3HT). A fraction of the polymer interacts with the nanotubes forming the nanohybrids while the remaining fraction remains free. In order to obtain purified NHs, the excess of free polymer has to be removed. This goal was obtained through a solvent extraction method based on an iterative sequence of physical steps.

Regioregular poly(3-hexylthiophene) (rr-P3HT) (Aldrich, M_n 54000-75000, $M_w/M_n \leq 2.5$, >98% head-to-tail regioregular) was solubilized in chlorobenzene (CB) by gentle warming to give 0.5 mg/ml solution. Purified SWNTs were then dispersed in P3HT/CB solution with a 1:1 P3HT:SWNTs ratio. The dispersion was promoted by tip sonicator (Hiescler, diam of the tip 2mm, 100W), at 50% of its nominal power, with 0,5 sec pulsed, for 30 min. In order to avoid solvent evaporation during ultrasonication, the dispersion was kept in an ice bath for the entire treatment. Following the proceeding dispersion of the tubes in the polymer solution, the color of the dispersion changed from bright orange, characteristic of the P3HT in CB, to brown and then to black, when most of the tubes are exfoliated from the aggregates they were forming in the dry powder. It is possible to notice also some violet reflection that, it is worth to note, is characteristic of crystallized P3HT. It is well known the ability of SWNTs to nucleate polymer crystallization on their sidewalls [8]. Therefore in the SWNTs/P3HT dispersion, P3HT is expected to be partly in intimate contact with the nanotubes and partly free in solution.

The solvent extraction of the nanohybrids from the polymer-rich solution is accomplished by the addition of a volume of toluene equal of the initial CB volume. Toluene is known to be a good solvent for P3HT and a poor one for SWNTs [9,10]. Therefore adding toluene decreases the overall solubility of the nanohybrids, causing their aggregation (in fact, solution becomes cloudy), leaving free P3HT well solubilized.

Centrifuging the hybrid solution at 13.000g for 10 min led to the precipitation of a black nanohybrids-rich deposit on the bottom of the centrifuge tube, leaving a brownish polymer-rich supernatant. This upper fraction was discarded while precipitated nanohybrids were redispersed in fresh toluene by means of the tip sonicator. Ultrasonication allows to temporarily disperse nanohybrids in toluene, facilitating the dissolution of the eventual free polymer remained after first centrifugation. Turning off the ultrasonication results in the rapid reaggregation of the NHs because of their bad solubility in toluene. NHs dispersion was then subjected to a second centrifuging cycle, at 13.000g for 10 min, and, as before, supernatant was removed and NHs-residue was redispersed again in toluene to undergo a further cycle of centrifuge. After this last centrifugation, supernatant was colorless, so it was decided to stop the solvent extraction process at this stage, considering that further cycles could be detrimental because of NHs loss. The NHs residue obtained at the end of the process was finally dispersed in chloroform, to take advantage of its volatility for the deposition of NHs films.

Steps for synthesis and solvent extraction of SWNTs/P3HT nanohybrids are reported in figure 5.32.

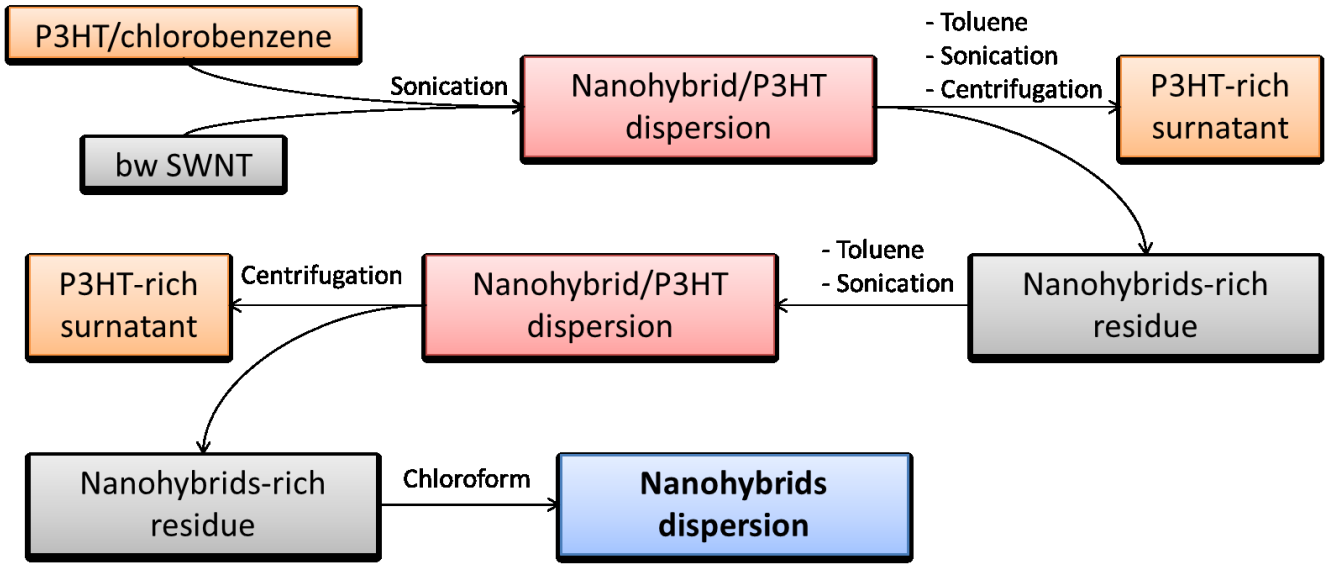

Figure 5.32 – Scheme of synthesis and solvent extraction method of nanohybrids

5.5.2 Deposition Techniques of Nanohybrids Films

Thin P3HT-SWNT hybrid films were deposited through drop-casting and spin-coating techniques. The former simply consist in the spreading of very small volumes of the dispersion on a substrate (~ 10 µl). Film forms after spontaneous solvent evaporation. This technique is simple and fast but it is not easily reproducible and the covering is not always uniform. In addition, when used with dispersed nanomaterials, it may suffer of their reaggregation, driven by the slow evaporation rate of the solvent. In spin-coating technique, substrates are fixed to a rotating base, bigger volumes (~ 100 µl) are poured on them and films formation occurs through a sequence of one or more programmed spinning ramps of the base. This technique allows to control the thickness of the deposited film through the experimental parameters (angular velocity and duration of the spinning ramps) and to obtain films having different morphologies than the drop- casted ones. The nanomaterial reaggregation issues are limited because of the fastest deposition rate.

Substrates preparation

Substrates used for deposition were obtained from a Si <100> wafer. All substrates were cut in 1 cm^2 squares in order to keep constant the area available for film deposition. These substrates were first washed with MQ water and then shortly bath-sonicated in an ethanol-acetone solution to remove any adsorbed organic contaminant. Substrates were finally dried under a stream of nitrogen and immediately used for film deposition.

5.5.3 AFM of Nanohybrids films

Nanohybrids films deposited using drop-casting and spin-coating techniques were investigated by AFM to investigate their different morphologies caused by different deposition techniques.

Film deposited by drop-casting

Drop-casted films were initially deposited as a preliminary check of the content of the hybrid dispersion obtained after the solvent extraction process. These first results were very encouraging because of the successful NHs enrichment of the starting 1:1 polymer/nanotubes composite dispersion through the solvent extraction process and because of the unusual and promising morphologies obtained (figure 5.33).

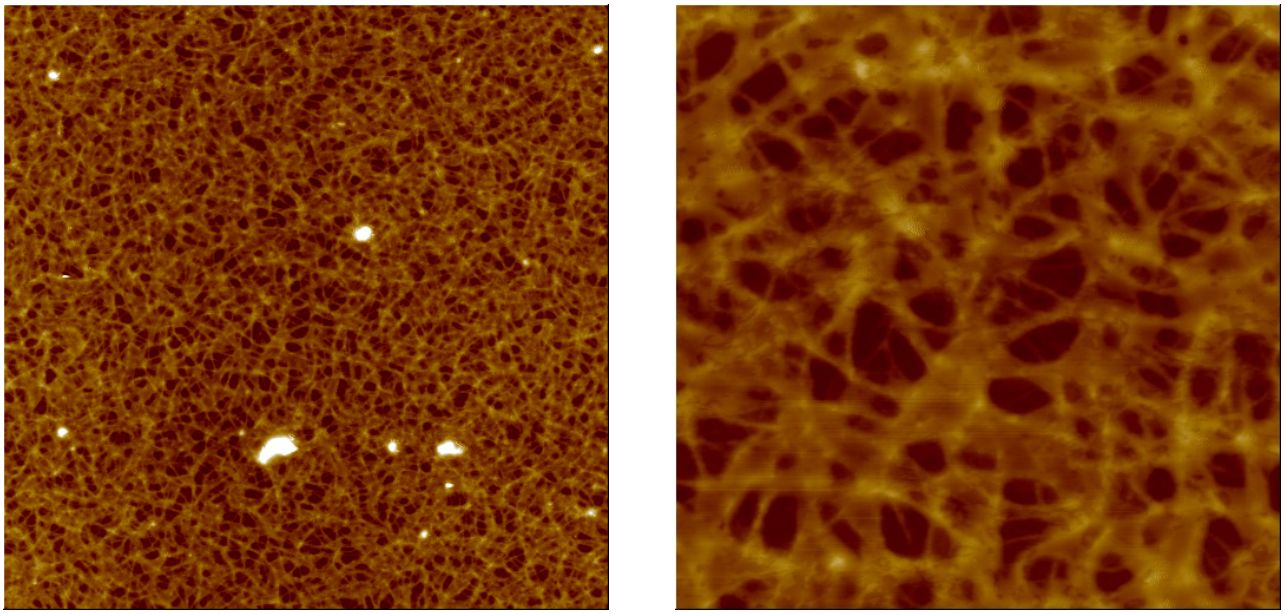

Figure 5.33 – AFM height images of drop-casted nanohybrids films.
(left) 20x20 um image, $\vec{z}$ scale = 100nm, (right) 5x5um image, $\vec{z}$ scale = 100nm.

As noted before, drop-casting technique can't usually guarantee a uniform coverage. In fact, scanning a different area of the same sample, in particular an outer area far from the center of the substrate, the images obtained showed a quite different morphology (figure 5.34).

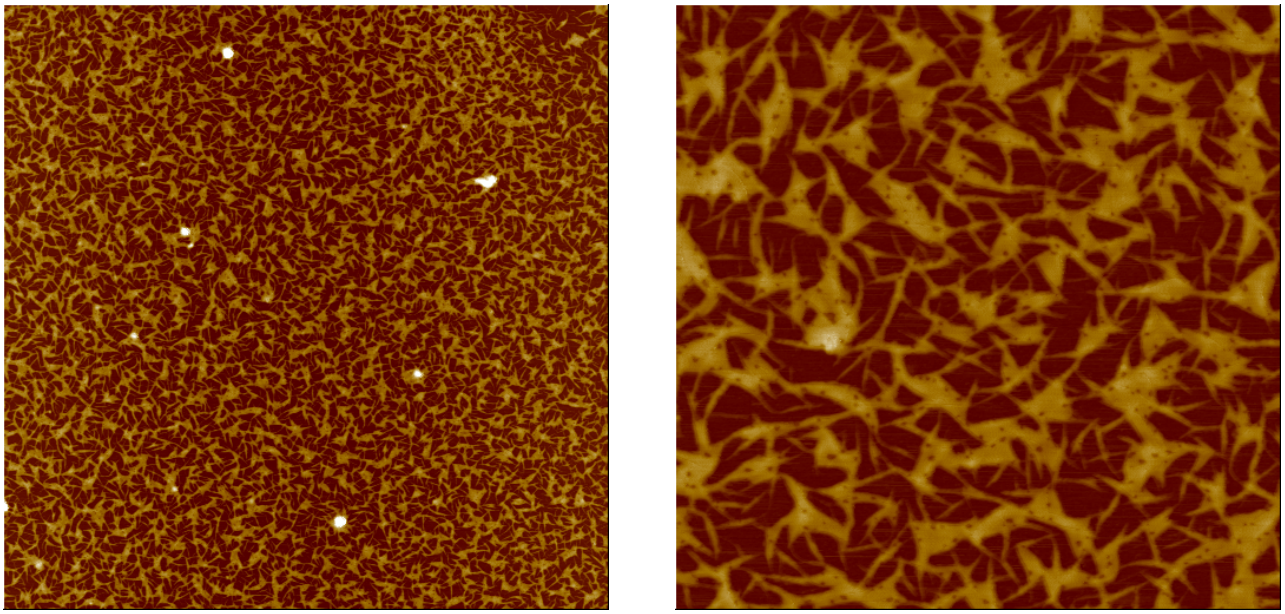

Figure 5.34 – AFM height images of drop-casted nanohybrids films.
(left) 20x20 um image, $\vec{z}$ scale = 50nm, (right) 5x5um image, $\vec{z}$ scale = 50nm

Comparing AFM images from inner (figure 5.33) and outer (figure 5.34) areas of the drop- casted film, it is possible to note the minor density of NHs and shorter characteristic heights of the features in the outer region with respect to the inner one. This could be explained considering that after spreading of the NHs dispersion on the substrate, solvent evaporation usually starts from the border and proceeds radially to the center, creating in the meanwhile a concentration gradient in the liquid phase above the substrate, which leads to a consequent gradient in the density of the film deposited.

Film deposited by spin-coating

After the drop-casted preliminary samples, spin-coating technique was used to deposit hybrid films with the aim of obtaining a uniform coverage of the substrate and in a reproducible way. The films were then analyzed by AFM.

First results are showed in figure 5.35. AFM analysis of spin-coated film highlighted the creation of a different morphology. Nanohybrids form an underlying network, which can be notice at small scan size (right image of figure 5.35), but the quality of the hybrid film is clearly affected by an excess of polymer residue, present in the film in the form of high (> 150 nm), round-shape, aggregates which are a consequence of an poor solvent extraction purification of the nanohybrids.

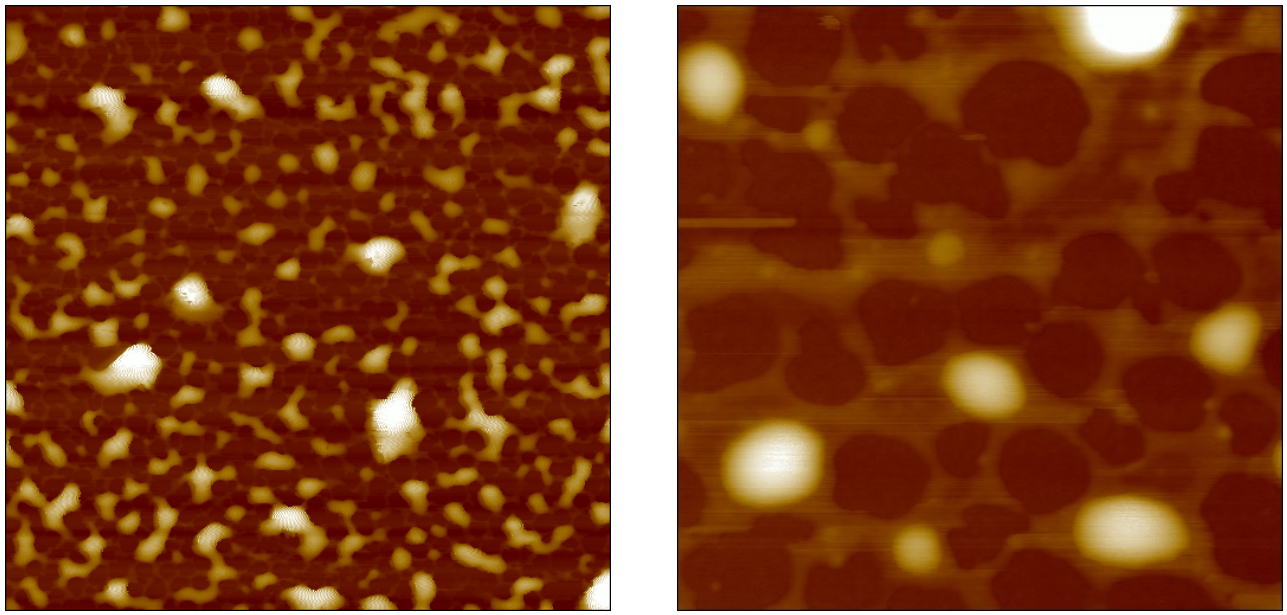

Figure 5.35 – AFM height images of spin-coated nanohybrids dispersion characterized by an excess of free polymer. (left) 10x10 µm image, $\vec{z}$ scale 150 nm, (right)) 2x2 µm image, $\vec{z}$ scale 50 nm

Despite the poor quality of the dispersion, this sample has the merit to highlight that interesting morphologies can be obtained, provided that the purification of the nanohybrids is improved.

Therefore new NHs were preparaed and solvent extraction process was accurately executed to reduce the amount of residual free polymer in the final dispersion. This allowed to obtain disperion characterized by a higher content of nanohybrids in conjunction with a lower amount of free polymer.

Spin-coating of this new dispersion produced films with a totally different morphology, showing a netwotk of connected nanohybrids with limited amounts of free polymer (figure 5.36).

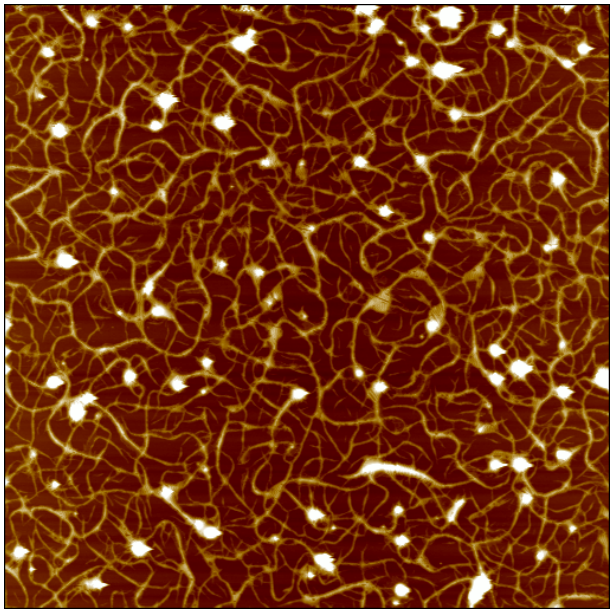

Figure 41.36 – AFM height image of spin-coated nanohybrids dispersion with reduced free polymer forming a well-defined network. 20x20 µm image, $\vec{z}$ scale 50 nm

Since one of the advantages of spin-coating is the possibility of modulating the morphology of thin films through variation of experimental parameters, the influence of the spinning rate on the films deposition was investigated. Films were therefore deposited using equal volumes of NHs dispersion (50 µl) but varying the spinning rate during deposition, ranging from 1000, 2000 and 3000 rpm.

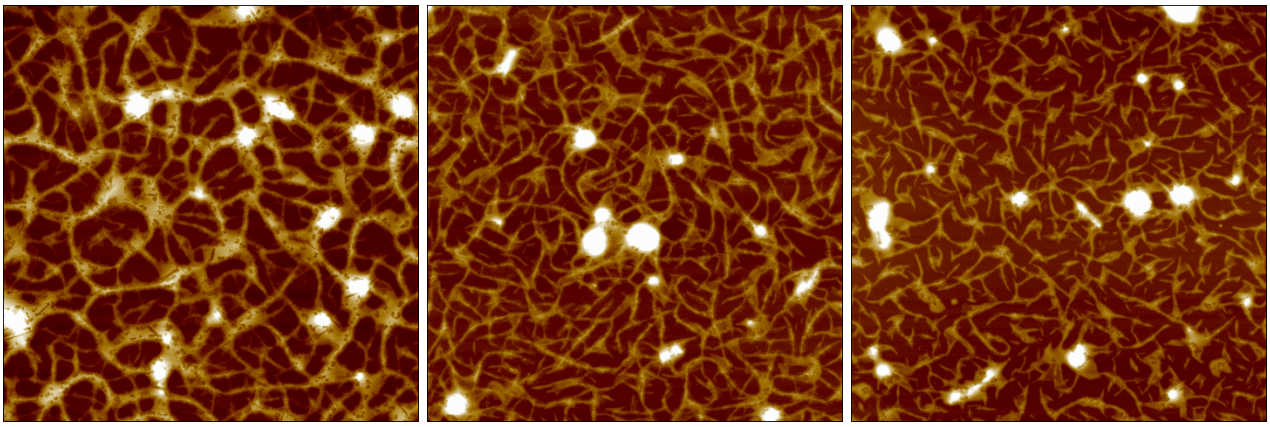

Figure 5.37 – AFM height images of nanohybrids films deposited at 1000 rpm (left), 2000 rpm (center) and 3000 rpm (right). All the images are 10x10 µm with $\vec{z}$ scale = 50nm

The AFM analysis of the resulting films allowed to highlight their singular morphology (figure 5.37). In addition, spin-coating was proved to be a technique giving more reproducible results, since very similar morphologies are obtained on different samples, and finally it is worth to note that changes in experimental parameters such as angular velocity allowed to exercise a control on the resulting morphology. It is in fact evident that, comparing samples deposited at 1000 rpm and 2000 rpm (left image and center image of figure 5.37, respectively), an increase of the spinning rate leads to a lower and thinner (with less polymer adsorbed) network. A further increase to 3000 rpm intensifies these effects causing the interruption of the network.

AFM allowed also to confirm that nanohybrids networks are obtained in a reproducible way on relatively large area of the substrate as 50x50 µm and on different samples (figure 5.38).

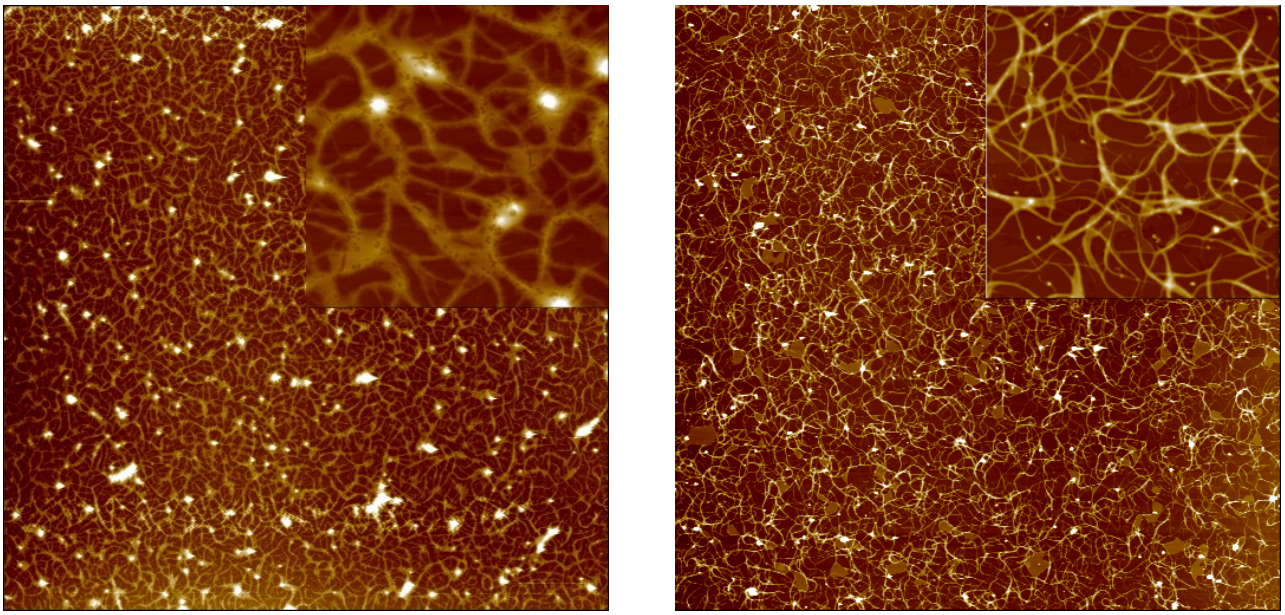

Figure 5.38 – AFM height images of nanohybrids films obtained from distinct dispersion showing different network "quality" (left) 50x50 µm image, inset is 5x5 µm, $\vec{z}$ scale 100 nm, (right) 50x50 µm image, inset is 5x5 um, $\vec{z}$ scale 50 nm.

AFM images in figure 5.38 are obtained starting from two distinct NHs dispersions, deposited in the same conditions by spin-coating. From the images it appears evident a difference in the quality of the networks, in terms of free polymer residue: in the left image of figure 5.38, nanohybrids are thicker and a certain number of polymer aggregates (white, circular spots) are present, while in the right image of figure 5.38, these two issues are considerably reduced, indicating a more effective removal of the P3HT in excess in the solvent extraction process. This highlights the importance of the physical steps (dispersion, centrifugation, precipitation) of the nanohybrids purification process, which has a direct effect on the quality of the final network obtained in the NHs film.

Figure 5.39 shows the same NHs network at progressive scan size of 10 µm, 5 µm, 1.5 µm.

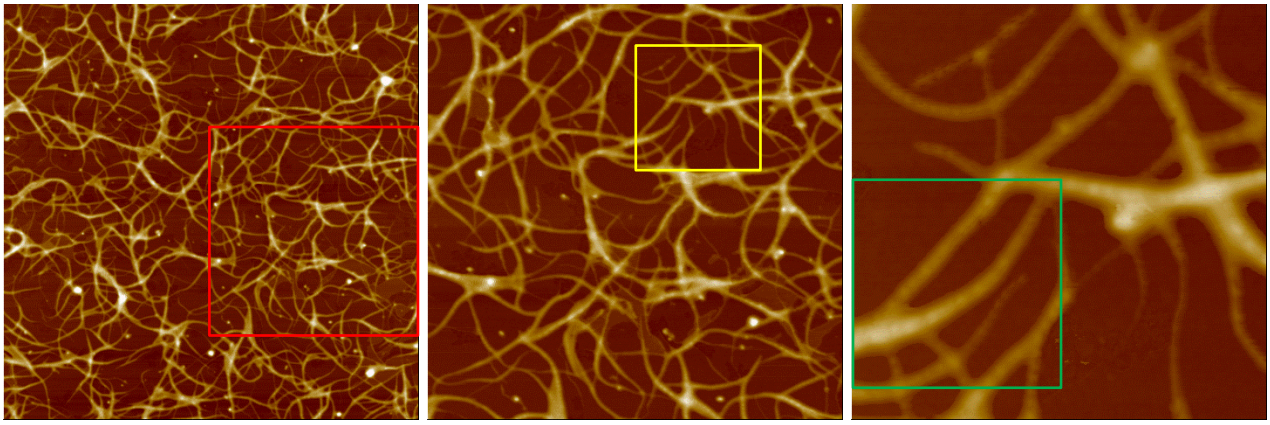

Figure 5.39 – AFM height images of nanohybrids film at different scan size: (left) 10x10 µm, (center) 5x5 µm, (right) 1.5x1.5 µm. $\vec{z}$ scale 50 nm for all images. Red box in left image corresponds to center image. Yellow box in center image corresponds to right image. Green box corresponds to area analyzed in fig.9.

Continuing to zoom in the sample analized in figure 5.39 is useful because allows to have a closer look on the nanohybrids. Interesting details can be inferred from the section analysis of the height (figure 5.40) and the phase (fig.10) profiles, characteristic of the nanohybrids.

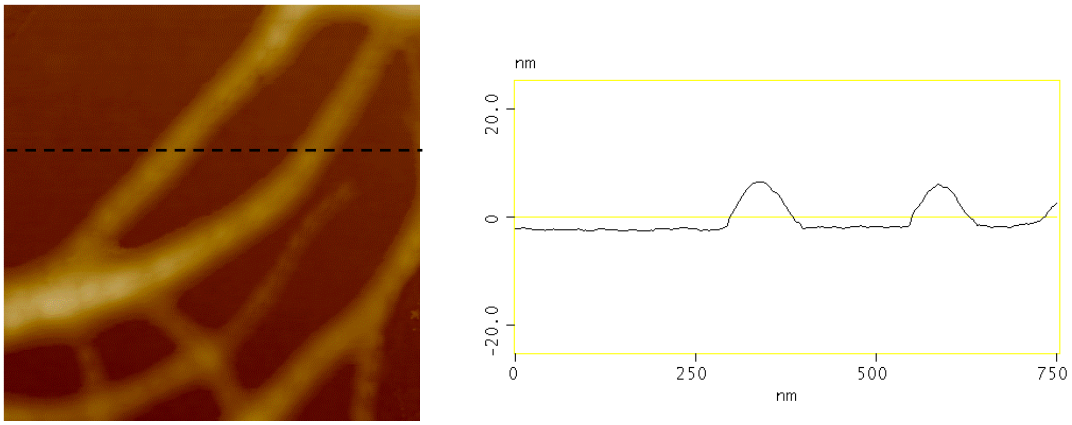

Figure 5.40 – (left) AFM height image of nanohybrids, 750x750 nm, $\vec{z}$ scale 50 nm. (right) height profile measured along the dashed line.

The height profile is useful to get an idea of typical heights of nanohybrids. From the section analysis, measured heights are comprise between 7.6 and 8.3 nm, but in figure 5.40 is possible to note also thinner NHs, proving that nanotubes are effectively exfoliated from the bundles and isolated through the wrapping of a very thin layer of P3HT.

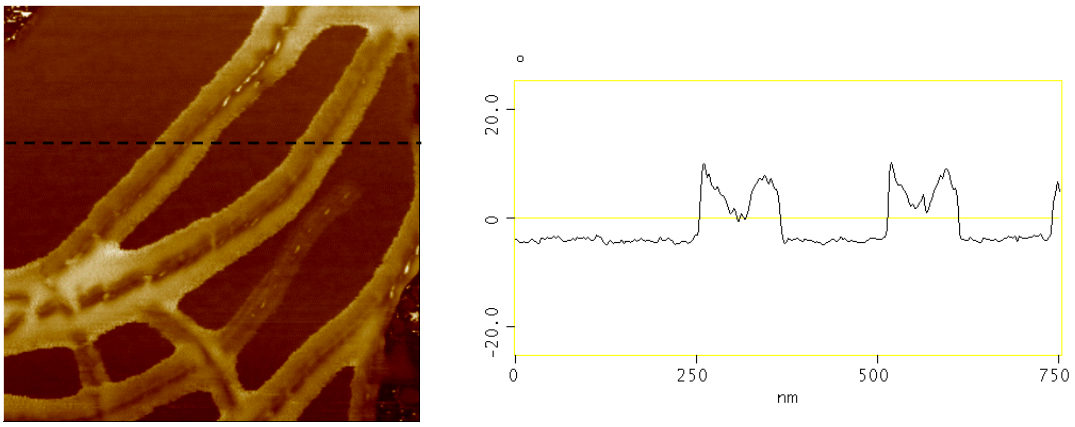

Figure 5.41 – (left) AFM phase image of nanohybrids, 750x750 nm, $\vec{z}$ scale 50°. (right) phase profile measured along the dashed line.

The phase profile allows to distinguish between the two different materials forming the nanohybrids, giving the proof of a phase-separation on nanometric scale. In fact nanotubes wrapped by the polymer are not directly observed in the height images (figure 5.40) because totally covered by the polymer, whereas they are easily observed in the phase image (figure 5.41). SWNTs visualization is possible because of the different response of nanotubes and polymer towards the AFM scanning tip. In fact, phase signal is sensitive to variations in composition, adhesion, friction, viscoelasticity as well as other factors, being a measure of the energy dissipation involved in the contact between the tip and the sample. For these reasons, phase contrast is commonly used for a qualitatively 'mechanical' characterization of sample surfaces, allowing to distinguish between softer (polymer) and stiffer (SWNTs) materials.

5.5.4 Bibliography

[1] A. Nish, J. Hwang, J. Doig and R. J. Nicholas – *Nanotechnology*, **2008**, *19*, 095603.

[2] D. H. Kim, H. Shin, H.S. Lee, J. Lee, B. Lee, W. H. Lee, J. Lee, K. Cho. W. Kim. S. Y. Lee, J. Choi and J. M. Kim – *ACS Nano*, **2012**, *6*, 662–670.

[3] M. C. Gwinner, F. Jakubka, F. Gannott, H. Sirringhaus, and J. Zaumseil – *ACS Nano*, **2012**, 6, 539–548

[4] L. S. Liyanage, H. Lee, N. Patil, S. Park, S. Mitra, Z. Bao, and H. P. Wong – *ACS Nano*, **2012**, 6, 451–458

[5] T. Schuettfort, A. Nish and R. J. Nicholas – *Nano Lett.*, **2009**, *9*, 3871-3876.

[6] S. D. Stranks, C. Yong, J. A. Alexander-Webber, C. Weisspfennig, M. B. Johnston, L. M. Herz, and R. J. Nicholas – *ACS Nano*, **2012**, *6*, 605-6066

[7] S. D. Stranks , S. N. Habisreutinger , B. Dirks , and R. J. Nicholas – *Adv.Mater.*, **2013**, *25*, 4365-4371.

[8] T. Schuettfort, H. J. Snaith, A. Nish and R. J. Nicholas – *Nanotechnology*, **2010**, *21*, 025201.

[9] J. L. Bahr, E. T. Mickelson, M. J. Bronikowski, R. E. Smalley and J. M. Tour – *Chem. Commun.*, **2001**, 193–194.

[10] H. T. Ham, Y. S. Choi and I. J. Chung – *J. Coll. Interf. Sci.*, **2005**, *286*, 216-223.

6. Summary and outlook

In this work, nanotubes were purified by means of a liquid phase oxidation, using a mixture of concentrated sulfuric and nitric acids. Nanotubes were oxidized varying sensitive reaction parameter such as time and temperature to find out the best conditions possible for purification, in terms both of final quality and final yield of the purified product. It was seen that reaction temperature has a deep effect on purification's results even for short reaction time. An oxidation temperature of 70°C was selected as best compromise for impurities removal with nanotubes preserving. The purification based on the oxidation at 70°C was followed by a second step where oxidized nanotubes were refluxed in strong alkaline media for long time. This step, usually called base-wash is useful in the removal of the carbonaceous impurities formed after oxidation of the amorphous carbon that tend to adsorb onto the sidewalls of the nanotubes. In the attempts to further improve the final quality of the purified product, the purification was repeated modifying the oxidation time, once oxidation temperature was set to 70°C. In this way a more efficient oxidation of the impurities was accomplished, and the base-wash step after the oxidation allowed to further eliminate the remaining impurities, producing high quality purified nanotubes.

Purified nanotubes were characterized through atomic force microscopy (AFM), thermogravimetric analysis (TGA), Raman spectroscopy and near infrared photoluminescence spectroscopy (NIR-PL). AFM was used to obtain a direct visualization of nanotubes purity after their deposition on substrates, allowing to evaluate the presence of amorphous carbon and the aggregation of nanotubes in bundles. This technique effectively allowed to verify the success of the purification process. TGA was used to evaluate the reduction of the residual metal content in the purified. The final purified material was demonstrated to have the minor metal content and a oxidation temperature higher than the raw sample, most of the with respect to all the other previous samples evidencing also that the oxidation-based purification is able to not lead substantial damage to the tubes, as evidenced by the high oxidation temperatures. Raman spectroscopy has allowed to analyze the effect of the oxidation and base-wash steps onto the nanotubes through the analysis of the modification of their characteristic bands. In particular, the ratio between the intensity of D (due to defects) and G (correlated to the integrity of the structure) bands, was used as index of the effective purification. Also variation of the characteristic band profile, linewidths and peak shifts gave important information on the improved quality of the final product. Finally, and most importantly, NIR-PL proofed that, after the oxidation-based purification, nanotubes are still able to emit, hence allowing to infer that their electronic properties are maintained unaltered so that it is possible for this purified nanotubes to realize their full potential by being integrated in electronic devices.

The second part of the thesis was focused on nanotubes/semiconducting polymer composites, in particular, using poly(3-hexylthiophene), (P3HT). Composite dispersions were first prepared in liquid

phase, using a noncovalent approach where nanotubes are stabilized in solution by the interaction with the conjugated polymer. These composite dispersion were prepared with 10/1 and 1/1 polymer/nanotube ratio and were used to deposit composite SWNTs/P3HT thin films. The electrical properties of such composite thin films were investigated upon fabrication of Schottky diodes depositing the composite thin film between the electrodes. Current-Voltage measures showed the effect of the nanotubes on the transport behavior of the semiconducting polymer, revealing that nanotubes enhance the conductivity of the devices up to two orders of magnitude. In addition, the characteristic current profile of the diode is modified by nanotubes so that the system is no more rectifying but shows comparable conductivities for both charge carriers, holes and electrons. This open the possibility to use this systems in optoelectronics, namely as organic light emitting diode, where the efficiency is correlated to the radiative recombination of opposite charge carriers and it is strongly positively influenced whenever the mobility of the two type of charge carriers have the same order of magnitude.

Optical properties of composite dispersion were also investigated, both in UV-Vis absorption and emission. Absorption spectroscopy revealed that P3HT and SWNTs interact so strongly to modify the absorbance spectrum of the polymer. A new band arises, partially overlapped to the principal absorption band of the polymer. This band is relative to those polymer chains adsorbed onto nanotubes surface. This physisorption changes characteristic energy level of the polymer because adsorbed chains experiment an higher conjugation length an crystalline order induced by the strong π–π interactions with the underlying nanotube. This was further proved showing that the absorption spectrum of the composite dispersion matches fairly well with one obtained from a pure P3HT thin film. Finally, emission spectra further proofed the interaction at molecular level between P3HT and SWNTs, as evidenced by quenching of the polymer fluorescence upon addition of nanotubes, due to charge transfer from the excited P3HT to the SWNTs. The possibility to have a photoinduced charge transfer open the way for the application of this composite system in photovoltaics because charge transfer from a donor to an acceptor is at the base of organic photovoltaic since it allows to split the exciton formed upon absorption of the light in two separated charge carriers which can therefore transport current across the device. This led to consider that the electronic interactions between P3HT and SWNTs are responsible of the formation of a supramolecular multifunctional composite complex, which is a nanoscale hybrid system, i.e. a nanohybrid.

Finally, a method for the nanostructuring of SWNTs/P3HT composite thin films was developed. This method relies on the strong interaction between nanotubes and conjugated polymer to isolate nanohybrids after their formation in solution. In fact, the starting composite dispersions were enriched in nanohybrids by means of a series of physical steps with the purpose of remove the polymer in excess from the dispersion leaving only that adsorbed on the nanotubes. In this way, it was possible to obtain a nanohybrid-enriched dispersion. The deposition of this dispersion allowed to obtain thin nanohybrids films. AFM of these films showed a singular morphology. Nanohybrids are characterized by an inner nanotube core and an outer polymer covering. The overall height of these structure is comprised in less than 10 nm, realizing a hybrid film with nanoscale phase separation, therefore suitable for nanoelectronics.